Modelling of large-scale brain network dynamics

Michael Forrester

Thesis submitted to the University of Nottingham
for the degree of Doctor of Philosophy

I hereby declare that this thesis is all my own work, except as indicated in the text.

July 2020

"I may not have gone where I intended to go, but I think I have ended up where I needed to be."

- Douglas Adams

Abstract

Like many systems in nature, the brain is a highly organised unit of interacting components. A natural way to study such systems is through the lens of mathematics, from which we may attempt to delineate the mechanisms that underlie seemingly unfathomable brain functionality using prescribed parameters and equations. In this thesis, we use large-scale *neural mass* network models of the human cortex to simulate brain activity. Moreover, we utilise techniques from graph, linear and weakly-coupled oscillator theory to describe the network states that are exhibited by such models. In particular, we focus on how the emergent patterns of synchrony (which are thought to be fundamental to the function of brain), or so-called *functional connectivity*, are dependent on the *structural connectivity*, which is the anatomical substrate for brain dynamics. Through large-scale network simulations and linear analysis we find that the structure–function relationship is highly dependent on– and indeed, predictable from– the dynamical state of individual nodes in the network, highlighting the role of dynamics in facilitating emergent functional connectivity. We take this further to consider how network states are modulated by external simulation and conduction delays, especially in relation to the influence of *transcranial magnetic stimulation* (TMS) on the brain's dynamics and, more generally, its role as a *neuromodulator*. We describe a computational framework using a recently developed *next-generation* neural mass model, by which trains of simulated pulses are employed to drive network dynamics into different states, which we believe may be adapted to be used to study the efficacy of TMS and to test *in silico* different stimulation protocols that can be used to treat neurological conditions. We then analyse more specific applications to potential effects of TMS: neural entrainment and conduction delays (which may be altered via TMS-induced plasticity). We use the theory of Lyapunov exponents to study entrainment via external stimulation and use linear analysis, as well as structural *eigenmodes*, to predict emergent network states due to conduction delays across long-range white matter projections.

Acknowledgements

Firstly, I would like to thank my supervisors Dr. Reuben O' Dea, Prof. Stephen Coombes and Dr. Jonathan Crofts for their invaluable support and guidance over the last 4 years (a special mention to Reuben for joining me on several misadventures around Lisbon). You have always been generous with your time and were always happy to lend a helping hand. Also thank you to Dr. Stam Sotiropoulos for his helpful contributions, especially with providing connectivity data.

To Dr. Marc Goodfellow, Prof. John King and Prof. Gary Mirams, thank you for a very nice remote viva and also for having excellent internet connections so it all ran smoothly!

I owe a huge debt of gratitude to the Beacon for Precision Imaging. Thanks to Dorothee Auer, Sarina Iwabuchi, Peter Liddle and Stephen Jackson for many helpful discussions and giving me the opportunity to present my work on a number of occasions. I'm also very grateful for the opportunity to work with the Beacon during a sixth-month research placement, and I look forward to working with them again over the next two years.

Thanks to my family for their encouragement and my friends for their welcome distractions. Also to everyone I've had the pleasure of living with over the years and shared in drinking of an incalculable number of cups of tea. Even in the midst of a global pandemic, there have been so many incredible getting me through the surreality of lockdown life and I'll be forever grateful for their support.

Publications

- Forrester, M., Crofts, J.J., Sotiropoulos, S.N., Coombes, S. and O'Dea, R.D., 2020. The role of node dynamics in shaping emergent functional connectivity patterns in the brain. Network Neuroscience, 4(2), pp.467-483. [adapted in chapter 4]

- Byrne, Á., O'Dea, R.D., Forrester, M., Ross, J. and Coombes, S., 2020. Next-generation neural mass and field modeling. Journal of Neurophysiology, 123(2), pp.726-742. [adapted in chapter 6]

Contents

Chapter 1

Introduction

Deciphering the mechanisms which underpin the phenomenon of cognition is one of the greatest challenges in science. Ironically, the main tool to study this has, for much of history, been the brain, which itself has not been sufficient enough to fully understand its own complexities. However, the last century has seen remarkable advances in the way the brain can be studied. With the advent of computing and precision neuroimaging techniques, researchers are now able to collect and analyse vast amounts of data from the brain, accelerating our understanding of how complex cognitive functions arise. This has, in turn, inspired novel mathematical modelling techniques which aim to replicate some of the phenomena observed in empirical studies and, moreover, attempt to shed light on the mechanisms that underpin them.

In this thesis, we will analyse how existing models of neural activity can be used as a tool to understand and predict brain dynamics. In particular, we make use of the availability of structural connectome data to build computational models of large-scale brain activity and explore ways to study how emergent brain function arises from its underlying structure. Elucidating these so-called *structure–function relations* is primarily achieved through calculating properties of coherent behaviour between simulated activity of different brain regions, known as '*functional connectivity*' (FC). We then specialise our study to look at transcranial magnetic stimulation, an increasingly popular clinical tool for treating neurological disorders, in order to investigate how its efficacy arises. Specifically, we investigate localised stimulation strategies and their effect on FC, *entrainment* of brain activity to a rhythm and modulation of delays in neural signal transmission to induce oscillations.

In chapter 2 we introduce the biological processes underpinning the large-scale activity of the brain that we accommodate within our models and further explain how these are captured using neuroimaging methods. We then specify the open biological questions that have motivated this research and why they are ripe for treatment with mathematical methods. We review some of the mathematical advances that have been made in the field of modelling neural systems, as well as contributions from some other fields of applied mathematics which prove useful in the analysis of such large-scale brain models.

Chapter 3 outlines the mathematical frameworks which are used to derive results in the subsequent chapters, chiefly network properties, linear analysis of dynamical networks and the theory of weakly-coupled oscillators.

Chapter 4 is the first of our technical chapters, in which we analyse how the dynamic state of brain networks modulates the relationship between the underlying physical, or '*structural*', connectivity (SC) and functional connectivity of brain regions. We use mathematical theory to describe how these arise from the linear instability of states, most notably the instability of the synchronous network state.

In chapter 5 we continue looking at structure–function relations through the introduction of a new network metric that describes the transitivity of nodes. The novelty of our new metric, more generally referred to as a measure of '*clustering*', is that we consider the functional and structural networks to exist as two separate layers superimposed on one another in what is known as a *multiplex*, allowing for the treatment of two or more interacting network structures simultaneously.

Our focus moves in chapter 6 from looking at structure–function relations in generality to describing how these may be manipulated by external forcing, with a particular focus on *transcranial magnetic stimulation* (TMS). We use a newly developed neural mass model with a diverse dynamic repertoire to explore how the network can be forced into different dynamic states and how these may relate to the treatment of conditions such as depression.

In chapter 7 we take a more analytical approach to explore the effects of TMS. We use linear theory at the network level to determine how conduction delays between brain regions, which may be influenced by neuronal plasticity resulting from TMS treatment, can modulate functional connectivity states. We also explore the how periodic forcing at different frequencies can drive entrainment.

We conclude with an overview of our main findings as well as the scope for work to be done in furthering this research.

Chapter 2

Background

2.1 Biological background

The study of the brain is a complex subject due to the myriad chemical and electrical signals that propagate within it and the diversity of spatial scales over which neural activity occurs, from long range cortical relays at the whole-brain scale to synaptic neurotransmitters at the sub-cellular scale. A neurophysical background is essential to understand both the anatomy of large scale brain networks and their emergent function that motivate the questions we discuss in the following chapters. Moreover, the models we use relate to real biological processes that are captured by coarse-grained neuroimaging techniques. Here we provide a brief overview of the basis of electrochemical activity and its propagation in the brain in order to describe how emergent function is empirically measured.

2.1.1 Physiology of the brain

Brain cells

The cells present in the brain can be broadly categorised into two groups: glia and neurons, both of which are estimated to number in the order of 10^{11} in humans (von Bartheld *et al.*, 2016).

The function of glial cells is to offer a supporting structure to the neurons, as well as aid with nutrient delivery, cell repair and myelination — the latter refers to a process whereby the electrically active fibres of neurons are coated in a fatty sheath for purposes of electrical insulation. While glial cells facilitate brain function in a variety of ways, they are not directly involved in the electrochemical processes by which neurons provide a substrate for cognition and other complex brain functions.

The neurons are the basic functional units of the central nervous system. It is their collective behaviour that underpins the emergence of macroscopic brain rhythms and is the primary focus of the work presented in this thesis. The structure of a neuron can be generally described by 3 sub-units:

- *The soma* is the main cell body of the neuron containing the nucleus.
- *The dendrites* are projections of the soma which recieve input from other nerve cells.
- *The axon* is a fibre along which electrical current flows from the soma to other cells. It splits at the end into thousands of smaller fibres called telodendria which have synaptic terminals at their tip. These terminals form electrochemical connections with the dendrites of other cells, which are known as *synapses*.

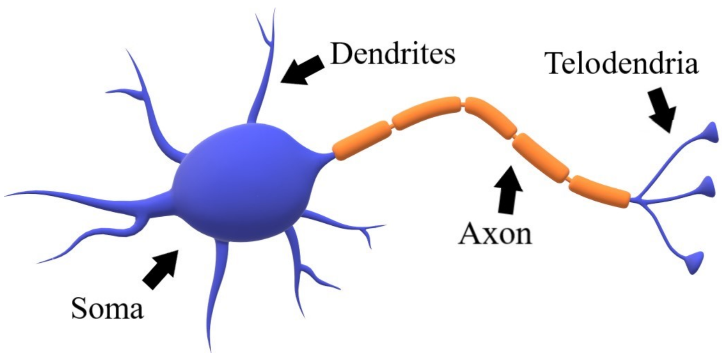

Figure 2.1: Structure of a neuron: A caricature of a typical neuron showing the soma with dendritic appendages and axon fibre (taken from Microsoft 3D Library).

Neuron populations and functional regions

As well as the numerous electrochemical processes undergone by individual neurons, the brain's ability to exhibit a variety of complex behaviours simultaneously is undoubtedly facilitated by the sophistication of its architecture. From neuronal microstructures to the macroscopic regions that encode the properties of body and mind, it is vitally important that communication in the brain happens on multiple spatio-temporal scales (Betzel and Bassett, 2017).

In order for electrical signals to propagate between neurons, chemical signals pass between the synaptic clefts that lie between axon terminals and the dendrites of neighbouring cells. There are roughly 10^{14} of these connections in the human brain, which highly specialised signaling molecules called neurotransmitters drift across. It is important to note that there are over 200 different neurotransmitters involved in chemical communication across synapses, the specifics of which are beyond the scope of this thesis.

The fundamental mechanism behind electro-chemical communication in the brain is the action potential, whereby the potential difference between the cell membrane and main body is depolarized from rest (about -70mV) through afferent inputs and other electro-chemical processes until it reaches the threshold for action potential generation (around -55mV). At this point, this *presynaptic* cell rapidly depolarises and a current passes down the axon towards its terminals in the form of a travelling pulse. At axon terminals, the action potential causes neurotransmitters to be released, which provoke specialised proteins in a neighbouring *postsynaptic* neuron, called *ion channels*, to allow the passage of charged particles across the cell membrane. The most common neurotrasmitters are GABA, which opens ion channels to decrease post-synaptic membrane potential (*hyperpolarisation*) and glutamate, which conversely opens ion channels to increase membrane potential (*depolarisation*), which in turn may either inhibit or excite an action potential in the postsynaptic neuron's soma respectively. In this way, electrical signals propagate locally within neural populations and form the basis of their spatio-temporal activity that underpins FC.

Large-scale brain structure and activity

Although neural signalling can occur at at the micro-scale, it also takes place over much greater distances in the brain. Indeed, white matter (highly myelinated neurons) has a total length of the order of 10^8m in the human brain and is capable of sending action potentials much further than the surface grey matter (Wen and Chklovskii, 2005). The thick layer of myelin around an axon acts as an insulator, allowing charge to jump via ionic exchange within gaps called nodes of Ranvier, shown as small crevices in the axon's coating in Figure 2.1. Because of this efficient transfer of charge, conduction velocities along myelinated axons are around 150ms^{-1} as opposed to around 0.5–10ms^{-1} for unmyelinated axons, commonly found in grey matter. Much of the surface of the brain is grey matter, forming folds (*gyri*) and troughs (*sulci*) on the surface, while much of the deeper volume is made up of white matter tracts.

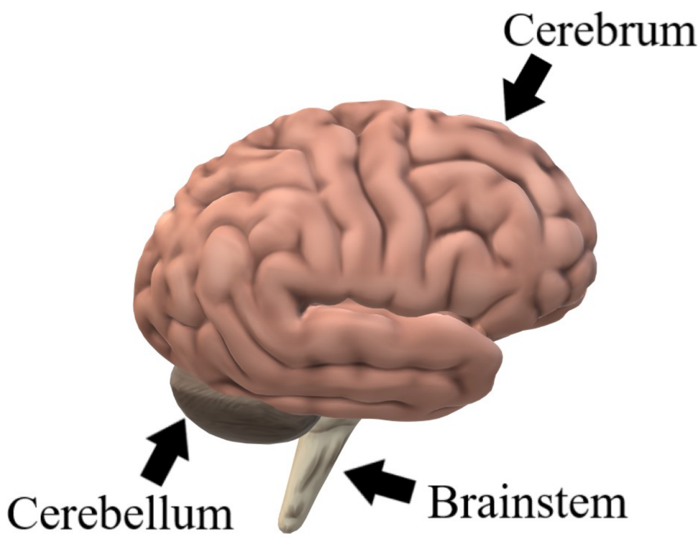

Figure 2.2: Basic brain anatomy. Coarse division of the brain into its three main components (taken from Microsoft 3D Library).

On the largest scale, the brain can be coarsely divided into three regions, as shown in Figure 2.2:

- *The cerebrum* is the largest part of the brain which processes voluntary actions and thought.

- *The cerebellum* is located at the back of the brain and is largely responsible for regulating motor function.

- *The brainstem* contains several sub-components required for maintaining homeostasis and well as relaying sensory information between the brain and the rest of the body.

The brain can further be divided into more refined subdivisions known as parcellation atlases, wherein borders between neighbouring regions reflect distinct functional or physiological differences between them. The density of white matter connections between these parcellations is commonly refered to as *structural connectivity* (SC). It is important to note here that there is no perfect map of the brain for the simple reason that all brains are different. Though many different parcellations exist, their usage is generally dependent on the context of the study in which they are applied. An example is given in Figure 2.3, which we also use in further chapters as a basis for many of our large-scale brain dynamics simulations.

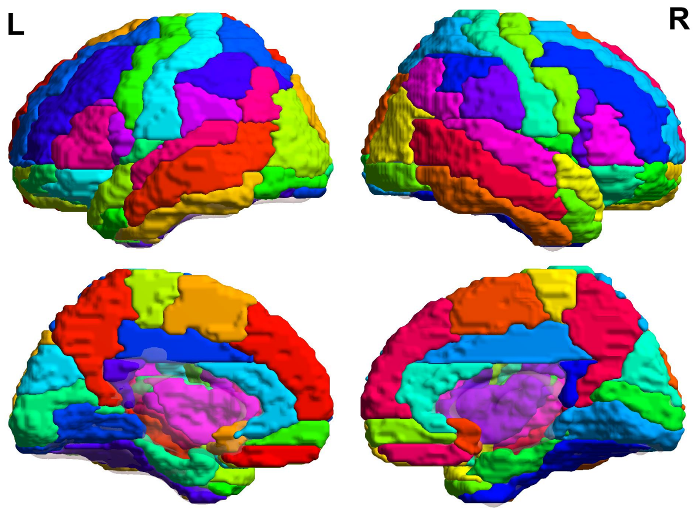

Figure 2.3: AAL atlas. Division of the brain into 78 regions of the Automated Anatomical Labeling atlas described in Tzourio-Mazoyer *et al.* (2002).

Much of the activity observed in neuroimaging studies comes from activity near the surface of the cerebrum, the cerebral cortex, simply because it is nearer the scalp and therefore more accessible for non-invasive imaging. The cortex is divided into vertical structures, which are around 500μm in diameter and generally run perpendicular to the surface, called 'columns' (Mountcastle, 1957), which have horizontal projections to other columns (Hawkins *et al.*, 2017). Cortical regions that are described by parcellation atlases are typically composed of thousands of these columns (Krueger *et al.*, 2008).

Oscillation in cortical regions arises from intrinsic excitation within neural populations, as well as feedback loops between other cortical regions. They are also governed by extra-cortical input, most notably from the thalamus (Guillery and Sherman, 2002; Sherman, 2005), which delivers sensory input to cortical regions but also forms a feedback loop which can synchronise firing activity of the thalamus as well as several cortical regions. The nature of these oscillations is highly dependent of the functional state of the brain (Hwang *et al.*, 2017). Indeed, certain parts of the brain that behave coherently can act as a biomarker for a certain cognitive task (Uhlhaas and Singer, 2006). The patterns arise from the correlated amplitude, phase or frequency of neural activity, which are often noisy and highly transient (Bowyer, 2016). Together, these correlations describe which parts of the brain are co-currently active, illustrating a different kind of network that is explicitly linked to dynamic brain function, hence why it is known as *functional connectivity* (FC).

Neural sub-networks

While the functional connectivity of the brain is in constant fluctuation (Cabral *et al.*, 2017; Hutchison *et al.*, 2013b; Deco *et al.*, 2017b), there are several classes of well-categorised states that have been extensively studied. *Resting state networks* (RSNs), which are functional networks recorded when the brain is not task-focussed, have been one of the most well-categorised of these, due to the ease of recording the brain without stimulation and the ability to reproduce similar experimental conditions with a range of different subjects. They are formed of a subset of brain regions that are found to be concurrently active or inactive, so can be represented as sub-networks within the wider whole-brain functional connectivity (FC) network. Yeo *et al.* (2011)

identified two sets of these sub-networks (dividing the brain into a 17 network as well as a coarser 7 network grouping within of the cortex). For more general purposes, one can consider three so-called 'core' networks (Menon, 2011) that form part of the 7 network structure:

- The *default mode network* (DMN) is a highly correlated network that is active during rest, while inactivity is often associated with task engagement. It is also related to introspective thought and empathy.
- The *salience network* (SN) is involved with a diverse range of functions including homeostasis and emotional processing. It is posited that this network amalgamates sensory and emotional processes while acting as a 'switch' between the default mode network and attention-based networks.
- The *central executive network* (CEN) is involved in high-level mental processing tasks such as focused problem solving and working memory, where important recent experiences are recalled in order to coordinate and complete a task.

These three networks are encapsulated in the parcellation in Figure 2.4 (Yeo *et al.*, 2011), as red, green and orange coloured regions respectively.

In a healthy human brain, these networks can be harmoniously activated/deactivated at will, though disruption of these core networks is associated with many neurological conditions (Putcha *et al.*, 2016; Yu *et al.*, 2017a; Chen *et al.*, 2019).

2.1.2 Relating structure and function

The underlying SC of the brain manifests itself as a complex circuit of interacting brain regions which supports the dynamic FC. Though it is true that strong structural connections correlate well with with strong functional connections across long time-scales (Hagmann *et al.*, 2008; Honey *et al.*, 2009), there is variability over short timescales, reflecting the rich dynamic repertoire of the brain (Honey *et al.*, 2007; Rubinov *et al.*, 2009). These dynamic FC

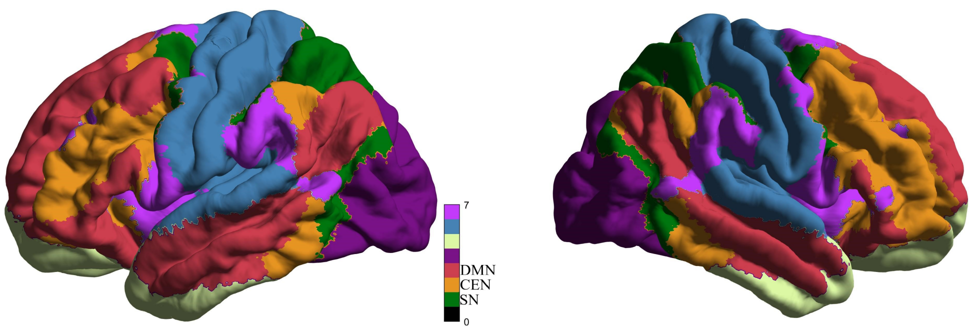

(a) Left hemisphere **(b)** Right hemisphere

Figure 2.4: Seven sub-network parcellation of human cortex. Here, regions of the cortical surface are coloured depending on the functional sub-network of which they are associated. This is a reproduction from Yeo *et al.* (2011) using data made available through FreeSurfer. Going from top to bottom of the colourbar, we have the following subnetworks: ventral attention in violet, somatomotor in blue, limbic in cream, visual in purple, default mode (DMN) in red, frontoparietal (central executive; CEN) in orange and dorsal attention (salience; SN) in green. The three core networks are labelled on the figure.

patterns are widely believed to be significant in integrative processes underlying higher brain function (Van Den Heuvel and Pol, 2010; van Straaten and Stam, 2013) and disruptions in SC and FC networks are associated with many psychiatric and neurological diseases (Menon, 2011; Braun *et al.*, 2015).

However, the relationship between the brain's anatomical structure and the neural activity that it supports remains largely unknown (Fukushima *et al.*, 2018; Batista-García-Ramó and Fernández-Verdecia, 2018). The divergence between dynamic FC and the relatively static structural connections between populations is critical to the brain's dynamical repertoire and may hold the key to understanding brain activity in health and disease (Park and Friston, 2013).

Presently, one of the most controversial aspects in this field of research is the role of criticality in explaining FC network transitions (Zimmern, 2020), whereby the brain's dynamics operate near to a 'tipping point' between different global states. There is much debate, however, concerning the mechanistic description of how this criticality manifests itself within the brain. Following from the influential work of Beggs and Plenz (2003), it has been suggested that neural activity organises itself in the form of 'avalanches', where the activation of neurons propagates through neural networks via a power law (Shriki *et al.*, 2013). However, this interpretation has been challenged due to evidence from *in vivo* spiking activity which is not in agreement with this principle. Further studies have suggested that the critical brain's critical regime is poised at a dynamic state at the edge stability and chaos (Boedecker *et al.*, 2012; Ezaki *et al.*, 2020) or synchronisation (Di Santo *et al.*, 2018; Palmigiano *et al.*, 2017). We treat this issue in chapters 4 by focusing on how the critical states of a model's dynamics organise the agreement between structural and functional networks. Notably, we find that these organisational features can be related to intrinsic nodal dynamics, without needing to understand the more complex network interactions that the model supports. Furthermore, in chapter 5 we consider how network dynamics organise a novel network measure that characterises the SC–FC relationship (see section 2.2.3).

2.1.3 Neuroimaging

There is a plethora of ways to visualise the brain on multiple spatial scales, from measuring the ionic flow in individual cells using a patch clamp, to measuring whole brain activity using electrodes and magnetometers. The former is also more invasive, since it requires direct contact with a neuron, while the others can be measured using devices placed outside the brain. Here we outline a sample of these techniques from the latter end of this scale, which are of most relevance to this thesis and we point the reader to Lowe *et al.* (2016) for a recent comprehensive review of these methods.

Electroencephalography (EEG) and magnetoencephology (MEG)

Due to its relatively low cost and high temporal resolution, EEG has been a popular tool for research and medicine for decades. It measures the voltage difference across electrodes placed on the scalp, caused by extracellular ionic flow from many thousands of neurons. Excitatory synaptic connections act as sources to increase positive ion flow across dendrites, while inhibitory synapses act as sinks. If neurons fire in a coherent way, electrical dipoles form in macroscopic areas comprising thousands of columns (Nunez and Srinivasan, 2006), which is the source of the EEG potential.

Conversely, MEG detects the magnetic fields generated by post-synaptic currents. This signal faces less interference from cranial tissue so is a better tool for source localisation (da Silva, 2013), though it is also much weaker than the EEG signal so requires superconducting magnetometers cooled using liquid helium in order to be sensitive enough to obtain reliable measurements.

Magnetic resonance imaging (MRI)

MRI is an imaging technique developed by Sir Peter Mansfield and Paul Lauterbur, for which they won the Nobel Prize in Physiology or Medicine in 2003. MRI exploits quantum properties of hydrogen atoms, present in water and fat cells, in order to image the brain (Berger, 2002). Fundamentally, MRI exploits the property of nuclear spin, which gives atoms a magnetic moment. The moments are typically randomly oriented in the brain so produce a very weak magnetic field due to destructive interference. MRI machines induce a strong magnetic field B to align the moments. Radio waves incident on the atoms causes their moments to spin about an axis in the direction of B, which induces a current on a receiver. If all atoms induced the same current, source localisation would not be possible. However, due to the quantised nature of energy, radio waves of a particular frequency only resonate atoms with a particular magnetic moment. A secondary magnetic field is applied with a gradient that isolates atoms so that their position can be calculated. The gradient field then constantly changes to scan across the entire spatial domain of interest.

Functional MRI

Functional MRI (fMRI) is a mechanistically similar procedure to standard MRI except it specifically measures the contrast between the responses of de-oxygenated and oxygenated haemoglobin, referred to as the blood-oxygen-level-dependent (BOLD) signal (Glover, 2011). The premise is that areas of the brain undergoing high activity require more energy, so blood flow is higher within these regions as highlighted in an fMRI scan that determines which areas of the brain are concurrently active and therefore functionally connected. This is beneficial compared to other signals arising from neuronal activity (EEG/MEG) because it has much higher spatial resolution. However, since fMRI does not directly capture the ionic flow arising from spontaneous neuronal activity it has poorer temporal resolution, since it takes time for blood to be transported to areas where it is required. The BOLD signal is also fundamentally different because oxygen transport may be due to processes other than neuronal firing (Hall *et al.*, 2014).

Diffusion MRI

Diffusion MRI is a more specialised version of MRI used to map the white matter structure of the brain (see Pujol (2015) for a detailed description of the techniques involved). Water diffuses isotropically in grey matter, but the myelin sheath of white matter tracts restricts the free movement of water, causing ansiotropic diffusion that is dependent on the orientation of the fibre. To track this diffusion, two additional magnetic field gradients are added to the standard MRI protocol in what is known as diffusion weighted imaging (DWI). The first non-uniform magnetic field is applied to a brain region in order to cause incident atoms to align differently to each other. A corrective field is then applied which has the effect of reverting them back to their original state; if atoms have moved in the intervening period the receiver will detect a reduction in current. This reduction is localised to the atoms whose moments are not fully aligned, indicating that diffusion has taken place in the direction of the applied gradient.

To build a map of the brain's white matter connectivity, diffusion MRI data is treated with post-processing techniques called tractography, which works on the assumption that water diffuses in the direction of white matter tracts. A seed point is chosen from which tract paths are estimated from directions of diffusion to construct a streamline traversing between points in the white matter domain called voxels, until it reaches some chosen termination point such as the grey matter/ white matter boundary. Single paths can be estimated algorithmically, or many different paths can be calculated probabilistically from different possible fibre orientations at each voxel (Hernández *et al.*, 2013).

2.1.4 Brain stimulation

With the advent of precision neuroimaging has come an increased use of sophisticated ways to stimulate neural activity, both for clinical and research purposes, since imaging offers a way to understand the neural mechanisms of action (Bergmann *et al.*, 2016; Horn, 2019). The purpose of brain stimulation is to disrupt the natural activity of the brain to inhibit or excite some effect, a process called *neuromodulation*.

Electrical stimulation

The first generation of brain stimulation came from electroconvulsive therapy (ECT), which was invented in the early 20th century to treat schizophrenic patients (Cerletti, 1950) but has since effectively treated Parkinson's disease (Popeo and Kellner, 2009; Fochtmann, 1988), depression (Pagnin *et al.*, 2008; Kellner *et al.*, 2012) and obsessive compulsive disorder (Mellman and Gorman, 1984; Maletzky *et al.*, 1994). ECT involves passing electrical current through the brain via electrodes placed on the scalp. A more invasive version of this is deep brain stimulation (DBS) (Perlmutter and Mink, 2006), which involves planting electrodes into subcortical areas of the brain to deliver electrical input to specific targets. DBS is typically used to treat severe motor-related disorders such as Parkinson's (Deuschl *et al.*, 2006; Vingerhoets *et al.*, 2002; Benabid, 2003), Tourette's (Shahed *et al.*, 2007) and dystonia (Ostrem and Starr, 2008), though due to its invasive nature, DBS is typically a last resort after other medical practises have proved unsuccessful. While the exact mechanisms which underlie the efficacy of these procedures remains unknown, it is clear that DBS and ECT do not elicit just a localised effect but also facilitate changes in large-scale brain network behaviour (Ashkan *et al.*, 2017).

Both of these stimulation methods have disadvantages for the patient: ECT can induce headaches and memory impairment (Gomez, 1975), while DBS is highly invasive, requiring surgery that which carries risk of complications such as infection and seizure onset (Fenoy and Simpson, 2014). An analogue to the aforementioned stimulation techniques using magnetic rather than electrical stimuli addresses some of the drawbacks presented by brain stimulation, which we discuss in the next section.

Magnetic stimulation

Transcranial magnetic stimulation (TMS) has gained popularity due to the fact that it incurs much less discomfort for patients, yet has also proved to be an effective treatment for many neurological disorders (Hallett, 2000). TMS is a non-invasive therapeutic brain stimulation technique whereby strong electromagnetic fields are used to induce a transient current pulse in the brain, in order to influence neural activity, particularly in superficial regions of cerebral cortex. TMS has potentially wide-reaching consequences for mental health conditions, having provided positive outcomes for patients with Parkinson's disease (Boggio *et al.*, 2005; Shimamoto *et al.*, 1999), schizophrenia (Lee *et al.*, 2005; Lett *et al.*, 2014) and depression (Kolbinger *et al.*, 1995; Loo and Mitchell, 2005; George *et al.*, 2000; Fox *et al.*, 2012). Though its efficacy in treating these conditions is evident in some cases, the precise neurological effects of TMS, in addition to DBS and ECT, are not understood. Previous studies highlight that TMS can influence neural activity within populations in a range of ways. Initial synchronous depolarisation, followed by longer-lasting GABAergic inhibition (Siebner *et al.*, 2009) impacts on neuronal excitability (Lang *et al.*, 2007) and the excitatory/inhibitory balance (Iwabuchi *et al.*, 2017), can drive neural plasticity (Fung and Robinson, 2014), and alter patterns of coherence between brain regions, leading to the reorganisation of functional connectivity networks (Tik *et al.*, 2017; Iwabuchi *et al.*, 2017). In chapters 6 and 7 we use computational and analytical methods to study the effects of TMS on simulated FC networks to explore how these transitions arise.

2.1.5 Shortcomings of neuroimaging

One of the main issues with the current state of neuroimaging is the trade-off between spatial and temporal resolution (Babiloni *et al.*, 2009). EEG, for example, is able to record changes in electrical conductance over very short timescales, with typical sampling rates in the order of 100 Hz, but due to the currents being distorted by resistive matter, most notably the skull, it is not possible to locate the source accurately. MEG and fMRI offer better spatial resolution, but they suffer from requiring much more expensive equipment and more technically demanding experiments. They also require the patient to be stationary to achieve accurate data, since the final image depends on localised cortical signals which will overlap and blur if the sources move during a scan, which restricts task-based experiments and situations where movement is involuntary such as for epilepsy sufferers (Ray and Bowyer, 2010). However, a wearable MEG scanner has recently been developed that offers promise for future research into motor-based disorders (Boto *et al.*, 2018). This is a significant step towards mapping human electrophysiology of people of all ages and neurological conditions, where subjects are free to move and interact with their environment.

Computational models are increasingly utilised in the field if neuroscience; advanced computing facilities, more sophisticated models and greater data assimilation are helping to reveal the relationship between the brain's structure and function (Breakspear *et al.*, 2010; Stam *et al.*, 2016) and the origin of resting state networks (Deco *et al.*, 2013). The major advantage of computational methods is that the brain can be investigated without recourse to expensive and sometimes invasive experimentation. Another benefit of this style of research is that researchers have complete control over simulated experimental conditions, side-stepping some of the real-world problems that hamper empirical studies; for instance, interference from external electromagnetic fields. This is especially useful in modelling brain stimulation, where brain imaging instruments can be at risk of interference from the source of stimulation itself (Ilmoniemi and Kičić, 2010). In a clinical setting, the computational study of the brain is helping to provide new methods of treatment in cases where a condition may be responding poorly to drugs (Kuhlmann *et al.*, 2015). For instance, in Wang *et al.* (2014) the authors identify and analyse dynamical mechanisms for drug-resistant focal epilepsy, giving hope that such research may be used to better inform clinical researchers to help provide better treatment for patients.

With this in mind, we shift focus to a theoretical perspective of neuroscience and in the following section give an overview of the mathematical ideas that reveal the underpinnings of the computational work pursued in the technical chapters of this thesis.

2.2 Mathematical Background

2.2.1 Modelling neural activity

In this section we discuss a variety of models that have been instrumental in the field of theoretical neuroscience. For a more detailed overview, we refer the reader to Ashwin *et al.* (2016). These can be broadly divided into two categories: those that aim to describe the action potential dynamics of individual neurons and those that reduce the complex interactions of large neural networks to state variables describing some average measure of activity.

In the pioneering work of Hodgkin and Huxley (1952), the authors presented one of the first models of neuro-electrical activity. Derived from voltage-clamp experiments on the squid giant axon, their non-linear system of equations characterises the temporal evolution of sodium and potassium currents. This work accelerated research into a family of models known as spiking neuron models, since they can be used to simulate the rapid depolarisation/repolarisation spikes that takes place when a neuron fires an action potential. Although

Hodgkin and Huxley's model provides a detailed description of ionic conduction that aids in studying action potential generation, its complexity allays practicality at the network level. Integrate-and-fire models simplify spiking dynamics by introducing a discontinuous resetting at some voltage threshold value (Lapique, 1907).

While this class of models has provided an excellent insight into neural behaviour on the cellular level, their ability to explain the macroscale behaviour of millions of neurons that contribute to brain rhythms observed in EEG recordings is limited, since the interactions that occur on the cellular scale are too vast in number and complexity to be feasibly characterised by such models. In the 1970s, there was much interest in developing models to confront this issue, which tracked the behaviour of large neural populations and their interactions (Da Silva *et al.*, 1974; Wilson and Cowan, 1972; Freeman, 1978). The necessity of this was to develop models that could accurately describe the higher functions of the brain, such as sensory processing and memory, which could not be captured effectively by single-neuron models (Wilson and Cowan, 1972). Typically phenomenological in nature, these so-called *mean field models* consider populations of neurons that exhibit excitatory or inhibitory behaviour computed on a continuous spatial domain or discrete points, which, in the latter case, are typically referred to as *neural mass models* (NMMs). In general terms, NMMs take a population average over the distribution of expectant states of neuronal populations (Deco *et al.*, 2008). Therefore, the main assumption made by NMMs is that neurons are statistically identical, allowing for computational efficiency when simulating the large-scale neural activity thought to be implicated in higher brain function (Breakspear, 2017). Due to the nature of this reduction, NMMs are incapable describing behaviour on the level of neurons and neural ensembles but, have been successful in replicating the EEG rhythms that they were originally designed to simulate (David and Friston, 2003). In this framework, neurons preferentially activate synchonously and interactions are mediated by firing rates rather than action potentials (David and Friston, 2003). Crucially, NNMs are beneficial for modelling large-scale brain networks, with which we mostly concern ourselves in this thesis.

Wilson–Cowan model

Wilson and Cowan (1972) designed their model, one of the first and simplest NNMs, on the assumption that cortical dynamics emerges from the interplay between excitatory and inhibitory activity, discounting the role played by subcortical structures. Nevertheless, it has been successful is describing a range of neurological phenomena including visual hallucinations (Bressloff *et al.*, 2002; Bertalmío *et al.*, 2020) and epilepsy (Wang *et al.*, 2014).

The model describes the nonlinear interactions two populations (see Figure 2.5) with mean numbers of activated and quiescent excitatory and inhibitory neurons, given by u and v respectively, whose dynamics governed by two first-order differential equations:

$$\begin{aligned} \dot{u} &= -u + s(c_1 u - c_2 v + P), \\ \dot{v} &= -v + s(c_3 u - c_4 v + Q). \end{aligned} \tag{2.1}$$

In (2.1) $c_{1,\ldots,4}$ represent inter- and intra-population coupling strengths, P and Q are extra-cortical input (from the thalamus, for example) and s is a non-linear firing-rate function called a sigmoid that saturates asymptotically at high levels of neural activity, *e.g.*:

$$s(x) = \frac{1}{1 + e^{-x}}. \tag{2.2}$$

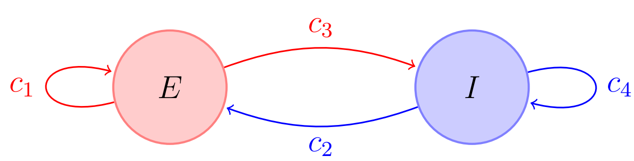

Figure 2.5: Wilson–Cowan node. Schematic for the two-population couplings described by the system (2.1). Red/Blue colours indicate respectively excitatory/inhibitory populations and their efferent couplings.

A key feature of the Wilson–Cowan model is its ability to produce oscillations, which can be viewed as a simple representation of brain rhythms to simulate large-scale brain activity. We can deduce where oscillations are stable in (2.1) via its *bifurcation* set, which is a map of qualitative changes in the nature of the solution set, given over some range of parameter values. For instance, Figure 2.6 shows two bifurcation sets: saddle nodes, by which the number of fixed point solutions changes and super-critical Hopf bifurcations, by which stable oscillations emerge. The oscillatory solution in stable in the central region of the diagram bounded by these two sets. We discuss the nature of bifurcations and how they are derived in greater depth in section 3.3.

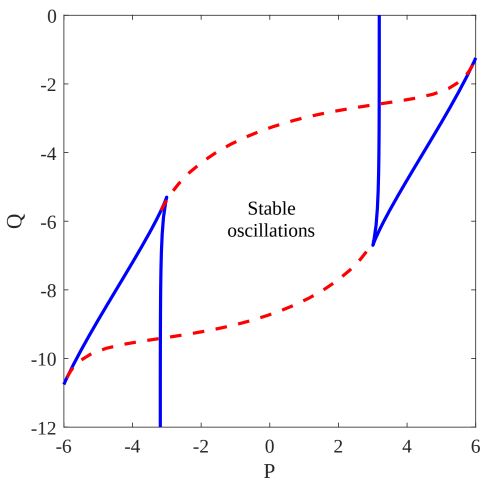

Figure 2.6: Wilson–Cowan bifurcations. Bifurcation structure of the system (2.1) in (P, Q) parameter space. Blue lines indicate saddle nodes of fixed points while red dashes are super-critical Hopf sets.

Jansen–Rit model

Following from the Wilson–Cowan model, which became a popular tool for theoretical neuroscientists to investigate neural dynamics at a population level, Jansen and Rit (1995) developed a model in a similar spirit. Their model takes greater inspiration from the biophysical connectivity of neuronal populations in order to replicate the rich dynamics of EEG activity associated with evoked potentials due to visual stimuli. The model was itself based on a previous model by Da Silva *et al.* (1974) which attempted to amalgamate population level effects into state parameters, sometimes referred to as

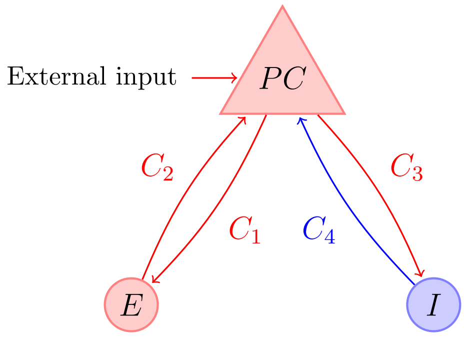

Figure 2.7: Wiring diagram for a Jansen-Rit network node. Excitatory/inhibitory populations and synaptic connections are highlighted in red/blue respectively. Interneurons (E, I) and pyramidal cells (PC) are interconnected with strengths C_i for $i = 1, \ldots, 4$.

a 'lumped-parameter' model.

While similar in spirit to the Wilson–Cowan model, the Jansen–Rit model describes the evolution of the average post-synaptic potential (PSP) in three interacting neural populations: pyramidal cells (y_0), and excitatory (y_1) and inhibitory (y_2) interneurons (see Figure 2.7). These populations are connected with strengths C_i $(i = 1, \ldots, 4)$, representing the average number of synaptic connections between each population. The Jansen–Rit model is mathematically described by a second order differential linear transform that converts firing frequency into an electrical potential, which results in six first order equations by adopting the notation $(y_0, \ldots, y_5)$ for the dependent variables. The pairs (y_0, y_3), (y_1, y_4), and (y_2, y_5) are associated with the dynamics of the population average of PSPs and their temporal derivatives:

$$
\begin{aligned}
\dot{y_0}(t) &= y_3(t), \quad \dot{y_1}(t) = y_4(t), \quad \dot{y_2}(t) = y_5(t), \\
\dot{y_3}(t) &= Aa\mathrm{Sigm}(y_1(t) - y_2(t)) - 2ay_3(t) - a^2 y_0(t), \\
\dot{y_4}(t) &= Aa\{P(t) + C_2\mathrm{Sigm}(C_1 y_0)\} - 2ay_4(t) - a^2 y_1(t), \\
\dot{y_5}(t) &= BbC_4\mathrm{Sigm}(C_3 y_0(t)) - 2by_5(t) - b^2 y_2(t).
\end{aligned}
\tag{2.3}
$$

The function f is a sigmoidal nonlinearity that can be viewed as an analogue of (2.2), which represents the transduction of activity into a firing rate:

$$f(v) = \frac{\nu_{\max}}{1 + \exp(r(v_0 - v))} = \nu_{\max} s(r(v - v_0)). \tag{2.4}$$

This model is employed and discussed in greater depth in chapter 4.

Wendling model

A significant extension of the Jansen and Rit's model came with the work of Wendling *et al.* (2002). Again, with the aim of replicating EEG activity, the authors were specifically interested in producing rhythms similar to those observed from epileptic patients during, and between, seizure onset.

Their extension to Jansen and Rit's model arises from the research suggesting that GABAergic inhibition operates at two different timescales: a fast one near the soma and a slow one near the dendrites (Miles *et al.*, 1996). Therefore, a second inhibitory neural population is added, again forming a feedback loop between the pyramidal population (similarly to the other interneuron populations in Figure 2.7) as well as receiving input from the other inhibitory population. Mathematically, this adds four more first-order ODEs to the system (2.3) to describe the PSPs of the fast inhibitory population y_3 as well as the PSPs of neurons connecting the inhibitory populations y_4. These are constructed in similarly to the the ODEs in (2.3):

$$\begin{aligned}
&\dot{y_0}(t) = y_5(t), \quad \dot{y_1}(t) = y_6(t), \quad \dot{y_2}(t) = y_7(t), \quad \dot{y_3}(t) = y_8(t), \quad \dot{y_4}(t) = y_9(t),\\
&\dot{y_5}(t) = Aa\mathrm{Sigm}(y_1(t) - y_2(t) - y_3(t)) - 2ay_5(t) - a^2 y_0(t),\\
&\dot{y_6}(t) = Aa\{P(t) + C_2\mathrm{Sigm}(C_1 y_0)\} - 2ay_6(t) - a^2 y_1(t),\\
&\dot{y_7}(t) = BbC_4\mathrm{Sigm}(C_3 y_0(t)) - 2by_7(t) - b^2 y_2(t),\\
&\dot{y_8}(t) = GgC_7\mathrm{Sigm}(C_5 y_0(t) - y_4(t)) - 2gy_8(t) - g^2 y_3(t),\\
&\dot{y_9}(t) = BbC_6\mathrm{Sigm}(C_3 y_0(t)) - 2by_9(t) - b^2 y_4(t).
\end{aligned} \tag{2.5}$$

The added dynamic complexity of this model allowed the authors to replicate a variety of biologically relevant rhythms related to epileptic-like activity.

This was further utilised in Goodfellow *et al.* (2016) to develop a framework to predict optimal surgical strategies to treat epileptic patients.

Next-generation neural mass model

A recent development in NNMs has been the development of a class of models which describe exact mean-field descriptions of coupled neural oscillators (Bick *et al.*, 2020). An archetypal *next-generation* NMM, outlined in (Coombes and Byrne, 2019), tracks the evolution of intra-population synchrony of a population of quadratic integrate-and-fire neurons, Synchronous firing of neurons is highly pertinent to neuroimaging since it can modulate the spectral power of brain rhythms (Uhlhaas and Singer, 2006; Buzsáki *et al.*, 2013). This is achieved through a mean-field reduction of the phase density distribution via the Ott-Antonsen ansatz (Ott and Antonsen, 2008), which provides a method to derive a quantification of synchrony for globally coupled oscillatory systems (via Kuramoto order parameters, which are described in section 2.2.2) in the infinite-oscillator limit. This model is further discussed and implemented in chapters 6 and 7 and we point the reader to Byrne *et al.* (2020) and Bick *et al.* (2020) for recent reviews.

2.2.2 Coupled oscillators

The emergence of synchronisation in biology is ubiquitous, as exemplified by the synchronised flashing of fireflies in southeast Asia (Strogatz, 2004), and its mathematical basis is a rich area of research. Winfree (1967) was one of the first to formulate a mathematical network model for the emergence of synchronisation by pursuing a mean-field approach, whereby the complex interactions of a large number of oscillating units, each given by a first-order ODE, could be reduced to an average influence on the whole network. Through his model, Winfree showed that synchronisation was a threshold phenomenon: when the coupling strength of oscillators exceeded some critical value, oscillators spontaneously synchronised their frequencies (Ariaratnam and Strogatz, 2001).

Kuramoto (1975) continued this line of research to develop a highly simplified model of coupled phase oscillators,

$$\dot{\theta}_i = \omega_i + \frac{K}{N}\sum_{j=1}^{N}\sin(\theta_j - \theta_i), \tag{2.6}$$

for oscillatory units $i = 1, \ldots, N$ coupled with strength K, and with natural frequency ω_i and phase $\theta_i \in [0, 2\pi)$. When all units have the same natural frequency, the convention of using a sinusoidal coupling function allows for synchrony to be a fixed point of the system ($\theta_j - \theta_i = 0$). Kuramoto investigated synchrony by defining 'order parameters' r and ψ, pertaining to the degree of coherence and average phase respectively:

$$re^{i\psi} = \frac{1}{N}\sum_{j=1}^{N} e^{i\theta_j}. \tag{2.7}$$

Using the order parameter representation of the model (2.6), Kuramoto (1975) showed that, similarly to Winfree, there was a threshold $K = K_c$ at which the oscillators would (partly) synchronise. Moreover, for natural frequencies ω_i, chosen from a Lorentzian distribution $g(\omega)$, the r value could be derived exactly as $\sqrt{1 - (K_c/K)}$, where $K_c = 2\gamma$ and γ is the width of $g(\omega)$ at half maximum.

Substituting the sinusoidal coupling for different functions allows the model to explore a greater dynamic repertoire. A review of the dynamical nature of the Kuramoto model is presented in Acebrón *et al.* (2005) but briefly, in different conditions, oscillators may phase-lock (have constant phase difference), frequency-lock (have constant frequency difference) or behave chaotically, where no uniform pattern emerges. This is particularly relevant in the context of neural simulation since coherence patterns are important in describing emergent function of neural populations.

2.2.3 Network properties of the brain

Another area of mathematical research that is highly important for this study is the field of network science. Analysis of structural brain networks has uncovered, perhaps unsurprisingly, a highly non-trivial organisation of connectivity.

The human connectome (Sporns, 2011; Van Essen *et al.*, 2013), which reflects white matter tracts connecting large-scale brain regions, is divided into two hemispheres with relatively few connections between them. Within the hemispheres are densely connected intra-hemispheric 'rich clubs' of brain regions (Van Den Heuvel and Sporns, 2011; Betzel *et al.*, 2016), while only a few highly-connected 'hubs' (van den Heuvel and Sporns, 2013; Oldham and Fornito, 2018) link to other rich clubs. This fragmentation repeats within these clusters and forms what is known as a hierarchical organisation (Meunier *et al.*, 2010; Sporns and Betzel, 2016).

It has also been shown that the connections of the brain are organised in such a way so as to minimise path length between regions, known as small-world achitecture (Bassett and Bullmore, 2006; Liao *et al.*, 2017). The brain does this through 'economical wiring' (Bullmore and Sporns, 2012; Betzel *et al.*, 2017), the efficient organisation of connections in order to minimise the amount of white matter tracts required.

An emerging concept of the study of brain networks is delineating the types of connections which exist in the brain by building networks with several layers, called multiplexes (Battiston *et al.*, 2014), with each layer containing connections that characterise a single class of interaction. For example, a method for determining a multiplex representation of FC where each layer corresponds to temporal coherence in a particular frequency band was recently described in Buldú and Porter (2018). The extension of network metrics to multiplexes can explain topological features unobtainable by standard single-layer approaches. Indeed, multiplex descriptions of the brain have been found to better explain the FC irregularities associated with schizophrenia (De Domenico *et al.*, 2016) and Alzheimer's disease (Cai *et al.*, 2020).

In Crofts *et al.* (2016), a two-layer approach is used to investigate structure function relations using a novel metric which determines the degree to which the functional layer improves the transistivity of the network, compared to the monolayer structure. We will expand upon this work in chapter 5 and generalise the metric to weighted SC and FC.

2.3 Aims and Scope

We have briefly introduced the ideas that are crucial to motivating the research conducted in this thesis. Much of this work has been driven by the abundance of neuroimaging data currently available which has deepened our understanding of cognition and other complex brain functions but also posed interesting questions for which large-scale brain modelling may be able to provide an answer. Though there exists much structural and functional connectivity data of large-scale brain networks, their relation is not entirely clear. The brain's ability to support a diverse range of functions from such a static network has particular relevance when considering the challenges of understanding transcranial brain stimulation, in particular how it is so effective at treating conditions associated with disrupted functional connectivity, while operating within a much more static structural network. In this thesis, we explore these issues through the lens of computational models with the hope of shedding new light of the dynamical nature of the brain and the networks that quantitatively describe it.

Chapter 3

Mathematical Methods

The work presented here, being theoretical in nature, has its basis in a variety of mathematical methodologies. We therefore use this chapter to consolidate and delineate the technical mathematical nomenclature and theory frequently used throughout this thesis, which will serve as a toolkit that we will refer back to during our research into dynamical neural networks.

3.1 Network analysis

3.1.1 Graph theory of networks

The discussion of brain networks in this thesis is highly reliant on nomenclature and notation used in graph theory, the field of mathematics which concerns the theoretical study of network structure. We consider such network approaches in chapter 5, but we give an overview of some of the key concepts here.

A graph $G(E, V)$ is composed of a set of n vertices $V = v_1, \ldots, v_n$ and m edges $E = e_1, \ldots, e_m$, where each edge e_i represents a pair of vertices. If the graph is undirected, this pair is unordered as a connection exists in both directions between the vertices. Otherwise, the edge is an ordered pair v_j, v_k which describes a directed path from v_j to v_k. The sum of the edges centred on each node is its degree, D. If G is weighted, there is an associated function $\mathbf{w} : E \to \mathbb{R}^m$ to supply weights for each edge. There exist a myriad different

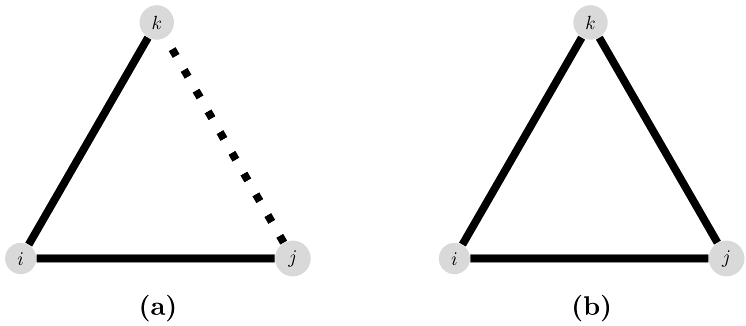

Figure 3.1: Three-node structures: We denote connected sets of three nodes, centred on an arbitrary node i, as (a) open triads, where an edge may exist between j and k and (b) closed triads, where we force the condition that an edge lies between j and k so that the edges form a loop.

metrics by which to measure the connectivity of graphs to determine, for instance, how efficiently connected the graph is or how robust its connectedness is to having parts of the graph removed. Here, we introduce some commonly used metrics that are employed in this thesis to evaluate the topology of brain networks. These are standard concepts in network science and we refer the reader to Newman (2018) for a comprehensive discussion of their formulation and wider applications.

Clustering

Clustering is commonly used in the study of social networks; a motivating question for this metric is to ask how likely a pair of mutual friends are also friends with each other. In more general terms, this measures the proportion of triadic structures (connected sets of three nodes) in a given network that form a loop, which has consequences for feedback within a network. Moreover, in the context of neural activity, the clustering coefficient is a biomarker for the specialised processing that occurs within densely interconnected groups of brain regions (Rubinov and Sporns, 2010b).

A schematic of triadic relationships is shown in Figure 3.1. For an arbitrary node i, the n_i nodes connected to i have a maximum of $n_i(n_i - 1)/2$ connections between them. The local clustering coefficient is simply the fraction of these that exist. It is convenient to represent this in the form introduced in Battiston *et al.* (2014),

$$c_i = \frac{\sum_{j \neq i} \sum_{k \neq i} a_{ij} a_{jk} a_{ki}}{\sum_{j \neq i} \sum_{k \neq i} a_{ij} a_{ki}}, \tag{3.1}$$

for an arbitrary undirected, unweighted network described by some binary matrix A, with elements a_{ij} (= 1 if an edge exists between node i and j, = 0 if not), that is simple (*i.e.* without self-loops so $a_{ii} = 0$ for all nodes i).

Local clustering can reveal the presence of communities in a given network, subsets of nodes which are strongly connected to other members but much less so to nodes outside the community. This is particularly useful for quantifying the modular hierarchy of the brain since it arises from these types of network motif (Meunier *et al.*, 2010; Sporns and Betzel, 2016; Boly *et al.*, 2012).

Centrality

In some networks, such as scale-free networks, certain nodes are much more highly connected and thus exert much more influence on network dynamics. This motivates the quantification of the relative importance of nodes in a network, called centrality scores. However, 'importance' is a rather ambiguous term with multiple interpretations. One definition is simply the nodal degree, using the logic that more highly connected nodes will exert more influence, though this does not capture the impact of higher-order interactions. Eigencentrality determines scores on the principle that nodes connected to important nodes will themselves be more significant than if they were instead connected to nodes of less importance. In this case, a node's score x_i is proportional to the sum of scores from the set of efferently connected nodes, where components of the binary adjacency matrix $a_{ij} = 1$:

$$x_i = \frac{1}{\lambda} \sum_j a_{ij} x_j, \tag{3.2}$$

where $1/\lambda$ is some constant of proportionality. By rearranging we form an eigenvalue problem, $A\mathbf{x} = \lambda\mathbf{x}$, where $\mathbf{x}$ is a vector of centrality scores and λ is chosen to be the dominant eigenvalue.

Connectivity

Like most real-world networks, especially in biology, brains are fallible systems that are prone to lesions and degeneration. It is therefore of interest to replicate this mathematically, and test the robustness of a network, by removing edges and nodes from a network to deduce the changes in connectedness. A graph is said to be connected when there exists a path from one node to every other, which means that every node can to some degree communicate with all the others. Without this important property, two or more subsets of nodes in a network will have completely independent dynamics, which is not physically realistic for a network such as the brain whose function relies on many integrated processes. Edge and vertex connectivity is the minimum number of these that can be removed, respectively, to disconnect the graph.

3.1.2 Synchronisation of networks

One of the most well studied properties of dynamical systems is the proclivity of networks to synchronise or, more generally, exhibit certain temporally coherent behaviours. While we have discussed how synchronisation phenomena is commonly studied with regards to Kuramoto networks in the form of (2.6), we here discuss general analytical methods to predict coherence from the graph structure, in the case where network dynamics are not necessarily known.

Eigenmodes

The Kuramoto order parameters are useful for capturing the collective behaviour of many oscillators, but they do not give information about the phase relationships between individual units. The dynamics of complex networks of oscillators can be decomposed to underlying elements called ‘eigenmodes’, a term which arises from the natural modes of vibration exhibited by many real-world systems. The principle of eigenmode decomposition is that the response of a system of coupled oscillators to external perturbation can be viewed as the superposition of several eigenmodes, with each one corresponding to a particular natural frequency of oscillation. Mathematically, the eigenmodes of a coupled system can be represented as the eigenvalues and eigenvectors of its associated connectivity matrix. Indeed, it has been shown that brain networks' eigenstructures reflect both healthy function and pathological defects (Wang *et al.*, 2017).

In chapter 4 and 7 we will revisit the notion of eigenmodes to study the emergent behaviour of large-scale brain networks using spectral methods described by linear theory (see section 3.3).

Algebraic connectivity

The eigenstructure of networks has also been well-studied in relation to 'synchronisability', *i.e.* how amenable a network is to synchrony. This is largely based on the topology of the network and its degree of heterogeneity, since nodes with very different connectivity properties will be less likely to exhibit similar dynamics. This is quantitatively encapsulated in the *algebraic connectivity* of a network described by Fiedler (1973), which is derived from the eigenvalues of an alternative representation of a network graph called a *Laplacian.* For an adjacency matrix A, we define its corresponding Laplacian as $\mathcal{L} = D - A$, where D is the diagonal matrix of degrees of each vertex. The algebraic connectivity α, defined by the second smallest eigenvalue of the Laplacian, is a lower bound for the vertex connectivity ν, edge connectivity ν' and minimum degree δ of the graph: $\alpha \leq \nu \leq \nu' \leq \delta$.

3.2 Neural network notation

Here we outline the notation that will serve as a basis for the models we describe. In generality, we consider the dynamics of a set of N nodes on a graph, governed by variables $\mathbf{u}(t) \in \mathbb{R}^M$ and coupled according to a weighted adjacency matrix $W \in \mathbb{R}^{N\times N}$ with elements $w_{ij} \quad (i, j \in \{1, \dots, N\})$

characterising strength of connection from node j to i, which may be binary or weighted. A simple coupling convention is *additive coupling* introduced in Hopfield networks (Hopfield, 1982), where afferent inputs are summed. In this case, we write the temporal evolution of state variable as a system of first-order ODEs,

$$\frac{\mathrm{d}}{\mathrm{d}t}\mathbf{u}_i(t) = F(\mathbf{u}_i(t)) + G(L\mathbf{u}_i(t)) + \sum_j w_{ij} H(\mathbf{u}_j(t)), \tag{3.3}$$

with the intrinsic intra-mass dynamics governed by $F(\mathbf{u}(t)) + G(L\mathbf{u}(t)) \in \mathbb{R}^M$, where $L \in \mathbb{R}^{M \times M}$ is a local coupling matrix, and some non-local inter-mass coupling between nodes via a nonlinear interaction function $H(\mathbf{u}_j(t)) \in \mathbb{R}^M$.

Furthermore, in physical networks communication is not instantaneous so we may consider the addition of delays, τ_{ij}, characterising the time it takes for the output of a node (i) to be received by another (j):

$$\frac{\mathrm{d}}{\mathrm{d}t}\mathbf{u}_i(t) = F(\mathbf{u}_i(t)) + G(L\mathbf{u}_i(t)) + \sum_j w_{ij} H(\mathbf{u}_j(t - \tau_{ij})). \tag{3.4}$$

In addition to providing a regime that is amenable to the modelling we wish to pursue in this thesis, using ODE systems of the form of (3.3) and (3.4) allow us to exploit a variety of well-established analytical methods.

Before we consider some mathematical methods for ODE systems, we divert our attention to the networks whose dynamics they govern.

3.3 Linear theory

Dynamical systems modelling complex processes are often non-linear, which normally means it is difficult, or impossible, to determine their solutions. However, it is possible to analyse the nature of solutions near steady states, which are time-invariant solutions, through linear theory. In this case, we seek approximate dynamics for a general M-dimensional system of variables u_n and functions f_n for $n = 1, \dots, M$,

$$\begin{pmatrix} \dot{u}_1 \\ \vdots \\ \dot{u}_M \end{pmatrix} = \begin{pmatrix} f_1(\mathbf{u}) \\ \vdots \\ f_M(\mathbf{u}) \end{pmatrix}, \tag{3.5}$$

which is given by $\dot{\mathbf{v}} = J\mathbf{v}$, where $\mathbf{v} = (v_1, \dots, v_M)$ is a set of small perturbations from equilibrium and J is a Jacobian matrix that has the form

$$\begin{bmatrix} \frac{\partial f_1}{\partial u_1} & \cdots & \frac{\partial f_1}{\partial u_M} \\ \vdots & \ddots & \vdots \\ \frac{\partial f_M}{\partial u_1} & \cdots & \frac{\partial f_M}{\partial u_M} \end{bmatrix}, \tag{3.6}$$

evaluated at steady state.

For networks of the form (3.3), with dynamics for each of N nodes described by M ordinary differential equations (ODEs), we have Jacobians of size $MN \times MN$, which can be very large for networks of composed of many nodes, as is the case for the large-scale brain networks studied in this thesis. In the following section we consider a method to reduce the problem so that it is more amenable to our computational methods.

3.3.1 Linearisation of non-delayed systems

For the system described in (3.3), with M-dimensional node dynamics such that $\mathbf{u}_i = (u_{1_i}, \dots, u_{M_i})$ we have at steady state:

$$0 = F(\mathbf{u}_i^\star) + G(L\mathbf{u}_i^\star) + \sum_j w_{ij} H(\mathbf{u}_j^\star). \tag{3.7}$$

We linearise around this state by writing $\mathbf{u}_i(t) = \mathbf{u}_i^\star + \mathbf{v}_i(t)$ for some set of small perturbations $\mathbf{v}_i(t) \in \mathbb{R}^M$ for $i = 1, \dots, N$, with $|\mathbf{v}_i(t)| \ll 1 \quad \forall \quad i$. Substitution into (3.3) and expanding to first order gives:

$$\frac{\mathrm{d}\mathbf{v}_i}{\mathrm{d}t} = [DF(\mathbf{u}_i^\star) + DG(L\mathbf{u}_i^\star)L]\,\mathbf{v}_i + \sum_j DH(\mathbf{u}_j^\star) w_{ij} \mathbf{v}_j, \tag{3.8}$$

where $DF, DG, DH \in \mathbb{R}^{M\times M}$ are Jacobians. It is now useful to define $D\mathbf{F}_i = DF(\mathbf{u}_i) + DG(L\mathbf{u}_i^\star)L$ and $D\mathbf{G}_j = DH(\mathbf{u}_j^\star)$ so that $D\mathbf{F}_i$ is the Jacobian which describes the intra-mass dynamics of node i and $D\mathbf{G}_j$ is the Jabobian for the effect of the inter-mass interactions with node j. Then we may write (3.8) in the form

$$\frac{\mathrm{d}}{\mathrm{d}t}\mathbf{V} = \begin{bmatrix} D\mathbf{F}_1 & & 0 \\ & \ddots & \\ 0 & & D\mathbf{F}_N \end{bmatrix}\mathbf{V} + (W \otimes I_M)\begin{bmatrix} D\mathbf{G}_1 & & 0 \\ & \ddots & \\ 0 & & D\mathbf{G}_N \end{bmatrix}\mathbf{V}, \tag{3.9}$$

where $\mathbf{V} = (\mathbf{v}_1, \ldots, \mathbf{v}_N)^\intercal$, and $\otimes$ denotes the tensor product. This system can be simplified by considering the eigenvalues of the connectivity matrix $W \in \mathbb{R}^{N\times N}$ (with components w_{ij}). We introduce a matrix of normalised column eigenvectors, E, and a corresponding diagonal matrix of eigenvalues, $\Lambda = \mathrm{diag}(\mu_1 \ldots \mu_N)$, such that $WE = E\Lambda$. Imposing the change of variables $\mathbf{Y} = (E \otimes I_M)^{-1}\mathbf{V}$ transforms (3.9) to

$$\begin{aligned}\frac{\mathrm{d}}{\mathrm{d}t}\mathbf{Y} = (E\otimes I_M)^{-1} &\begin{bmatrix} D\mathbf{F}_1 & & 0 \\ & \ddots & \\ 0 & & D\mathbf{F}_N \end{bmatrix}(E\otimes I_M)\mathbf{Y} \\ + (E\otimes I_M)^{-1}(W\otimes I_M) &\begin{bmatrix} D\mathbf{G}_1 & & 0 \\ & \ddots & \\ 0 & & D\mathbf{G}_N \end{bmatrix}(E\otimes I_M)\mathbf{Y}.\end{aligned} \tag{3.10}$$

Assuming a homogeneous system such that $\mathbf{u}_i^\star$ is independent of i, which is natural for identical units with a network connectivity with a row-sum constraint so that $\sum_{j=1}^{N} w_{ij}$ is the same for all i, then we have a useful simplification $D\mathbf{F}_i = D\mathbf{F}$ and $D\mathbf{G}_i = D\mathbf{G}$ for all i. It is simple to establish that for any block diagonal matrix W of size $NM \times NM$, formed from N identical matrices of size $M \times M$, that $(E \otimes I_M)^{-1}W(E \otimes I_M) = W$. Moreover, using standard properties of the tensor operator, $(E \otimes I_M)^{-1}(W \otimes I_M) = (E^{-1}W) \otimes I_M =$

$(\Lambda E^{-1}) \otimes I_M = (\Lambda \otimes I_M)(E^{-1} \otimes I_M)$. Hence, (3.10) becomes

$$\frac{\mathrm{d}}{\mathrm{d}t}\mathbf{Y} = \begin{bmatrix} D\mathbf{F} & & 0 \\ & \ddots & \\ 0 & & D\mathbf{F} \end{bmatrix} \mathbf{Y} + \begin{bmatrix} \mu_1 D\mathbf{G} & & 0 \\ & \ddots & \\ 0 & & \mu_N D\mathbf{G} \end{bmatrix} \mathbf{Y}. \tag{3.11}$$

The system (3.11) is in a block diagonal form and so it is equivalent to the set of decoupled equations given by

$$\frac{\mathrm{d}}{\mathrm{d}t}\xi_p = \left[D\mathbf{F} + \mu_p D\mathbf{G}\right]\xi_p, \qquad \xi_p \in \mathbb{C}^M, \qquad p = 1, \dots, N. \tag{3.12}$$

This has solutions of the form $\xi_p = \mathbf{A}_p \mathrm{e}^{\lambda t}$ for some amplitude vector $\mathbf{A}_p \in \mathbb{C}^M$. For a non-trivial set of solutions we require $\mathcal{E}(\lambda; p) = 0$ where

$$\mathcal{E}(\lambda; p) = \det\left[\lambda I_M - D\mathbf{F} - \mu_p D\mathbf{G}\right], \qquad p = 1, \dots, N. \tag{3.13}$$

Solving $\mathcal{E} = 0$ for λ produces a set of eigenvalues indexed by p which describe the dynamic behaviour of the network near to steady state. Since local stability requires the real part of all eigenvalues to be negative, if one of these eigenvalues crosses the imaginary axis the solution can undergo either a saddle-node bifurcation ($\Re(\lambda) = 0 = \Im(\lambda)$) or a Hopf bifurcation ($\Re(\lambda) = 0$, $\Im(\lambda) \neq 0$).

3.3.2 Linearisation of delayed systems

In light of the conduction velocities that mediate the speed of travel of action potentials down axons, it is appropriate to analyse how the addition of these delays affect the stability of solutions.

Much of the linear analysis presented in section 3.3.1 carries forward to the delayed system (3.4), although we must amend the linearised system (3.8) to account for the delays of interactions due to the perturbation:

$$\frac{\mathrm{d}\mathbf{v}_i}{\mathrm{d}t} = \left[DF(\mathbf{u}_i^\star) + DG(L\mathbf{u}_i^\star)L\right]\mathbf{v}_i(t) + \sum_j DH(\mathbf{u}_j^\star) w_{ij} \mathbf{v}_j(t - \tau_{ij}), \tag{3.14}$$

Using the reduction techniques of the previous section, we recover the same spectral equation as (3.13) with the substitution:

$$\mu_p(\lambda) = \sum_{i=1}^{N}\sum_{j=1}^{N} w_{ij} e^{-\lambda\tau_{ij}} v_i^p v_j^p, \tag{3.15}$$

where v_p^i is the ith element of the pth normalised eigenvector and we have assumed the symmetry $w_{ij} = w_{ji}$ and $\tau_{ij} = \tau_{ji}$.

3.4 Weakly-coupled oscillator theory

Homogeneous networks of oscillators, whereby all nodes are described by the same dynamics, can be approximated to evolve on the same limit cycle if coupling is sufficiently weak as to make interactions between nodes negligible compared to the intrinsic node dynamics. These small interactions can, however, cause phase-shifts along the periodic orbit. In this case we can reduce the dynamics of a system to consider how its phase on the limit cycle evolves, with interactions between nodes only dependent on the instantaneous phase difference of connected nodes. These oscillator networks can therefore be represented as a Kuramoto-style oscillator network model:

$$\dot{\theta}_i = \omega + \sum_j w_{ij} I(\theta_j - \theta_i), \tag{3.16}$$

where $\omega = 2\pi/T$ represents the natural frequency of an uncoupled oscillatory node with period T and phase θ_i, and the second term determines phase changes arising from pairwise interactions between nodes. I is called the T-periodic *phase interaction function* which can be *derived* from the network dynamics such as in equation (3.3).

The phase interaction function I is determined in terms of two quantities. The first is the so-called phase response function $\mathbf{Q} \in \mathbb{R}^M$, that describes the response of an attracting limit cycle to a small perturbation. This can be computed by solving the *adjoint equation*, whereby we write the dynamics for a single uncoupled node of the form (3.3) as $\dot{\mathbf{u}} = \mathbf{F}(\mathbf{u})$, with $\mathbf{F}, \mathbf{u} \in \mathbb{R}^M$. Then the adjoint is given by the T-periodic solution of

$$\frac{\mathrm{d}}{\mathrm{d}t}\mathbf{Q} = -D\mathbf{F}^{\intercal}(\overline{\mathbf{u}}(t))\mathbf{Q}, \quad \langle \mathbf{Q}(0), \mathbf{F}(\overline{\mathbf{u}}(0)) \rangle = \omega \text{ and } \mathbf{Q}(t) = \mathbf{Q}(t+T). \quad (3.17)$$

Here $\overline{\mathbf{u}}(t)$ is a T-periodic solution of the node model and $\langle\ ,\ \rangle$ denotes a Euclidean inner product between vectors. The second ingredient comes from writing the physical interactions in terms of phases rather than the original state variables. This is easily done by writing $\mathbf{u}_i(t) = \overline{\mathbf{u}}(\theta_i/\omega)$. The phase interaction function is then obtained as

$$I(t) = \frac{1}{T}\int_0^T \mathrm{d}s \big\langle \mathbf{Q}(s), H(\overline{\mathbf{u}}(s+t)) \big\rangle. \quad (3.18)$$

The adjoint equation is readily solved numerically by backward integration in time (Williams and Bowtell, 1997), whilst the integral in (3.18) can be evaluated using numerical quadrature.

In order to analyse the stability of such functions, we note that when $\sum_j w_{ij} I(\theta_j - \theta_i)$ is constant for all nodes i, all nodes evolve on the limit cycle with a fixed phase difference, known as *phase-locking*.

For a given phase-locked state $\theta_i(t) = \omega t + \phi_i$ (where ϕ_i is the constant phase of each node), local stability is determined in terms of the eigenvalues of the Jacobian of (3.16), denoted by $\widehat{I}(\mathbf{\Phi})$ with $\mathbf{\Phi} = (\phi_1, \ldots, \phi_N)^{\intercal}$, with components:

$$[\widehat{I}(\mathbf{\Phi})]_{ij} = \varepsilon[I'(\phi_j - \phi_i)w_{ij} - \delta_{ij}\sum_{k=1}^{N} I'(\phi_k - \phi_i)w_{ik}]. \quad (3.19)$$

The globally synchronous steady-state, $\phi_i = \phi$ for all i, exists in a network with a phase interaction function that vanishes at the origin (*i.e.* $I(0) = 0$), or for one with a row-sum constraint, $\sum_j w_{ij} = \Gamma =$ constant for all i. Note that the emergent frequency of the synchronous network state is given explicitly by $\omega + \varepsilon\Gamma I(0)$. Using the Jacobian in (3.19), synchrony is found to be stable if $\varepsilon I'(0) > 0$ and all the eigenvalues of the graph Laplacian of the structural network,

$$[\mathcal{L}]_{ij} = -w_{ij} + \delta_{ij} \sum_k w_{ik}, \tag{3.20}$$

lie in the right hand complex plane. Since the eigenvalues of a graph Laplacian all have the same sign (apart from, in this case, a single zero value) then local stability is entirely determined by the sign of $\varepsilon I'(0)$. For example, for a globally coupled network with $w_{ij} = 1/N$ then the graph Laplacian has one zero eigenvalue, and $(N-1)$ other degenerate eigenvalues at -1, and so synchrony is stable if $\varepsilon I'(0) > 0$.

3.5 Summary

In this chapter we have laid the foundations of the mathematical analysis conducted in this thesis.

The constructs introduced here are touched upon in all chapters. Specifically, the network theory will be highly useful for network measures discussed in chapters 5 and 6. The linear theory techniques are applied in chapters 4 and 7 to investigate the dynamics of the Jansen–Rit and the next generation neural mass models respectively. Finally, weakly coupled oscillator theory is applied in the next chapter to determine the stability of phase-locking patterns and synchrony and, moreover, how these relate to structure–function relationships.

Chapter 4

The role of node dynamics in shaping functional connectivity

As noted in chapter 2, the link between underlying structural connectivity and emergent function is not fully understood. In this chapter, we present work published recently in *Network Neuroscience* (Forrester *et al.*, 2020) in which we treat this issue by combining neural mass modelling with connectome data.

Previous theoretical studies deploying anatomically realistic structural networks alongside neural mass models describing mean-field regional neural activity have been used to investigate the emergence of large-scale FC patterns (Honey *et al.*, 2007; Rubinov *et al.*, 2009; Crofts *et al.*, 2016; Deco *et al.*, 2013; Ponce-Alvarez *et al.*, 2015; Messé *et al.*, 2015; Breakspear, 2017). These findings suggest that through indirect network-level interactions, a relatively static structural network can support a wide range of FC configurations, though current models have not yet been able to accurately simulate the transitive states underpinning cognition (Petersen and Sporns, 2015).

In the context of mean-field models, simulated (typically time-averaged) FC has been found most strongly to resemble SC when the dynamical system describing regional activity is close to a phase transition (Stam *et al.*, 2016), and strong structure–function agreement is reported near Hopf bifurcations in Hlinka and Coombes (2012). Similarly, analysis of the dynamical systems underpinning neural simulations have shown to be a good fit to fMRI data when the system is near to bifurcation (Deco *et al.*, 2019; Tewarie *et al.*, 2018). These results provide a possible manifestation of the so-called critical brain dynamics hypothesis (Shew and Plenz, 2013; Cocchi *et al.*, 2017), which posits that the brain operates in a regime poised at a near a critical point between an attractor of complete inactivity another of high activity (Beggs and Timme, 2012).

Here we present a combined computational and mathematical study, which significantly extends the related works of Hlinka and Coombes (2012) and Crofts *et al.* (2016), to investigate how the detailed and rich dynamics of the intrinsic behaviour of neural populations, together with structural connectivity, combine to shape FC networks. We treat the issue of criticality by investigating how bifurcations of model solutions and stability of synchrony within the network organise features of emergent FC. Importantly, we find that restricting our mathematical analysis to the node is sufficient to explain some features of the structure–function relationship measured from simulations of neural activity.

4.1 Data acquisition

The connectome data we use for these analyses was estimated using diffusion MRI data recorded with informed consent from 10 subjects, obtained from the Human Connectome Project (HCP) (Van Essen *et al.*, 2013). Probabilistic tractography, as described in section 2.1.3, was employed to determine the paths of white matter tracts. The processing of the raw MRI data into the connectivity matrix employed in this chapter was conducted by Glasser *et al.* (2013), though we describe an overview of the techniques used here. Briefly, 60,000 vertices on the white/grey matter boundary surface for each subject were used as seeds for 10,000 tractography streamlines. Streamlines were propagated through voxels with up to three fibre orientations, estimated from distortion-corrected data with a deconvolution model (Jbabdi *et al.*, 2012; Sotiropoulos *et al.*, 2016). The number of streamlines intersecting each vertex on the boundary layer was measured and normalised by the total number of valid streamlines. This resulted in a 60,000 node structural matrix, which was further parcellated using the 78-node AAL atlas by computing the mean connectivity between all pairs of vertices within each region. This was used to describe connections between brain regions, providing an undirected (symmetric), weighted connectivity matrix. To enable a meaningful comparison between the network measures of SC and FC, the former reflecting the density of tractography streamlines and the latter that of correlated neural activity, we place them on a similar footing by thesholding and binarising, such that only the top 23% of the weights (ordered by strength) are retained; see Figure 4.1. Thresholding is a widespread technique for removing spurious connections that may not in fact be a realistic representation of brain connectivity. We note that our thresholding choice (that reduces the number of connections, while ensuring that the overall modular structure is unchanged) is commensurate with a recent study (Tsai, 2018), which employed DTI data averaged on the same brain atlas as used herein to consider thresholding approaches suitable to remove weak connections with high variability between ($n = 30$) different subjects. This threshold level is also chosen for consistency with SC data employed in a related study (Hlinka and Coombes, 2012). To generate nodal inputs with commensurate magnitudes, the structural connectivity matrix was normalised by row so that afferent connection strengths for each node sum to unity. This normalisation process permits some of the analysis that we undertake to help explain SC–FC relations in regards to stability of oscillations and synchronisation (in particular, results arising from the weakly-coupled oscillator theory outlined in section 3.4). The physiological consequence of normalisation is that the relative number of connective white matter fibres is considered to be the same for each node, though we justify this simplification by highlighting that the results we present herein are not crucially dependent on such a choice and so our conclusions generalise (see section 4.5.3).

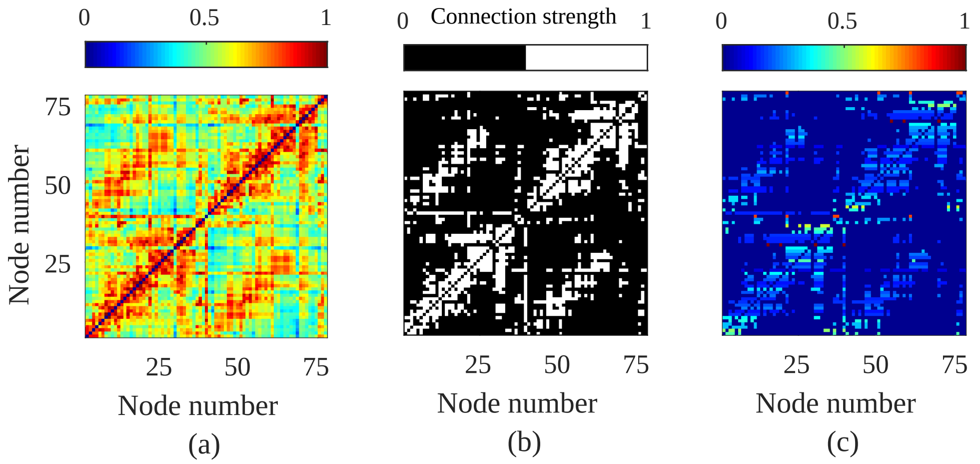

Figure 4.1: SC post-processing. The original structural matrix (a) is derived from DTI data taken from the Human Connectome Project database and parcellated on to a 78-region brain atlas. This is thresholded and binarised to keep the top 23% strongest connections (b) and normalised by row so that $\sum_{j=1}^{N} w_{ij} = 1$ for all regions i) in (c).

4.2 Analysis of the Jansen-Rit Model

Introducing an index $i = 1, \ldots, N$ to denote each node in a network of N interacting neural populations, we modify the $m = 6$ dimensional Jansen–Rit system of equations introduced in (2.3) with notation of the form of (3.3):

$$
\begin{aligned}
\dot{y}_{0_i} &= y_{3_i}, \qquad \dot{y}_{1_i} = y_{4_i}, \qquad \dot{y}_{2_i} = y_{5_i}, \\
\dot{y}_{3_i} &= Aaf\left(y_{1_i} - y_{2_i}\right) - 2ay_{3_i} - a^2 y_{0_i}, \\
\dot{y}_{4_i} &= Aa\left\{P_i + \varepsilon \sum_{j=1}^{N} w_{ij} f\left(y_{1_j} - y_{2_j}\right) + C_2 f\left(C_1 y_{0_i}\right)\right\} - 2ay_{4_i} - a^2 y_{1_i}, \\
\dot{y}_{5_i} &= BbC_4 f\left(C_3 y_{0_i}\right) - 2by_{5_i} - b^2 y_{2_i},
\end{aligned}
\tag{4.1}
$$

where,

$$
f(v) = \frac{\nu_{\max}}{1 + \exp(r(v_0 - v))}. \tag{4.2}
$$

The model is identical to that presented in Jansen and Rit (1995) for a single cortical column, but is completed by the specifying the network interactions as a function of average membrane potential of afferently connected pyramidal populations, encoded in a connectivity matrix with elements w_{ij}, with an overall scale of interaction set by ε. The remaining model parameters, together with their physiological interpretations and values (taken from Grimbert and Faugeras (2006), and Touboul *et al.* (2011)), are given in Table 4.1.

The model represents a population of pyramidal neurons receiving and sending signals between populations of inhibitory and excitatory interneurons (recalling the schematic for a single node in Figure 2.7), except that here we explicitly define external input to the PC population, which consists of an extracortical input P_i, as well as contributions from afferently connected nodes.

The Jansen–Rit model, defined by equation (4.1), adds complexity in relation to the similar study of Hlinka and Coombes (2012), in which the Wilson–Cowan model was employed. It can support oscillations that relate to important neural rhythms, such as the well known alpha, beta and gamma brain rhythms, and also irregular, epileptic-like activity (Ahmadizadeh *et al.*, 2018). Moreover, the model is able to replicate visual-evoked potentials seen in EEG recordings (Jansen and Rit, 1995), from which FC may be empirically measured (Srinivasan *et al.*, 2007).

4.2.1 Linear stability

A natural starting point to elucidate the nature of a mathematical model's solutions is through linear theory, which can be used to reveal the types of solutions the model supports. Here, we pursue this analysis for both the single node and network cases in order to deduce whether the network significantly impacts the resultant dynamics of the model.

Single Node bifurcations

Bifurcations for a single node are readily computed using the software package XPPAUT (Ermentrout, 2002), using A and B as the parameters of interest. The result is a Hopf and saddle-node set in parameter space, which bounds a region of oscillatory solutions. We also observe a region of bistability bounded by fold bifurcations of limit cycles, in which the types of activity

Parameter	Meaning	Value
C_1, C_2, C_3, C_4	Average number of synapses between populations	135, 108, 33.75, 33.75
P_i	Basal extracortical input to main pyramidal excitatory populations	120 Hz
A, B	Amplitude of excitatory, inhibitory PSPs respectively	$[2, 14]$ mV, $[10, 30]$ mV
a, b	Lumped time constants of excitatory, inhibitory PSPs	100 s^{-1}, 50 s^{-1}
ε	Global coupling strength	0.1
w_{ij}	Coupling from node j to i	$[0, 1]$
ν_{max}	Maximum population firing rate	5 Hz
v_0	Potential at which half-maximum firing rate is achieved	6 mV
r	Gradient of sigmoid at v_0	0.56 mV^{-1}

Table 4.1: Parameters in the Jansen–Rit model. Parameters appearing in equations (4.1) and (4.2) along with physiological interpretations and values/ranges used in simulations, which were taken from Grimbert and Faugeras (2006) and Touboul *et al.* (2011). In particular, the values of A and B, which modulate the strength of excitatory and inhibitory responses respectively, were chosen as the key control parameters for varying network activity.

described in Figure 4.2(a) and (c) can both exist. This is shown in Figure 4.3. We refer the reader to Grimbert and Faugeras (2006) Touboul *et al.* (2011) and Spiegler *et al.* (2010) for a comprehensive analysis of the bifurcation structure of the Jansen–Rit model.

Network bifurcations

The corresponding diagram for the full network requires numerical analysis of a much higher dimensional system, described by $N \times m = 78 \times 6 = 468$ ODEs; this is computationally demanding, and so we adopt the quasi-analytic approach of section 3.3 by linearising the full network equations around a fixed point. The resulting equations can be block-diagonalised (equation (3.11)) in the basis of eigenvectors of the structural connectivity, leading to a set of N equations (equation (3.13)), each of which prescribes the spectral problem for an m-dimensional system. Thus, each of these low dimensional systems can be easily treated without recourse to high performance computing. Moreover, this approach exposes the role of the eigenmodes of the structural connectivity matrix in determining the stability of equilibria. We report the locus of Hopf and saddle-node sets for the network in Figure 4.5. Comparison of Figures 4.3 and 4.5 shows that the bifurcation structure of steady states for the full network is practically identical to that of the single node. Indeed, the coupling strength ($\varepsilon = 0.1$) is chosen such that network interactions are significant, demonstrated by the weakly-coupled reduction being only marginally predictive of the full model here (discussed later in this chapter in section 4.5.2), highlighting the potential importance of single-node dynamics in driving SC–FC correlations.

4.2.2 False Bifurcations

In Figure 4.2 we consider in more detail the types of activity that the network model (4.1) supports. In particular, we observe that under changes to parameter values within the oscillatory region (see highlighted parameter values in Figure 4.3), the time-course of activity shifts from single- to double-peaked waves, which could have consequences for synchronisation of oscillations and, moreover, FC. The points of transition are known as *false bifurcations* since there is a significant dynamical change that occurs smoothly rather than critically. False bifurcations in a neural context have previously been seen as canards in single neuron models (Desroches *et al.*, 2013) as well as in EEG models of absence seizures (Marten *et al.*, 2009). In the latter case the false bifurcation corresponds to the formation of spikes associated with epileptic seizures (Moeller *et al.*, 2008). Indeed, the Jansen-Rit model has previously been shown to exhibit transient shifts between absence and background activity states by exploiting its bistable solutions (Goodfellow *et al.*, 2011).

As illustrated in Figure 4.2 the false-bifurcation transition is characterised by the change from a double-peaked profile (a) to a sinusoidal-like waveform (c) via the development of a point of inflection in the solution trajectory (b). Since this transition is not associated with a change in stability of the periodic orbit, these *false bifurcations* are determined by tracking parameter sets for which points of inflection occur. We refer the reader to Rodrigues *et al.* (2010) for details on methods for detecting and continuing false bifurcations in dynamical systems analytically. Here, however, we use a numerical approach, whereby the single-node system was integrated to a stable oscillatory orbit, then the number of local maxima in each period was measured. This divided the domain into two segments, for one and two local maxima. The interface between these regions gives the loci of false bifurcations. The result of this computation is shown in Figure 4.3, where we observe the set of false bifurcations arising from the breakdown of two branches of fold bifurcations of limit cycles. In the full network (not shown), this computation is more laborious (and there is some delicacy in defining the bifurcation since the network coupling leads nodes to inflect at marginally different parameter values); however, we obtain very similar results to those obtained in Figure 4.3 for a single node.

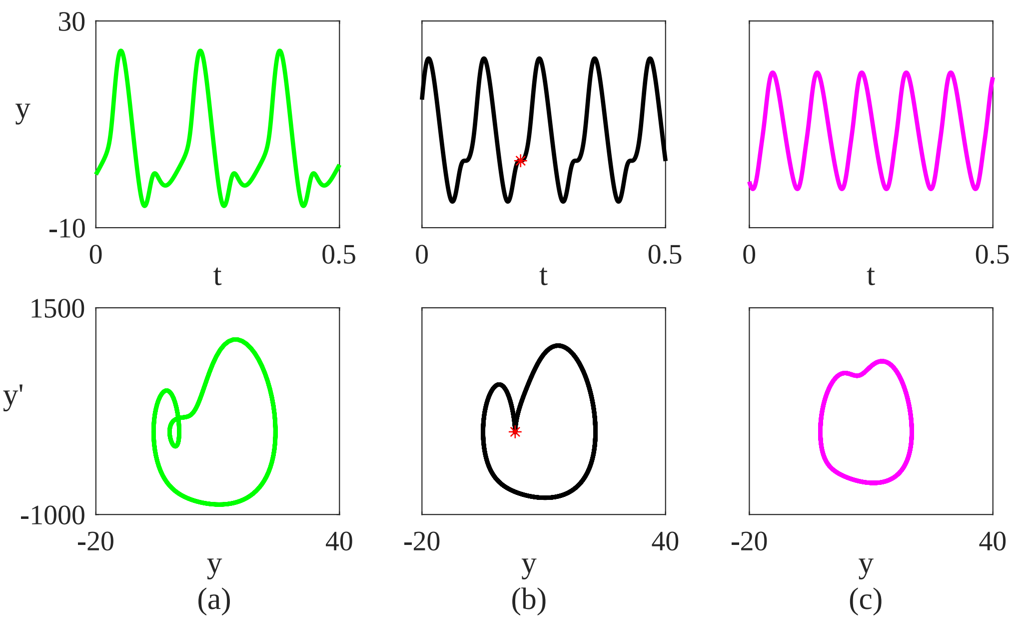

Figure 4.2: Activity profiles. Reporting $y = y_1 - y_2$, the potential of the main population of pyramidal neurons for a node in the Jansen–Rit network (1) in the absence of noise, with B fixed at 22 and (a) $A = 9.0$; (b) $A = 7.7$; (c) $A = 7.0$ and other parameter values as in Table 4.1. Subfigures in the upper row are plots of the time-series solution, whereas the bottom row shows the trajectories of stable orbits in the (y, y') plane. The chosen parameters lie at either side of the region where a smooth transition between activity types occurs, corresponding to a *false bifurcation* (see highlighted parameter values in Figure 4.3). In (b), an inflection point occurs and is highlighted as a red star on the orbit.

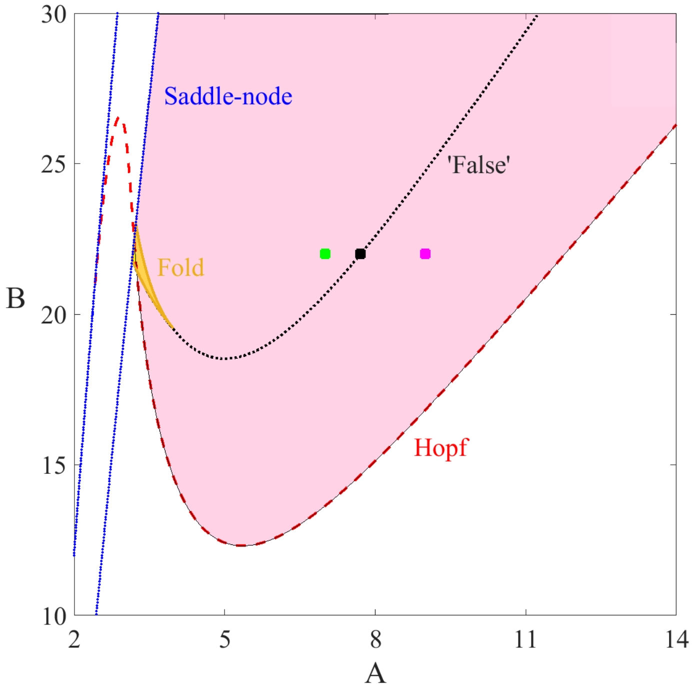

Figure 4.3: Two-parameter bifurcation diagram. Bifurcation sets in the (A, B) plane for the single-node case of the Jansen–Rit system of equations (4.1). Other parameter values are as stated in Table 4.1. Red dashes are Hopf bifurcations, black dots are false bifurcations and blue lines represent saddle points. There is also a region of bistability, highlighted in yellow, which is bounded by saddle nodes and a set of fold bifurcations of limit cycles. The pink and yellow shaded regions indicates parameter values for which there exist stable oscillatory solutions. The three coloured dots at $B = 22$, $A = 7.0,\ 7.7,\ 9.0$ indicate parameter values at which we observe distinctly different dynamics as shown in Fig. 4.2.

4.3 Computational methods

In this section we outline the numerical methods used to generate time-series solutions of Jansen–Rit network dynamics and how these are used to generate FC matrices.

4.3.1 Forward simulations

In what follows, we consider the patterns of dynamic neural activity that arise under systematic variation of the model parameters A and B, these being chosen as the parameters of interest because they govern the interplay between inhibitory and excitatory activity, which would typically vary due to neuromodulators in the brain (Rich *et al.*, 2018). It is known that a single Jansen–Rit node can support multi-stable behaviour which includes oscillations of different amplitude and frequency, for example in the yellow region bounded by fold points in the bifurcation diagram of Figure 4.3. Moreover, a network of these nodes can also exhibit various stable phase-locked states. However, we showed in section 3.4 that a globally synchronous steady state also exists in the network, which is physiologically unrealistic in terms of the complex patterns of FC that we concern ourselves with. In order to drive the system away from global synchrony and allow the system to explore a variety of dynamical states, a small amount of white noise is added to the extracortical input P_i on each node: $P_i + \mathrm{d}W_i(t)$, where $\mathrm{d}W_i(t)$ is chosen at random from a Gaussian distribution with standard deviation 10^{-1} Hz and mean 0 Hz. For direct simulations of the network we use an Euler–Murayama scheme,

$$\mathbf{Y}_{n+1} = \mathbf{Y}_n + \mathbf{F}(\mathbf{Y}_n)\mathrm{d}t + \mathrm{d}\mathbf{W}, \tag{4.3}$$

where $\mathbf{Y}_n$ is the vector of dependent variables at the n^{th} timestep, $\mathbf{F}(\mathbf{Y}_n)$ is the network dynamics given by the RHS of (4.1), $\mathrm{d}\mathbf{W}$ is the vector of additive noise and $\mathrm{d}t$ is the integration timestep. This numerical method was implemented in Matlab®, with a fixed numerical time-step of 10^{-4}, which we have confirmed ensures adequate convergence of the method (Figure 4.4), and a total time of 500 seconds (of which the first 40 seconds were omitted to remove initial transients from the time series data).

4.3.2 FC network construction from time-series

In view of the non-linear oscillations supported by the network model given by (4.1), functional connectivity networks are obtained by computing the commonly-used metric of mean phase coherence (MPC; Mormann *et al.* (2000)), which determines correlation strength in terms of the proclivity of two oscillators to phase-lock, giving a range from 0 (completely desynchronised) to 1 (phase-locking). We choose $y_j = y_{1_j} - y_{2_j}$ as the variable of interest because of its relation to the EEG signal, making it a good candidate to produce time-series more readily comparable with empirical data. Pairwise MPC measures

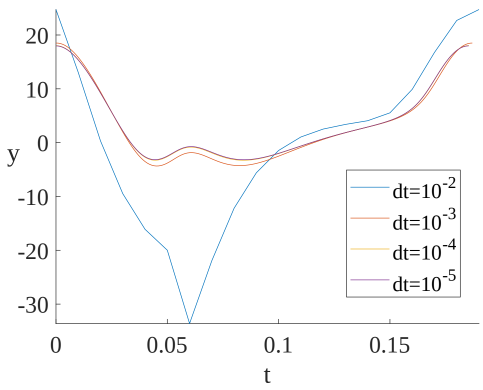

(a)

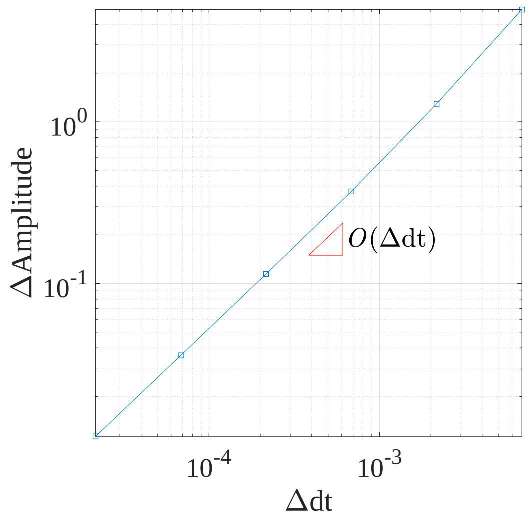

(b)

Figure 4.4: Convergence of the Euler–Maruyama scheme for integrating the Jansen–Rit system. (a) Example trajectories of the solution $y_i = y_{1_i} - y_{2_i}$ obtained from a single node under identical Brownian driving paths, for different numerical timesteps, as indicated in the legend. (b) Convergence of the error in the expectation of the solution y for different timestep choices, showing linear proportionality between the change in the amplitude of oscillatory solutions ΔAmplitude and change in timestep Δt, indicating optimal convergence of the method.

the average temporal variance of the phase difference $\Delta\phi_{jk}(t) = \phi_j(t) - \phi_k(t)$, between two time-series indexed by j and k, where here the instantaneous phase $\phi_j(t)$ is obtained as the angle of the complex output resulting from application of a Hilbert transform to the time-series, $y_j(t)$,

$$\phi_j(t) = \frac{1}{\pi}\int_{-\infty}^{\infty} \frac{y_j(\tau)}{t-\tau} d\tau, \tag{4.4}$$

which is computed using Matlab®'s built-in `hilbert` function. The mean phase coherence of the time-series comprising M time-points t_l $(l = 1, \ldots, M)$ is defined as:

$$R_{jk} = \left| \frac{1}{M} \sum_{l=1}^{M} \mathrm{e}^{i\Delta\phi_{jk}(t_l)} \right|, \tag{4.5}$$

which we computed as an average over the entire time series.

Structure–function relations are assessed by computing the Jaccard similarity coefficient (Jaccard, 1912):

$$J(X, Y) = \frac{\sum_i \sum_j \min\{x_{ij}, y_{ij}\}}{\sum_i \sum_j \max\{x_{ij}, y_{ij}\}}, \tag{4.6}$$

for two matrices X and Y of the same size, with elements x_{ij} and y_{ij} respectively. When calculated for the non-diagonal entries of the binarised SC and FC matrices, this describes the relative number of shared pairwise links between the two networks, providing a natural measure of structure–function similarity, ranging from zero for matrices with no common links to unity for identical matrices. The code for this computation is shown in Appendix A.

4.4 Weakly-coupled oscillator theory

In section 3.4 we showed that for networks with a row-sum constraint (as we have imposed on the SC matrix in this chapter), there is a globally synchronous steady state. Its linear stability, governed by the eigenvalues of the reduced model's Jacobian (3.19), is determined by the first derivative of phase interaction function. Therefore $\varepsilon I'(0) > 0$ can be considered a natural prerequisite for a structured network to support high levels of synchrony (without recourse to exploring the full Jacobian structure). Algorithm 1 outlines the procedure for calculating $I'(0)$ for the Jansen–Rit model. For completeness, however, the full Jacobian is also computed in order to account for the potential influence of detailed structure on the correspondence with the observed SC–FC agreement measured in simulations. To do this, the system given by (4.1) was integrated with $\varepsilon = 0.001$ to a (stable) phase-locked state, and relative phases computed. The eigenvalues of the Jacobian (eq. (3.19)) were then computed, with the largest non-zero real value providing an indication of solution attractivity. Note that although we do not characterise all possible phase-locked solutions (of which there may be too many for feasible numerical computation), we use this measure of stability of a single network state to serve as a comparison to the more readily solvable single-node analytical measures with which we mostly concern ourselves in this chapter.

It has been shown in Tewarie *et al.* (2018) that the eigenmodes of the structural connectivity matrix are predictive of emergent FC networks arising from an instability of a steady state. The largest non-zero eigenvalue, which is related to the most unstable eigenmode (or closest to instability), was found to be a good predictor of FC resulting from neural-mass time-series by computing the tensor product of its corresponding eigenvector, $v \otimes v$. Here we take this further by considering instabilities of the *synchronous* state. In this case the Jacobian (3.19) reduces to $-\varepsilon I'(0)\mathcal{L}_{ij}$ and the phase-locked state that emerges beyond instability of the synchronous state has a pattern determined by a linear combination of eigenmodes of the graph Laplacian, since all eigenmodes destabilise simultaneously. It is known that the graph Laplacian can be used to predict phase-locked patterns (Chen *et al.*, 2012) and has indeed been used to predict empirical FC from SC (Abdelnour *et al.*, 2018). Following from this, the eigenmodes of the Jacobian in (3.19) can be used as simple, easily computable proxy for the FC matrix when the system is poised at a local instability.

Algorithm 1 Algorithm to find $I(0)$ as defined in equation (3.18)

procedure PHASEINTERACTIONFUNCTION(*params*)
$\triangleright$ Where *params* contains the Jansen-Rit parameters.

  $\mathrm{d}t = 0.01$ $\triangleright$ Set time-step

  $\mathbf{y}_i = \mathbf{rand}(6)$ $\triangleright$ Set random initial conditions for variables

  $[T, \mathbf{Y}] = \mathbf{orbit}(params, \mathbf{y}_i, \mathrm{d}t)$ $\triangleright$ Solve to find orbit $\mathbf{Y}$ with period T.

  if $T = 0$ **then** $\triangleright$ Test for existence of orbit.

    return

  end if

  $total = 20T$ $\triangleright$ Set total time for computing adjoint (equation (3.17)).

  $\mathbf{Q}_i = \mathbf{rand}(6)$ $\triangleright$ Random initial conditions for phase response function.

  for $total \to 0$ **do** $\triangleright$ Solve adjoint in backwards time.

    solve $\dot{\mathbf{Q}} = \mathbf{Adjoint}(params, \mathbf{y}, \mathbf{Q}_i, T)$

  end for

  $\mathbf{Q}(\mathbf{t}) = \mathbf{flip}(\mathbf{Q}(\mathrm{end} - T : end))$ $\triangleright$ Isolate one period of (forward) time.

  $\triangleright$ Compute $\dot{\mathbf{Y}}$, given by system (4.1) evaluated at $\mathbf{Y}$.

  $inner = \langle \mathbf{Q}, \dot{\mathbf{Y}} \rangle \mathrm{d}t/T$ $\triangleright$ Computing time-averaged inner product.

  $\mathbf{Q} = \mathbf{Q}/inner$ $\triangleright$ Normalising phase response function.

  $\mathbf{H} = \mathrm{zeros}(\mathrm{size}(\mathbf{Q}))$, $H_5 = f(y_1(t) - y_2(t))$ $\triangleright$ Define interaction.

  $I(0) = \langle \mathbf{Q}, \mathbf{H} \rangle \mathrm{d}t/T$ $\triangleright$ Calculate interaction function.

end procedure

4.5 Results

4.5.1 Structure-function similarity

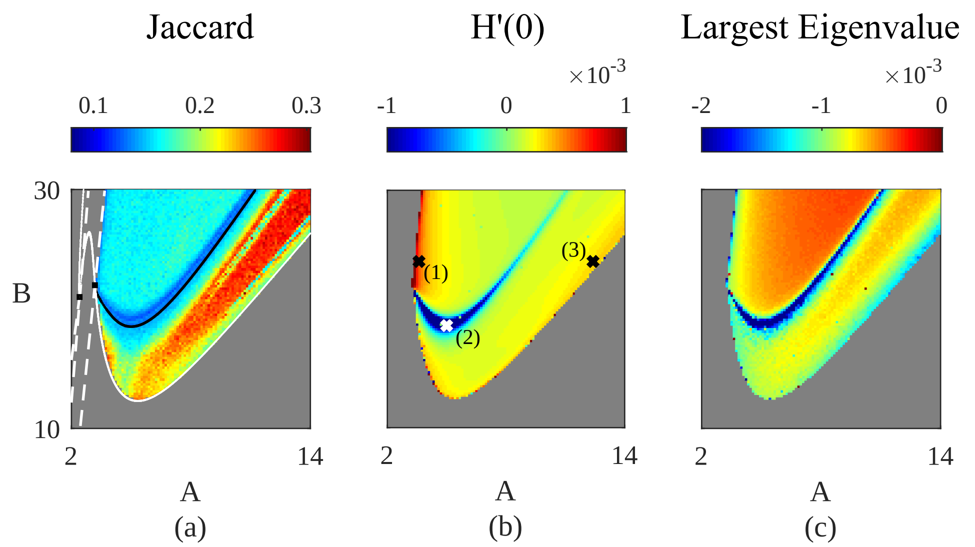

Figure 4.5: Structure–function analysis results. (a) Jaccard similarity coefficient between SC and FC (measured by MPC in (4.5), averaged over the entire 460 second timeseries) when the Jansen–Rit network (4.1) supports an oscillatory solution, averaged over 30 realisations of initial conditions chosen at random. Parameter values are given in Table 4.1. Warmer colours indicate greater SC/FC correlation. Here we have superimposed the bifurcation diagram for the network steady state, which shows the oscillatory region being bounded by Hopf/saddle-node sets in solid/dashed white lines respectively; boxes are Bogdanov–Takens points. False bifurcations in the single node case are indicated by a black line but, because of its relative size, the bistable region is not shown (though can be seen for the single node case in Figure 4.3). (b) The value of $I'(0)$ (see (3.16) and (3.19)) in the A, B-plane. When this value is positive/negative, the globally synchronised solution is stable/unstable (if it exists). Crosses mark parameters where we inspect the time-series in Figure 4.10. (c) The largest non-zero eigenvalue of the Jacobian for the full weakly-coupled oscillator network (equation (3.19)), calculated at a stable phase-locked state. More negative values indicate a stronger stability.

Figure 4.5 shows plots in the (A, B) parameter space highlighting our studies on the combined influence of SC and node dynamics on FC. In all panels, we report values in the region bounded by the bifurcation curves, obtained via a linear instability analysis of the network steady state, where the network model supports oscillations as well as phase-locked states. In Figure 4.5(a) the Jaccard similarity between SC and FC is computed from direct numerical simulations of the Jansen–Rit network model (4.1). Beyond the onset of oscillatory instability (supercritical Hopf bifurcation) the emergent phase-locked network states show a nontrivial correlation with the SC. This varies in a rich way as one traverses the (A, B) parameter space, showing that the precise form of the node dynamics can have a substantial influence on the network state. The highest correlation between SC and FC appears just beyond a Hopf bifurcation of a network equilibrium (shown as a solid white line), whilst a band of much lower correlation coincides with the fold bifurcations of limit cycles and false bifurcations of a single node (in black), reproduced from Figure 4.3. Indeed, it would appear that these mathematical constructs are natural for organising the behaviour seen in our *in silico* experiments. We reiterate that we have confirmed that the organising SC–FC features that we here identify are not crucially dependent on the binarisation, thresholding and normalisation procedure, described in section 4.1 and are qualitatively similar under variation of coupling strength (see section 4.5.3).

In Figure 4.5(b) we show a plot of $I'(0)$. Recall from our discussion of weakly-coupled oscillator theory in section 3.4 that a globally synchronous state (which is guaranteed to exist from the row-sum constraint) is stable if $\varepsilon I'(0) > 0$. Comparison with (a), highlights that when synchrony is unstable ($\varepsilon I'(0) < 0$), SC only weakly drives FC and we observe a low Jaccard similarity relative to that in the rest of the explored parameter space. Moreover, this instability region coincides with the region of bistability and the false bifurcation, stressing the important role of these bifurcations for understanding SC–FC correlation. Where $\varepsilon I'(0) > 0$, we observe higher Jaccard similarity when $I'(0)$ appears closer to 0, suggesting that operating close to criticality of synchrony facilitates greater SC–FC correlation.

Of course, there is a much finer structure in Figure 4.5(a) that is not predicted by considering either the bifurcation from steady state, or the weakly-coupled analysis of synchronous states, and so it is illuminating to pursue the full weakly coupled oscillator analysis for structured networks. The eigenvalues of the Jacobian, corresponding to more general stable phase-locked states, can be used to give a measure of solution attractivity. The largest eigenvalue is plotted in Figure 4.5(c). The most stable (non-synchronous) phase-locked states occur in the neighbourhood of the false bifurcations, as well as in the region of bistability and along the existence border for oscillations, defined by a saddle node bifurcation. Furthermore, stronger stability of the general phase-locked states corresponds with stronger stability of global synchrony (in Figure 4.5(b)), apart from near false bifurcations, which again highlights their importance in organising the observed SC–FC correlations. In correspondence with Figure 4.5(b), we find that when the phase-locked solution is closer to criticality, in accordance with the largest eigenvalue being closer to 0, we observe higher Jaccard SC–FC similarity in Figure 4.5(a), which again emphasises the role of critical dynamics in influencing patterns of FC.

4.5.2 Phase-locking and synchrony

To test the predictive power of the weakly-coupled theory, we compare the emergent FC structure obtained from direct simulations of the Jansen–Rit network model (4.1) against direct simulations of the weakly-coupled oscillator network (3.16). In this case, MPC (4.5) is not ideally suited for our study because it does not discern between phase-locking and complete synchrony, yet we consider situations where stable phase-locking naturally arises. Therefore, FC in the weakly-coupled network is computed via the new metric of mean phase agreement (MPA), whereby patterns of coherence are determined by a temporal average of relative phase differences:

$$\hat{R}_{jk} = \frac{1}{M}\sum_{l=1}^{M}\frac{1}{2}\big(1+\cos(\Delta\phi_{jk}(t_l))\big). \tag{4.7}$$

In Figure 4.6, the phases required to compute (4.7) from simulations of (4.1) are determined from each node's time-series by a Hilbert transform; in the weakly-coupled oscillator case, the phase variables from equation (3.16) are employed directly. Since the weakly-coupled reduction of the Jansen–Rit model is deterministic, these simulations were computed in the absence of noise ($\mathrm{d}W_i = 0$ for all nodes), using Matlab's built-in ode45 adaptive timestepper (the model equations were integrated for a total time of 1000 seconds). As expected, we find excellent agreement between the modular FC structure in the case of very weak coupling, with this agreement reducing with increasing ε, as quantified by a reduction in Jaccard similarity (from 0.98 in panel (a) to 0.65 in (c)). This is a manifestation of the network moving from a dynamical regime that can be well described by the weakly-coupled reduction (3.16) to one where stronger network interactions dominate. Since an analogous theory does not exist for stronger coupling, we do not consider here how SC–FC relations arise from network dynamics within a strongly–coupled framework.

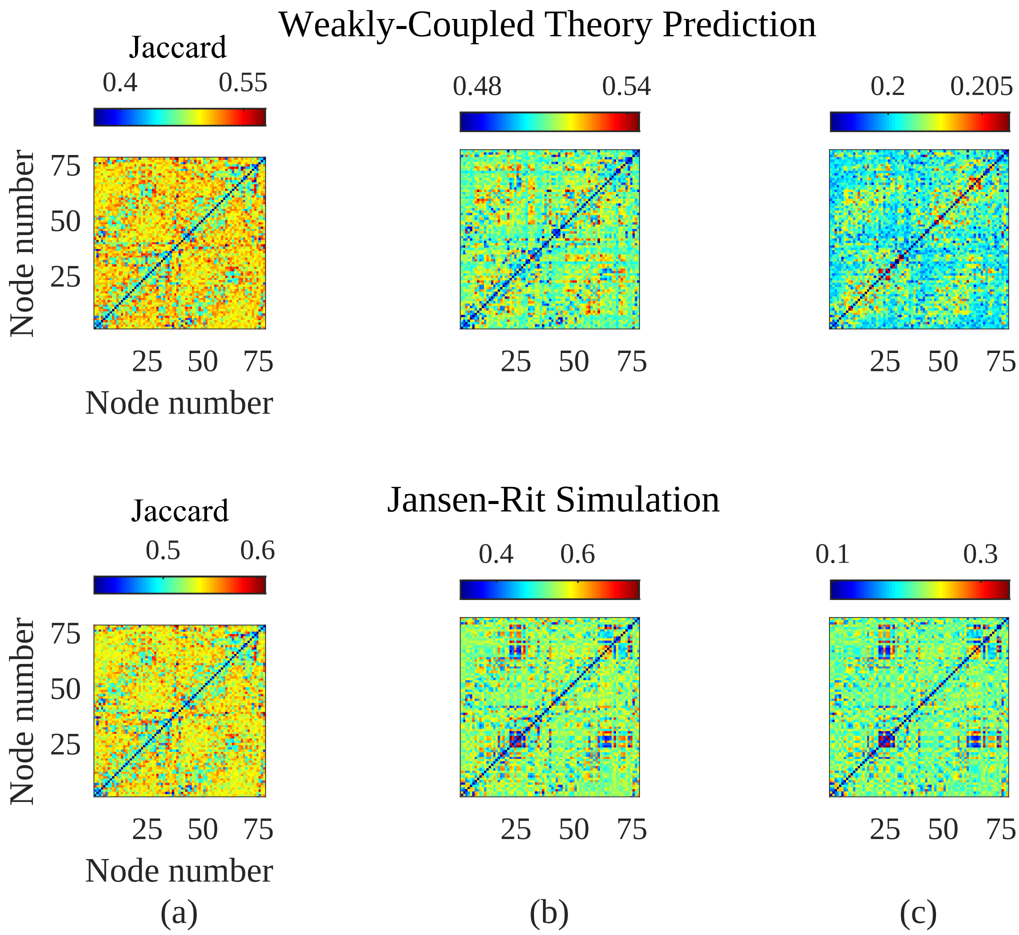

Figure 4.6: Comparison of FC patterns from averages of realisations of the weakly-coupled oscillator model (3.16) with corresponding Jansen–Rit (4.1) simulations, with no noise present, at $A = 5, B = 19$, computing averages over 600 realisations with initial conditions chosen at random (other parameter values are given in Table 4.1). (a) ε=0.01; (b) ε=0.1; (c) ε=1. These results show how the weakly-coupled theory becomes less predictive for stronger coupling strengths, resulting in matrices with Jaccard similarity of 0.98, 0.76 and 0.65 (to 2 s.f.) respectively.

Through the instability theory of the synchronous state we can construct a proxy for the FC as described in section 4.4. In Figure 4.7 we compare simulated FC with that predicted by $R^\star$ using the tensor product sum,

$$R^\star = \sum_{i=1}^{N^*} \lambda_i v_i \otimes v_i \tag{4.8}$$

of $v_k = (v_k^1, \ldots, v_k^N)$, which denotes the k^{th} eigenvector of the Jacobian for the synchronous state. These are weighted by their corresponding eigenvalues, λ_k, and we include the N^* unstable eigenmodes (*i.e.* using the unstable eigenmodes of the Jacobian at synchrony), for parameter values that lie just beyond the onset of instability of the globally synchronous state and near the false bifurcation set (see Figure 4.5(a,b)). We observe that the key features of the FC are captured by the eigenmode prediction; indeed the (weighted) Jaccard similarity coefficient between predicted and simulated FC (both scaled to $[0, 1]$) is calculated to be 0.82. We believe this to be a reasonable prediction considering the high dimensionality and non-linearity of the model, though a smaller network with dynamics operating closer to its linear approximation would likely be better predicted by this method. This offers a convenient way of predicting an emergent FC pattern, since it does not rely on brute-force forward integrations of the full network model, which may take a long time to converge. However, it does require, knowing the phase-locking solution to the weakly-coupled oscillator model, though this is generally of a much lower dimension since it consists of only one ODE for each oscillator.

4.5.3 Impact of SC post-processing on results

As described in secction 4.1, we process structural connectivity data obtained from the HCP by thresholding, binarising and normalising by row. To confirm that these procedures do not unduly influence our conclusions, or restrict their applicability, we performed the following tests. First, we check that the results in Figure 4.5 hold under different levels of threshold. Then,

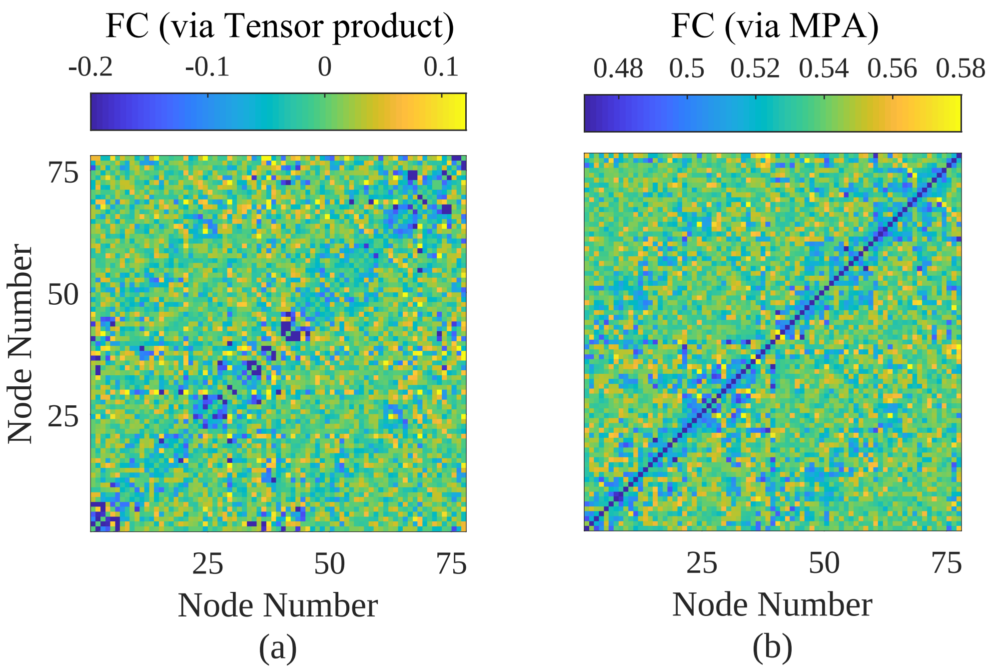

Figure 4.7: (a) FC prediction given by the a linear combination of eigenmodes of the weakly-coupled oscillator system, given by tensor products of eigenvectors of the SC graph Laplacian (4.8), with $N^* = N$. (b) Direct simulation of the Jansen–Rit network model (4.1) with no noise present. Parameter values are chosen as $A = 6$, $B = 18$, which lies near the existence border for stable synchronous solutions (see Figure 4.5(b)); other parameter values are given in Table 4.1. The (weighted) Jaccard similarity between the two FC networks (scaled to $[0, 1]$ for comparability) is calculated to be 0.82, indicating the predictive power of equation (4.8).

we confirm that we observe similar results for the unbinarised network.

Statistical checks on the distribution of unthresholded SC weights indicate that node degree distributions have standard deviation of less than 10% of the mean, and outliers differ from the mean by less than 25%. Therefore we are confident that our thresholding and binarisation process does not unduly influence the SC network structure, and thereby our results. We have also confirmed that the features of SC–FC correlation that we uncover in Figure 4.5(a) are retained for different thresholds (namely: 20%, 30%, 40%, see Figure 4.8).

To ensure that binarisation of the SC matrix did not crucially influence our findings, we recalculate equivalents of Figures 4.5(a) and (c) for a weighted, un-normalised network, obtaining similar SC–FC structures (see Figure 4.9). Inspection of node behaviour in the weighted un-normalised network, at parameter choices for which Figure 4.5(b) predicts stable or unstable synchronous behaviour, shows that the predictive power of our linear analysis is retained in the un-normalised case (see Figure 4.10).

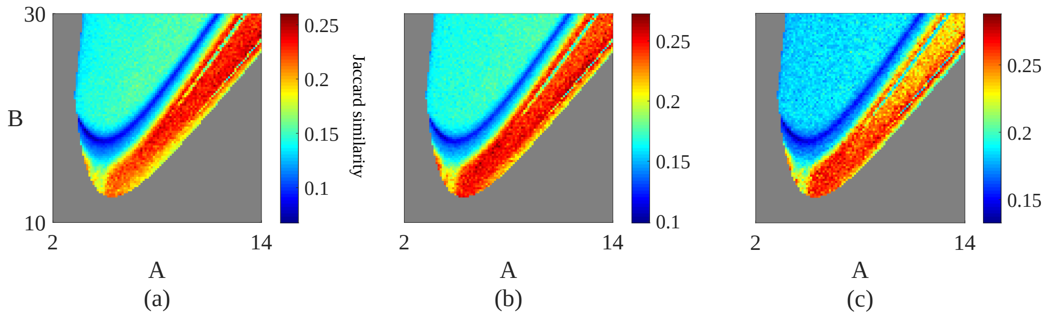

Figure 4.8: Jaccard similarity coefficient at different thresholds. Computed in exactly the same fashion as in Figure 4.5(a), except in each case the structural matrix was thresholded to (a) 20%, (b) 30% and (c) 40% of its strongest connections, which were then binarised and normalised by row sum.

As noted in Hansen *et al.* (2015), variation in coupling strength can affect SC–FC relations. In Figure 4.11, we show that the essential organising features of the Jaccard similarity between SC and FC that we highlight in Figure 4.5(a) are qualitatively unchanged for a range of choices of coupling strength ε.

These tests indicate that the steps taken to post-process the SC data, in the interests of analytical tractability, do not unduly negate the significance of the computational results. Specifically, in all network cases, we find that the relatively low SC–FC agreement is observed when parameters are close to the false bifurcation set.

4.6 Discussion

In this chapter, we investigated the degree to which the dynamical state of neural populations, as well as their structural connectivity, facilitates the emergence of functional connections in a neural-mass network model of the human brain. We have addressed this by using a mixture of computational and mathematical techniques to assess the correlation between structural and functional connectivity as one traverses the parameter space controlling the inhibitory and excitatory dynamics and bifurcations of an isolated Jansen–Rit

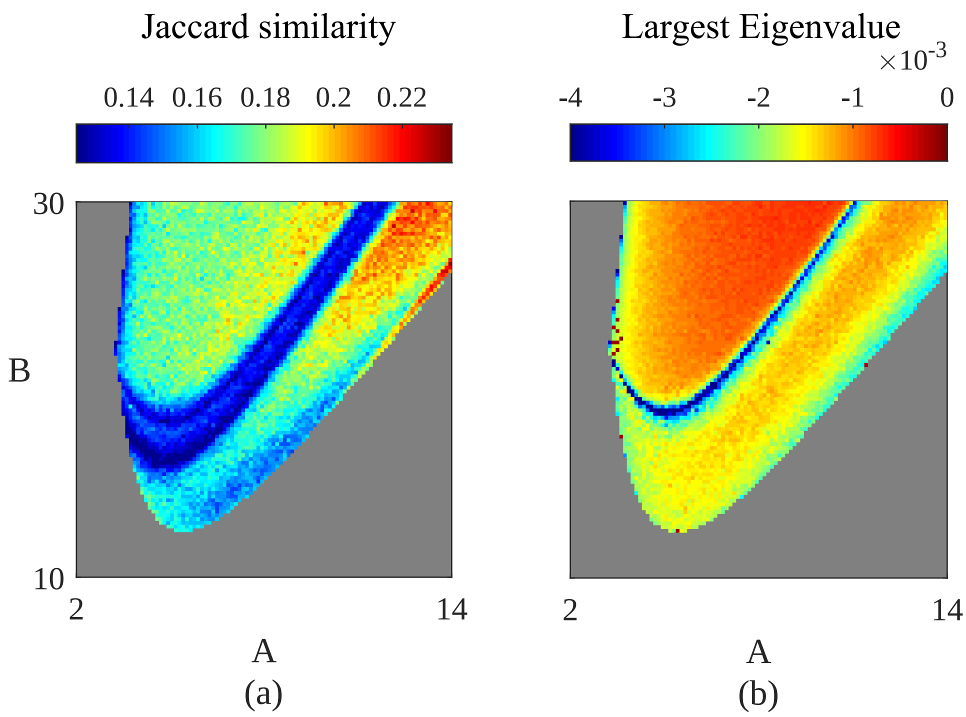

Figure 4.9: Results for un-normalised network. (a) Jaccard similarity coefficient between SC and FC in numerical simulations of the Jansen–Rit network model (4.1), when the network supports an oscillatory solution. Here the structural connectivity is the original weighted, un-normalised data. Model parameters are as in Figure 4.5. (b) The largest non-zero eigenvalue of the Jacobian for the full weakly-coupled oscillator network (3.16), calculated at a stable phase-locked state for the un-normalised SC matrix.

neural mass model. Importantly, SC has been estimated from HCP diffusion MRI datasets. We did not record high levels of similarity (which ranged from ~ 0.1 to ~ 0.3 in Figure 4.5(a)), which reflects the fact that the model supports FC states that differ highly from the SC. Moreover, the focus here was to investigate the degree to which emergent SC–FC similarity could be predicted from the underlying node dynamics operating within the wider network, by comparing the pattern of Jaccard similarity in relation to different analytical measures (*i.e.* bifurcation sets and stability of phase-locking) within the explored parameter space. We find that SC strongly drives FC when the system is close to a Hopf bifurcation, whereas in the neighbourhood of a false bifurcation, this drive is diminished. These results emphasise the vital role that local dynamics has to play in determining FC in a network with a static SC. In addition, we show that a weakly-coupled analysis provides insight into the

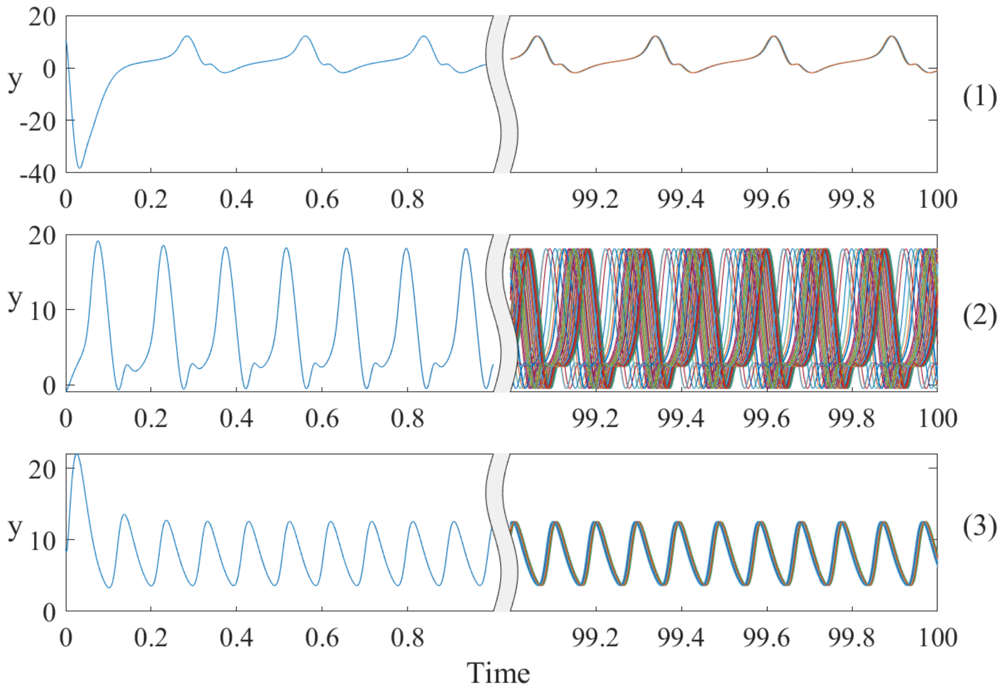

Figure 4.10: Correspondence of synchrony stability in normalised versus un-normalised network. time-series plots for the node activity in the unnormalised structural network for parameters $A = 3.6$, $B = 24$ (1), $A = 5$, $B = 18.6$ (2), $A = 12.4$, $B = 24$ (3), which correspond to different levels of stability of synchrony as labelled in Figure 4.5(b). In these simulations, $\varepsilon = 0.01$.

organisation of SC–FC correlation features across parameter space, and can be exploited to predict emergent FC structure.

We note that modelling SC–FC relations is a well-studied field and we outline some related studies which have reported relevant results to contextualise our findings. Messé *et al.* (2014) considered statistical models to predict FC from SC (in particular, a spatial simultaneous autoregressive model (sSAR), whose parameters can be estimated in a Bayesian framework) and found, interestingly, that simpler linear models were able to fare at least as well. More recently, Saggio *et al.* (2016) were also able to make predictions of FC from empirical SC data (and *vice versa*) using a simple linear model. Since the only free parameter of their model for SC is the global coupling strength, results from this method are efficient and computationally inexpensive. We have not attempted to reproduce empirical data here, but we have shown that similar predictions can be made using bifurcation theory and network reduc-

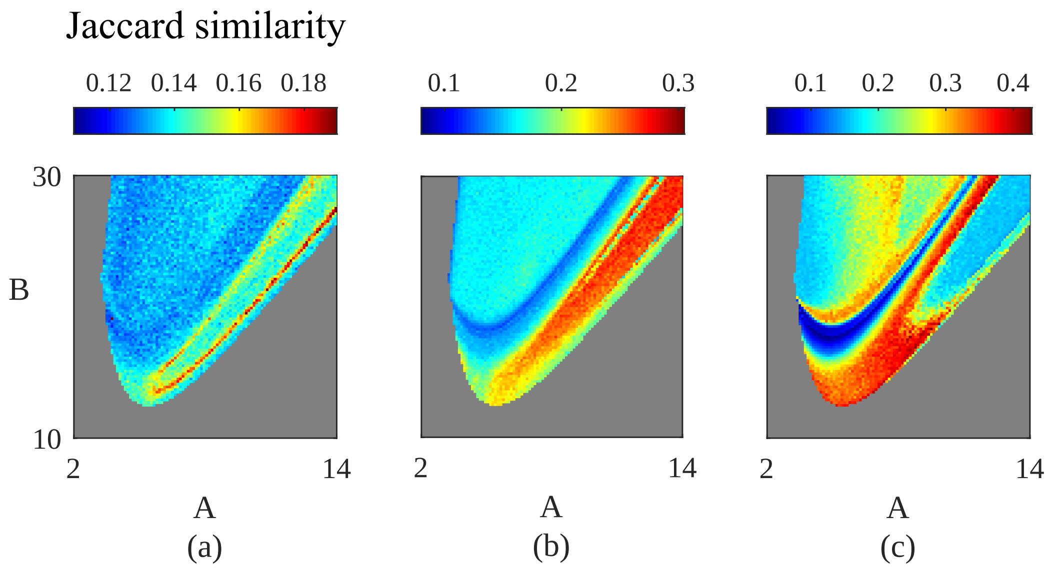

Figure 4.11: Jaccard similarity coefficient at different coupling strengths. These were computed in exactly the same fashion as in Figure 4.5(a), except in each case ε was set to (a) 0.01, (b) 0.1, (c) 1.0.

tion techniques; such an approach allows us to consider in more detail, and explain, the influence of the rich neural dynamics supported by the Jansen–Rit model on SC–FC relationships. Nevertheless, it is important to note that the FC structures we are concerned with are averaged over long-time scales and therefore represent a static FC state, as opposed to dynamic FC. Use of such static FC networks as a clinical biomarker is widespread; however, subject variability in FC means that their predictive power is restricted to group analyses (Mueller *et al.*, 2013). To capture the rich dynamic FC repertoire exhibited in empirical resting state data, for example the distinct hierarchical organisation in switching between FC states (Vidaurre *et al.*, 2017), will require alternative approaches. One such approach is dynamic causal modelling, as employed in Goulden *et al.* (2014) and Van de Steen *et al.* (2019) for empirical data.

The modelling work presented here is relevant in a wider neuroimaging context—for example, epilepsy is often considered to be caused by irregularities in synchronisation (Mormann *et al.*, 2003; Netoff and Schiff, 2002; Lehnertz *et al.*, 2009). It is noteworthy that the changes in synchrony patterns that we observe can be largely attributed to local dynamical considerations, without the need to concern ourselves with large scale structural topology. In the Jansen–Rit model, the bifurcations organising emergent FC take the form of Hopf, saddle, fold of limit cycle and false bifurcations. False bifurcations have received relatively little attention in the dynamical systems community (a notable exception being the work of Marten *et al.* (2009)), although our results indicate that they may be significant for understanding how 'synchronisability' of brain networks is reduced during seizures. This phenomena was reported in Schindler *et al.* (2008), which also found that synchronisability increases as the patient recovers from seizure state.

A natural extension to the work presented here would be the inclusion of conduction delays, characterised by Euclidean or path-length distances between brain regions, which are certainly important in modulating the spatiotemperal coherence in the brain (Deco *et al.*, 2009). These would manifest as constant phase shifts in the weakly-coupled reduction of the model (Ton *et al.*, 2014). For strongly coupled systems the mathematical treatment of networks with delayed interactions remains an open challenge. Recent work in this vein by Tewarie *et al.* (2019) focuses on the role of delays in destabilising network steady states, and techniques extending the Master Stability Function to delayed systems (Otto *et al.*, 2018) may be appropriate for treating phase-locked network states. Though we do not pursue a direct extension to the study presented in this chapter (which would ideally contain analogues of all results with the inclusion of delay parameters), in chapter 7, we revisit this issue to investigate delays in the context of neuromodulation, in particular how delays arising from the topology of brain networks excite different FC patterns.

In summary, the findings reported here suggest that there are multiple factors which give rise to emergent FC. While structure clearly facilitates functional connectivity, the degree to which it influences emergent FC states is determined by the dynamics of its neural sub-units. Importantly, we have shown that local dynamics has a clear influence on SC–FC correlation, as does network topology and coupling strength. Our combined mathematical and computational study has demonstrated that a full description of the mechanisms that dictate the formation of FC from anatomy requires knowledge of how both neuronal activity and connectivity are modulated and, moreover, exposes the utility of bifurcation theory and network reduction techniques. These together add to the wider study of SC–FC relations and their relevance to the critical brain hypothesis (discussed in section 2.1.2). Moreover,our results demonstrate that this analysis may largely be conducted on the local level of single-node dynamics, rather than the wider network, as an expedient way to study properties of the emergent FC. This work is further extended to a more complex neural mass model derived by Coombes and Byrne (2019) in chapter 6, to explore the relationship between dynamics and structure–function relations in externally stimulated neural networks, with particular focus on applications to TMS. In the next chapter, we will again consider SC–FC relations in a study less driven by understanding of the dynamical properties of networks, but more focussed on the topology of networks. In particular, we investigate whether the topological changes induced by thresholding and binarising SC has a significant impact of SC–FC relations in an extension of a multiplex network measure defined by Crofts *et al.* (2016).

Chapter 5

A weighted clustering measure for multiplex brain networks

In this chapter, we deploy techniques from network science to further interrogate structure–function relations in the brain. In chapter 4, we largely focused on the impact that nodal dynamics has on structure–function relations. The Jaccard index proved a useful metric by which we could characterise the structure–function relationship in the light of our mathematical results, allowing us to perform an in-depth study of how the observed computational results arose. However, as discussed in chapter 3, there are many network measures we could use and it is of interest, in the context of neuroimaging, to develop novel metrics to answer particular questions of connectivity data, be they theoretical or empirical. Currently, there is growing interest in the use of multiplex measures, where the edges within each layer represent different types of interaction between the same set of nodes, to better understand the relationships between brain networks.

Here we build upon the previous work of Crofts *et al.* (2016), in which a multiplex clustering measure to treat binary SC and FC matrices is presented to investigate the emergence of functional connections that are distinct from the underlying cortical structure. Their study follows a similar computational setup to the previous chapter, whereby the SC matrix used in forward simulations of neural activity is thresholded, binarised and normalised by row. While binarisation is useful to isolate strong connections to better expose the modules and clusters in brain networks (Sporns, 2013), it comes at the cost of losing information about relative connection strengths from which network metrics may give a better characterisation of the network topology (Dimitriadis *et al.*, 2017). Preserving mean node degree, for example, has been found to be critical in simulating seizure states in a network model incorporating epilepsy patients' connectivity data (Petkov *et al.*, 2014).

The aim of the work in this chapter is to establish a measure more widely applicable to both simulated and empirical structure–function connectivity data, therefore being more useful to the neuroscience community. In this extension to Crofts *et al.* (2016), we generalise the metric presented therein to treats weighted networks with any number of network layers. We evaluate the impact of using this measure by conducting a companion computational study to Crofts *et al.* (2016), to highlight qualitative differences in the results. We go on to demonstrate the measure's usefulness by calculating the multiplex clustering of a 6 layer multiplex (formed of a SC layer and 5 frequency band-filtered FC layers).

5.1 Multiplex description

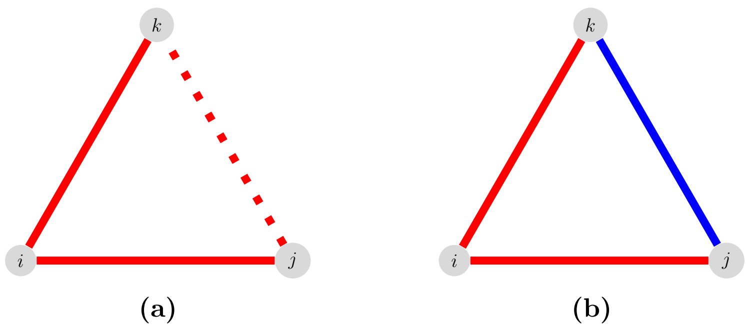

Figure 5.1: Multiplex triads. (a) We consider a triad as being formed of a node i with connections to two other nodes, j and k in the same (red) layer, which are not necessarily connected to each other in that layer. (b) A multiplex triad, which is closed by a connection between j and k present in a second (blue) layer.

A multiplex is a collection of several networks that overlap to comprise the different types of connections that exist between nodes within the network. This is a special case of the more general multilayer network, which also considers connections between layers (Kivelä *et al.*, 2014).

We consider a graph $G(V, E^{[1]}, \ldots, E^{[M]})$, where V is a set of vertices and E^{α} is a set of edges appearing in layer α of M network layers. V is the same for all network layers.

Each layer can now represent a different type of connection. In brain networks, the connectivity could constitute FC derived from correlated activity in different brain rhythm frequency bands (Buldú and Porter, 2018; Tewarie *et al.*, 2016; Yu *et al.*, 2017b), temporally varying networks measured across different epochs (Mucha *et al.*, 2010; Sannino *et al.*, 2017), or structure–function network layers (Battiston *et al.*, 2017; Crofts *et al.*, 2016).

It is convenient to use the methodology of Battiston *et al.* (2014), whereby standard nodal clustering, c_i, represented by equation (3.1) is transformed its multiplex analogue,

$$c_i^{\text{multiplex}} = \frac{\sum_{\alpha}\sum_{\alpha' \neq \alpha}\sum_{j \neq i}\sum_{k \neq i} a_{ij}^{[\alpha]} a_{jk}^{[\alpha']} a_{ki}^{[\alpha]}}{(M-1)\sum_{\alpha}\sum_{j \neq i}\sum_{k \neq i} a_{ij}^{[\alpha]} a_{ki}^{[\alpha]}}, \tag{5.1}$$

where $a_{ij}^{[m]}$ represents a connection from node $j \to i$ in the mth layer. We extend the definitions of open and closed triads introduced in 3.1.1 to multiplex counterparts, composed of edges in different layers. Equation (5.1) is suitable for treating multiple network layers simultaneously, with triadic structures in the form of Figure 5.1, but for now we focus on the simplest two-layer case for the purpose of structure–function analysis.

The novelty of the metric presented in Crofts *et al.* (2016) was to restrict this clustering measure to only consider node triplets in the structural layer S which do not form a closed triad (*i.e.* the edge weight between j and k in Figure 5.1 is enforced to be 0) and asks what proportion of these open triads are closed by an edge in the functional layer F. For a symmetric matrix, this can be written as:

$$
\begin{aligned}
c_i^{SF} &= \frac{\sum_{j\neq i}\sum_{k\neq i} a_{ij}^{[S]} a_{jk}^{[F]} a_{ki}^{[S]} (1-a_{jk}^{[S]})}{\sum_{j\neq i}\sum_{k\neq i} a_{ij}^{[S]} a_{ki}^{[S]} (1-a_{jk}^{[S]})} \\
&= \frac{(A^{[S]}(A^{[F]}\cdot(E-A^{[S]}))A^{[S]})_{ii}}{(A^{[S]}(E-I)A^{[S]}-A^{[S]^3})_{ii}},
\end{aligned}
\tag{5.2}
$$

where I is the identity matrix, E is a matrix of ones and the bullet operator $(\cdot)$ represents element-wise scalar multiplication of matrices.

It is important to note here that this new measure is a departure from the network analysis posed in the previous chapter. While the aim there, using the Jaccard index, was to determine the degree to which FC was inherited from SC, the aim here is to understand where strong functional connections emerge in presence of a weak structural counterparts. Specifically, the new measure quantifies the degree to which the addition the functional layer improves the transitivity of the network relative to the single layer SC. This serves as a tool to continue to our research into structure–function relations from the previous chapter, since much of the variability in FC arises from strong functional connections between anatomically unconnected regions (Honey *et al.*, 2009).

5.2 Methodology

While (5.2) is a useful tool to study emergent SC–FC relations, it was only employed in Crofts *et al.* (2016) for binary data with 2 layers. Here, we generalise this measure to consider an arbitrary multiplex of weighted layers. We also describe how we test that the inclusion of weighted data gives qualitatively different results using multiplexes formed of a connectomic structural layer and FC layers derived from time series of a computational model. Finally, we report how we obtain preliminary results using FC data obtained from MEG time series to highlight the usefulness of the metric and the scope for further study.

5.2.1 Weighted clustering coefficients

Before we proceed with discussing the specific multiplex measures, it is important to note that there are several ways to define weighted clustering measures. In binary networks, we can describe the (single-layer) clustering coefficient for a node i as,

$$\frac{\text{Number of closed triads centred on node } i}{\text{Number of triads (open or closed) centred on node } i}. \tag{5.3}$$

In this case, the metric only concerns the existence of closed/open triads, whereas in the weighted case each must have some value attributed to it. This is discussed in depth in Opsahl and Panzarasa (2009), where several candidates for the triadic values are analysed, chiefly the arithmetic and geometric mean of weights as well as the maximum and minimum weights. However, the choice of triad value is largely dependent on the type of network being studied and the particular relationship between interacting nodes that is to be exposed by the measure.

In this chapter, we use the product of weights as triad values, which are equivalent to those employed in equation (5.1) when weights are binary. This ensures that the extension of (5.1) to weighted networks quantifies an analogous multiplex property.

5.2.2 Generalised multiplex clustering for M weighted layers

Following on from the definition of triad values, we note that if we have a set of undirected network layers, with edge weights described by matrices $W^{[m]}$ for each layer m, we can substitute these connectivity weights for binary strengths in the clustering coefficient (5.1). In this case, the metric gives the proportionality between the sum of closed multiplex triad products ($w_{ij}^{[\alpha]} w_{jm}^{[\alpha']} w_{mi}^{[\alpha]}$) and all $\alpha - layer$ triad products ($w_{ij}^{[\alpha]} w_{mi}^{[\alpha]}$).

As in equation (5.2), we wish to manipulate the clustering coefficient to give a notion of how much the secondary layers (α'; appearing blue in figure Figure 5.1) contribute to the transitivity of the multiplex relative to the underlying (α; appearing red in figure Figure 5.1) layers. In (5.2), this is achieved by only considering open triads that are not completed by a structural edge, $\sum_{j \neq i} \sum_{k \neq i} a_{ij}^{[S]} a_{ki}^{[S]} (1 - a_{jk}^{[S]})$. Assuming weights lie on $[0, 1]$, we can similarly consider weighted products of triads centred on node i to be inversely proportional to connections between neighbours of i by multiplying by a factor $1 - w_{jk}^{[S]}$. This ensures that the new metric is equivalent to (5.2) for binary structure and function. The full generalised clustering coefficient is therefore

$$\begin{aligned} \tilde{c}_i &= \frac{\sum_{F_n} \sum_{j \neq i} \sum_{k \neq i} w_{ij}^{[S]} w_{jk}^{[F_n]} w_{ki}^{[S]} (1 - w_{jk}^{[S]})}{(M-1) \sum_{j \neq i} \sum_{k \neq i} w_{ij}^{[S]} w_{ki}^{[S]} (1 - w_{jk}^{[S]})} \\ &= \frac{\sum_{F_n} (W^{[S]} (W^{[Fn]} \cdot (E - W^{[S]})) W^{[S]})_{ii}}{(W^{[S]} (E - I) W^{[S]} - W^{[S]^3})_{ii}}, \end{aligned} \tag{5.4}$$

for M undirected network layers, where the first layer denotes brain SC and the layers $F_n, n = 1, \ldots, M-1$ are different FC network layers. For our particular clustering definition we require the weights to lie on $[0, 1]$, so we normalise each layer m according to $\tilde{W}^{[m]} = (W^{[m]} - \min(W^{[m]}))/(\max(W^{[m]}) - \min(W^{[m]}))$. This scaling is applied to the rest of the networks we concern ourselves in this chapter.

In order to ascertain the degree to which the clustering coefficient arises from the specific topology of the multiplex, rather than solely the distribution of weight values itself, it is helpful to normalise the coefficient by the mean of corresponding results for random surrogate networks, $\tilde{c}/\langle \tilde{c}^{\text{rand}} \rangle$, for which node number, row/column sums and connection density are preserved. In the following we introduce the procedures for randomisation of networks, with schematics provided in Figure 5.2.

The algorithm employed here for randomising binary networks is presented in Maslov and Sneppen (2002), whereby two pairs of connected nodes, $B \to A$ and $D \to C$, are chosen such that no edges exist from $D \to A$ and

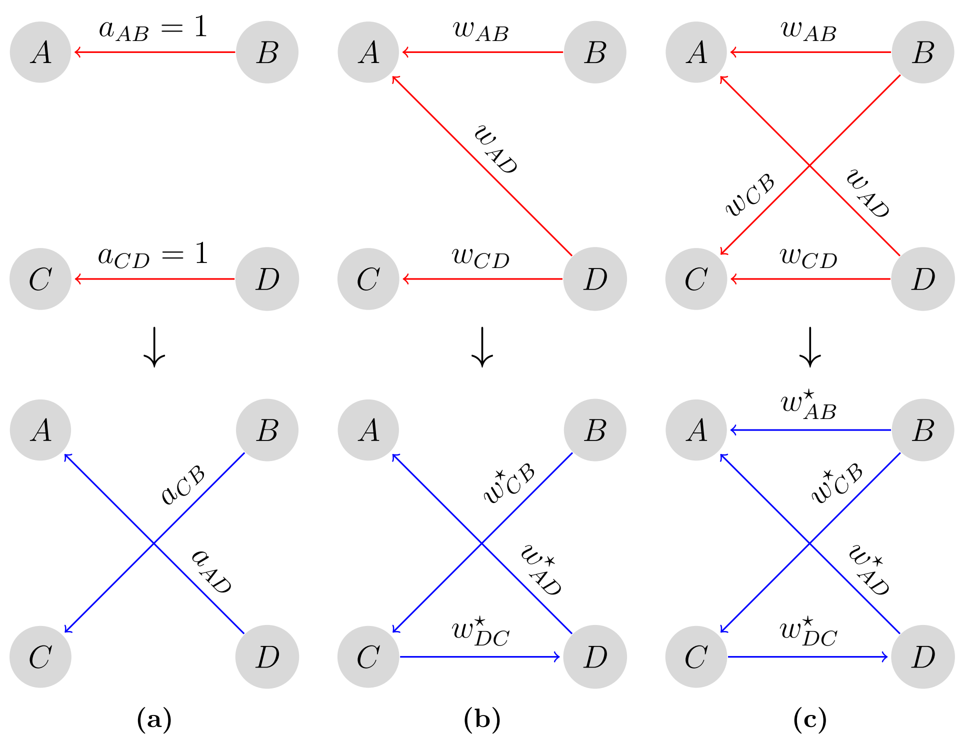

Figure 5.2: Randomisation algorithm schematics. An illustration of how connections and associated weights change at each iteration of the randomisation procedure for (a) binary thresholded, with $a_{ij} = 1$ if an edge exists from $j \to i$ and 0 if not; (b) weighted thresholded, where w_{ij} is the weight of the edge from $j \to i$ and $w^{\star}_{CD} = w_{CD} - w_{AB}$, $w^{\star}_{AD} = w_{AD} + w_{AB}$, $w^{\star}_{CB} = w_{AB}$; (c) weighted all-to-all networks, with $w^{\star}_{AB} = w_{AB} - X$, $w^{\star}_{CD} = w_{CD} - X$, $w^{\star}_{AD} = w_{AD} + X$, $w^{\star}_{CB} = w_{CB} + X$, $X \in [0, \min\{w_{AB}, 1 - w_{AD}, 1 - w_{CB}, w_{CD}\}]$.

$B \to C$. The connections within the chosen pairs are then removed and new connections are added to the pairs $D \to A$ and $B \to C$. We extend this to formulate our own comparable algorithms to treat weighted networks, which may be all-to-all (where every node pair has an associated edge) or thresholded (where only a subset of node pairs have edges between them). We note that similar randomisation algorithms are employed in Opsahl *et al.* (2008), though here we pursue algorithms more readily comparable to the method employed in Crofts *et al.* (2016) in the interests of continuity with that study. We note that since the original algorithm of Maslov and Sneppen (2002) was formalised for directed networks, the following algorithms are also described in terms of directed networks. It is simple to extend them to undirected networks, however, by repeating the procedure at each step with subscript indices reversed, i.e $w_{AB} \to w_{BA}$ etc.

For randomising thresholded weighted networks, we modify this algorithm slightly. We again choose two pairs of connected nodes, where $A \to B$ has the smaller of the two connection weights, but enforce the condition that an edge exists from $D \to A$, but not from $B \to C$. Furthermore, we require $w_{AB} < 1 - w_{AD}$, in order to keep all edge weights within $[0, 1]$. If this is satisfied, we assign new edge weights $w^\star_{AB} = 0$, $w^\star_{CD} = w_{CD} - w_{AB}$, $w^\star_{AD} = w_{AD} + w_{AB}$, $w^\star_{CB} = w_{AB}$. This ensures that in the 4-node subnetwork we have chosen, we have 3 edges pre- and post-randomisation to preserve connection density.

When randomising all-to-all weighted networks, we can alter the algorithm further. Again selecting four random nodes (we are now guaranteed that edges exist between all pairs), we can choose a value X selected (randomly) from a uniform distribution $[0, \min\{w_{AB}, 1 - w_{AD}, 1 - w_{CB}, w_{CD}\}]$ and again assign new node weights $w^\star_{AB} = w_{AB} - X$, $w^\star_{CD} = w_{CD} - X$, $w^\star_{AD} = w_{AD} + X$, $w^\star_{CB} = w_{CB} + X$.

In the following section, we pursue the extension of Crofts *et al.* (2016) to multiplexes with weighted structural and functional layers.

5.2.3 Structure–function clustering

As proof-of-principle for the new clustering measure, we employ a computational approach following the procedure presented in Crofts *et al.* (2016). Briefly, we simulate time series for a network of nodes whose dynamics are governed by a system of Wilson–Cowan network equations, described in chapter 1:

$$\begin{aligned} \dot{u}_i &= -u_i + s(c_1 u_i - c_2 v_i + P + \varepsilon \sum_j w^{[S]}_{ij} u_j) \\ \dot{v}_i &= -v_i + s(c_3 u_i - c_4 v_i + Q). \end{aligned} \tag{5.5}$$

Recall from section 2.2.1 that the c_n are parameters governing the coupling strength of within-node excitatory and inhibitory neural populations, which have respective population-average activities u_i and v_i and basal inputs P and Q; s is a sigmoidal function that represents the average firing rate of populations. Each node represents a brain region in the AAL atlas, with structural connectivity described by a weighted matrix with elements $w_{ij}^{[S]}$ (scaled by the parameter ε in the ODE system) describing the strength of connection between nodes i and j, informed using the same connectome data employed in the previous chapter (described in section 4.1).

In the same spirit as the computational study presented in the previous chapter, the system (5.5) is integrated using Matlab®'s built-in `ODE45` solver for 1000 seconds to produce time series solutions for each node. The Pearson correlation is computed for pairs of time series for the excitatory populations to produce a functional connectivity matrix with weights $W_{jk}^{[F]} = R_{jk}$.

For comparison with Crofts *et al.* (2016), we report a global measure of clustering using the mean value of (5.4), $\hat{c}_i = 1/N \sum_i^N \tilde{c}_i$, for a network of N nodes. We normalise each value by an average of corresponding results for 100 random surrogate networks. These surrogates are constructed by running corresponding simulations for a randomised SC, with preserved node degree and connection density, via 100,000 iterations of the algorithms described in section 5.2. This number of iterations was chosen because the Jaccard similarity between SC and random SC appeared to converge such that more iterations did not make the matrices significantly more dissimilar (Figure 5.3).

Results for these computations are outlined in section 5.3.1.

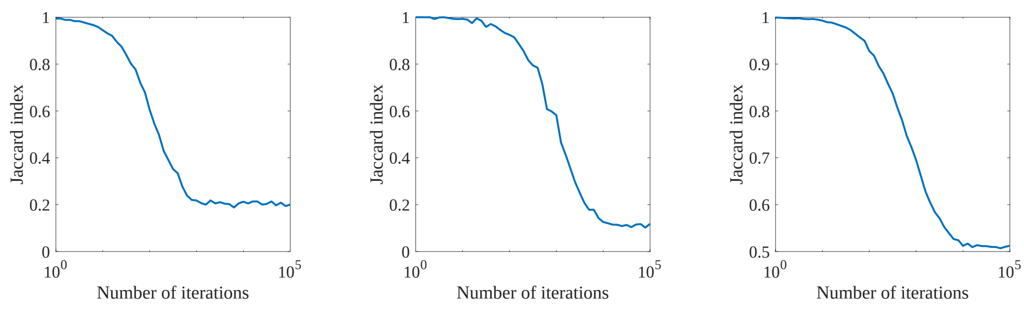

(a) (b) (c)

Figure 5.3: Convergence of Jaccard similarity between original and random networks. Jaccard similarity between the structural matrix and its randomised counterpart for different numbers of iterations of the algorithms for (a) binary, (b) weighted thresholded and (c) weighted all-to-all network, averaged from 10 realisations.

5.2.4 Frequency band-filtered FC

It is becoming increasingly clear that the brain operates across multiple frequency bands (Deco *et al.*, 2017a; Florin and Baillet, 2015; Furl *et al.*, 2014), with the activity of brain regions forming frequency-specific correlations with other brain regions. Multiplex approaches are therefore of great interest to the neuroimaging community to understand the complex functional connectivity arising from oscillatory activity within different bands in order to reveal a more complete picture of the brain's functional behaviour (Brookes *et al.*, 2016; Buldú and Porter, 2018).

We exploit the applicability of (5.4) to several weighted layers by considering FC data derived from correlated activity from MEG data obtained for the HCP's MEG2 release (Van Essen *et al.*, 2013), which contains the MEG signals for 89 subjects (Larson-Prior *et al.*, 2013). We use the post-processed data employed in Tewarie *et al.* (2019), whereby the time courses for each brain region are derived from covariance between signals in different frequency bands, which is conveniently parcellated using the same 78-node parcellation as the structural human connectome data we have applied in computations. The bands selected correspond to the classical brain rhythms (Cannon *et al.*, 2014): delta (1–4 Hz), theta (4–8 Hz), alpha (8–13 Hz), beta (13-30 Hz) and gamma (30–48 Hz). The Hilbert transform is applied to each time course to extract a phase signal and a Pearson correlation is calculated between every pair of signals across the whole trial to form a static functional connectivity matrix for each frequency band for all subjects. A thorough overview of the techniques involved in acquiring this data is provided in Tewarie *et al.* (2016).

Using this data, we can perform calculations of the 2-layer structure–function clustering metric as in the previous section, using each time-averaged FC for each frequency band to give a qualitative comparison of the how each layer contributes to the clustering of the multiplex compared to the single structural layer. We can further determine how multiple frequency band FC layers cohesively act to facilitate multiplex clustering by computing (5.2) for $M > 2$ to ascertain a more complete characterisation of the relationships that exist between structure and function across different frequency bands.

5.3 Results

5.3.1 Structure–function duplexes

To validate that using the full, weighted SC (as opposed to threshold/binary networks) has an influence on structure–function multiplex clustering, we follow the procedure of Crofts *et al.* (2016). In order to produce results that are qualitatively comparable with those presented by the authors, we used an identical computational setup, apart from the use of the new multiplex measure and different connectomic data. We measure global clustering (as described in section 5.2.3) between structure and function across a 2-dimensional parameter space, $P = [-6, 6]$ and $Q = [-12, 0]$. These parameters modulate inputs to the excitatory and inhibitory neurons, thereby altering the relative output of those populations, making them good candidates to study the dynamical underpinnings of structure-function relations in the Wilson–Cowan model. We note that this is a similar rationale to the choice of the Jansen–Rit model's $\{A, B\}$ parameter space which was the chosen domain for exploring SC–FC relations in the previous chapter, so P and Q may be considered as analogous parameters for this study.

To test whether there are qualitative differences between the emergent FC patterns arising from forward simulations of the model, we measure global clustering when SC is processed in three different scenarios: unthresholded, thresholded and binarised (Figure 5.4). The threshold level was set at 23% of the strongest weights, as used for the SC dataset in chapter 4, which results in 701 bidirectional connections.

We observe highly different organisation of SC–FC clustering relations for the different forms of SC matrix, suggesting that the qualitative topological information removed by the processes of thresholding and binarising have a sig-

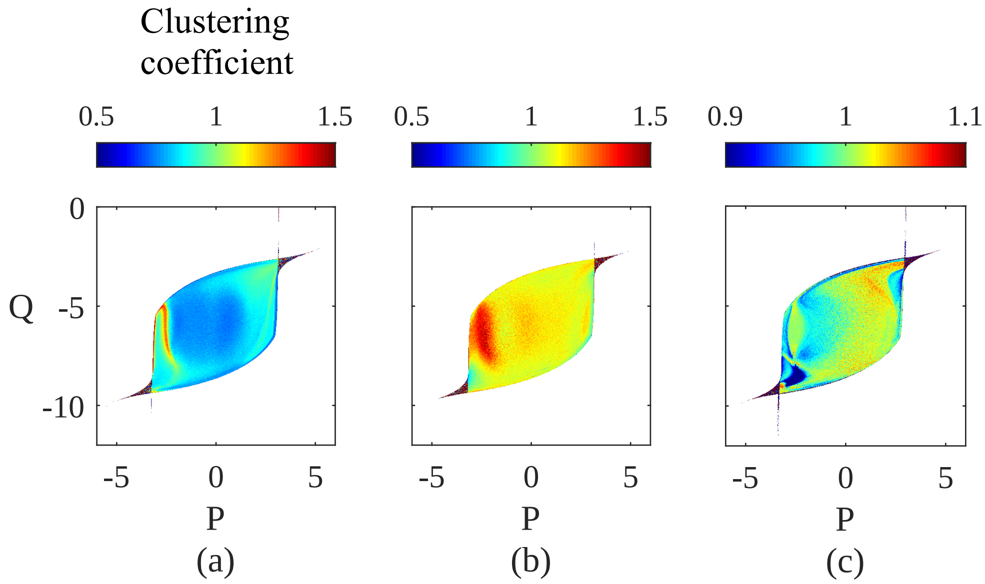

Figure 5.4: SC–FC clustering in the Wilson–Cowan model. We compute the global clustering coefficient, which is the average of (5.4) over the 78 nodes of the brain network, normalised by the mean result for 100 random surrogates for the (a) binary, (b) weighted thresholded and (c) weighted all-to-all networks. We report this over a domain in (P, Q) parameter space, which is uniformly discretised into a 500×500 grid, where the network time series exhibits oscillations. Other parameters are set to $c_1 = c_2 = c_3 = 10$, $c_4 = -2$, $\varepsilon = 0.01$.

nificant effect on the resultant dynamics of the model, in particular the relative phases of oscillation from which we determine FC. Note that the scale of normalised clustering has a smaller range for the full-weighted SC (Figure 5.4(c)). This is due to the surrogates having greater similarity to the original network in this case, which we deduce from the higher Jaccard coefficient reported in Figure 5.3(c), compared to (a) and (b).

It is noteworthy that in contrast with Crofts *et al.* (2016), the structures observed in the P, Q domain (Figure 5.4) are more complex. This is due to employing a more complex structure in the model (a higher node symmetric human network as opposed to directed macaque), which reveals richer network dynamics.

5.3.2 Application to MEG band-passed data

We here present preliminary results for the MEG-derived FC dataset described in secion 5.2.4, where we compare local clustering for each node in each of the five duplexes, formed of the SC layer and a layer representing time-averaged FC in a particular frequency band. Each clustering value is normalised by its corresponding value taken from the mean of 100 surrogate multiplexes, formed from randomised SC and FC layers. As in section 5.2.3, these are randomised using 100,000 iterations of the appropriate randomisation algorithm.

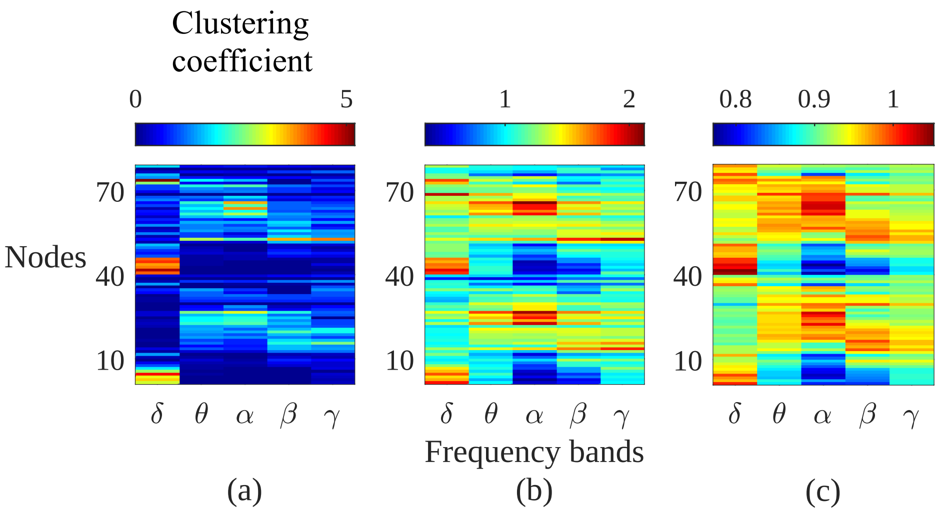

Figure 5.5: Structure–function clustering in different frequency bands. We record the clustering coefficient given by (5.4) for a duplex composed of a structural layer and a functional layer derived from each of the five frequency bands, where the structure is given by (a) a binary, (b) a weighted thresholded, (c) a all-to-all weighted connectivity matrix.

It is clear from this data that clustering using (5.4) reveals greatly different SC–FC relationships for different frequency bands, and that these differences are accentuated by thresholding and binarising the matrices. Though a general structure is preserved for all three network types, there are details in the relative clustering between nodes that does not persist. The ranges of values reported are highest for the binary SC and lowest for the all-to-all network. Comparing (b) and (c), there appears to be a comparable organisation of clustering values for the all-to-all and thresholded networks, suggesting that the weaker connections' topology contributes little to the clusteredness of the multiplex. As alluded to at the start of this chapter, application to the binary forms of the matrices isolates highly clustered nodes, but washes out some of the richer relationships apparent in the weighted examples.

5.4 Future work: Dynamic FC using sliding-windows

One of the drawbacks of performing network measures on FC averaged over a long time period is that these static networks lose the notion of temporal variability which may reveal interesting transient relationships in the MEG data (Hutchison *et al.*, 2013a; Hansen *et al.*, 2015). A sliding window approach has the potential to address this (O'Neill *et al.*, 2017; Preti *et al.*, 2017), whereby FC matrices measured over short epochs are concatenated into a chronological sequence of FC evolution (Figure 5.6).

Sliding windows are particularly useful for exploring SC–FC relationships in task-based datasets, whereby qualitative changes in the organisation of FC are apparent during task state (Gonzalez-Castillo and Bandettini, 2018). Furthermore, dynamically changing FC has also been extensively studied in resting-state data (Allen *et al.*, 2014; Hansen *et al.*, 2015), whereby dynamic transitions between different resting-state networks, such as those identified by Yeo *et al.* (2011), are observed. We propose that the clustering metric (5.4) offers a novel way to investigate these switching phenomena, since it offers a way to measure the emergent behaviour of functional connections between structurally unconnected regions, which show high variability over short timescales (Honey *et al.*, 2007).

The resulting FC matrices can then be investigated in the same way as described in the previous section, where layers represent FC measured within a window for different frequency bands and we report the evolution of multiplex clustering over time. However, it may also be of interest to construct a multiplex where layers are defined as FC matrices calculated during different epochs time series. In this case, we may consider substituting the underlying structural layer and secondary functional layers in equation (5.4) for FC matrices corresponding to consecutive windows of activity. The clustering metric could then be used to quantify the degree to which the FC changes between

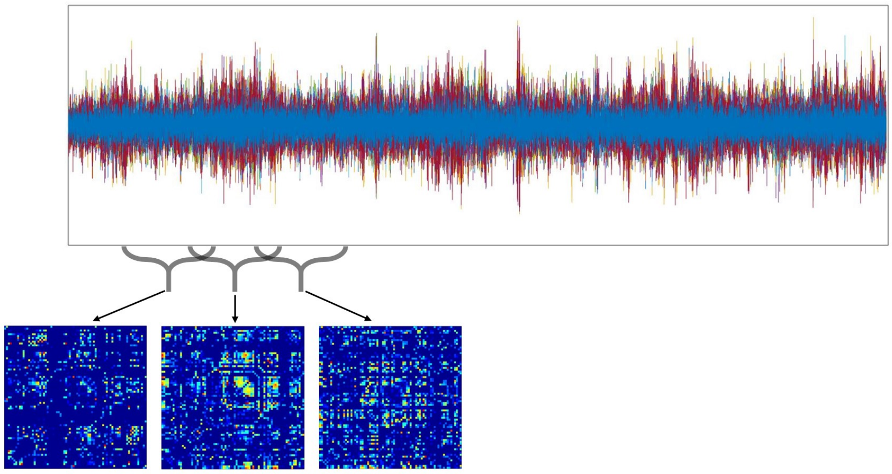

Figure 5.6: Sliding-window dynamic FC. An example of overlapping windows over portions of the time series, within which FC is measured in order to produce a sequence of FC matrices, each representing a snapshot of the temporal coherence for a single epoch.

epochs, which may possibly highlight biomarkers for the dynamic switching observed in resting-state data.

5.5 Discussion

In this chapter we have developed a novel clustering measure to interrogate weighted brain networks. The measure is useful for quantifying the degree to which edges in a multiplex layer increases clustering relative to the single-layer measures. In the specific SC–FC case, it can tell us how strong functional connections are likely to be between neighbouring nodes when SC connections are weak. Extending the work of Crofts *et al.* (2016), we have produced additional results for weighted brain networks, showing that by modulating the dynamics of a neural mass network model we can achieve different SC–FC relationships dependent on whether the underlying SC is weighted, thresholded or binarised. We note the contrast to the previous chapter, where our interest mainly lay in understanding how SC–FC relations emerged from dynamics at the node level, here we use node dynamics as a convenient mechanism to show how altering the structural topology affects network dynamics and, moreover, the emergent temporal coherence that underpins the emergent FC matrices.

We have also described the potential of the metric (5.4) for use in understanding empirical data and present preliminary results for FC computed from MEG time series data. Figure 5.5 is presented as an example of how our clustering coefficient can be used as a novel way to interrogate MEG data, or indeed any brain network data that could be represented as a multiplex network. Indeed, in the interests of learning more about the physiological basis of the SC–FC relationship, the metric may be viewed as the influence of each node on those functional connections that arise from mechanisms other than direct white-matter fibre communication. This could have future benefits in identifying the hub-structure of functional networks (Esfahlani *et al.*, 2020).

Further to this, we have discussed the relevance to dynamic FC, whereby our metric could help reveal transient switching behaviours in resting state data. In the next section, we examine dynamic switching more fully, with a particular focus on the relevance to TMS treatments.

Chapter 6

Computational methods for simulating TMS protocols

Thus far, much of the technical work in this thesis has been concerned with employing neural mass models to study the interplay between structure and dynamics in shaping functional connectivity and analysing the emergent dynamic network states. Though we have discussed in part the nature of multistability within these systems, we have not yet characterised how we can drive the system between states. For instance, in Figure 4.5(a) in chapter 4, individual realisations of Jaccard similarity were computed with different initial conditions and noise distributions, allowing the system to explore a variety of phase-locked states, from which we used an average of many realisations to expose a pattern of SC–FC correlations. While characterisation of all phase-locked states did not prove necessary for the analytical methods employed to elucidate our findings, it would be illuminating to understand whether networks can be driven from one stable state to another with the inclusion of a forcing term in the model. This has particular relevance for brain stimulation, which we introduced in section 2.1.4, whereby we are interested in inducing a transition from one network state to another. A motivating example for this is the switching behaviour of the resting state (Hansen *et al.*, 2015), whereby spontaneous fluctuations in FC reflect the complexity of a brain's function, even when it is not focused on a particular task. As introduced in chapter 2, this is exemplified by the mechanisms of the core networks; an unfocused, daydreaming mind operating in default mode is presented with some environmental stimuli such as a puzzle, which triggers the salience network to activate in order to notice the change and thereby engage the central executive network, which mediates the abstract thought required to solve the problem (Menon, 2011). Moreover, recent studies have shown that external brain stimulation can alter resting-state FC in a comparable way (To *et al.*, 2018; Alkhasli *et al.*, 2019).

This chapter concerns the nature of induced switching between network states in the context of transcranial magnetic stimulation (TMS), a non-invasive method of brain stimulation used for treating a range of psychiatric disorders (see Bersani *et al.* (2013) for a review). The noninvasive approach has the advantage of being safer and less distressing for patients. Clinical procedures can also be repeated easily because all apparatus is external to the patient and any effects due to medication are more readily accountable (Najib *et al.*, 2011). We discussed in section 2.1.4 that TMS has had a substantial impact on the treatment of neurological conditions, particularly in cases of major depression that are unreceptive to medicine (Somani and Kar, 2019).

An issue facing the clinical use of TMS is finding the best stimulation protocols for patient safety and treatment efficacy. There are several parameters to consider such as pulse intensity, frequency and the target site or sites (McClintock *et al.*, 2018). The use of a large network of neural masses as an *in silico* testing ground for ideas about the mechanism and control of brain states is explored in this chapter. As well as using the model to probe the link between structural and functional connectivity, we also explore the response of networks to stimulation (for networks built using human connectome data) and we demonstrate that this has major potential for the design and application of TMS protocols.

In order to build a network model amenable to neuromodulation, we employ a so-called next-generation neural-mass model (Coombes and Byrne, 2019), which is derived from a spiking network model in the infinite population limit. Populations are coupled according to the human connectome, allowing us to interrogate whole-brain dynamics. The model is appropriate to our study since TMS of the cortex has been found to increase the spectral power of oscillations via local synchronisation of neural ensembles (Thut *et al.*, 2011; Vernet *et al.*, 2019), which in turn propagates to other cortical areas to influence global synchrony (Okazaki *et al.*, 2017). This poses a multiscale problem that is can be suitably treated with the next-generation model, since TMS can be incorporated as an effect on the neuronal level, which then influences other populations via long-range white matter coupling. This is more suitable than the models used in chapters 4 and 5, where our focus was on exploring SC–FC relations expediently using low-dimensional neural-mass models. Here, the greater complexity of this model, and particularly its multistable solutions, make it a more suitable candidate for exploring the FC states that emerge from neuromodulation.

In this chapter, we first describe the model we implement, then describe how the multistability of the model (in the simple case of one cortical area in isolation) can be used as a simple analogue for neuromodulatory effects. We pursue similar results on the network level to show that stimulation can reorganise the dynamics of network activity dependent on propagation of stimuli within the structural network. We then investigate the alteration of functional networks due to TMS in the computational model, with particular interest on how the specific topology of FC post-TMS differs depending on target site. Moreover, we explore how stimulation to one cortical area can propagate through the SC to influence global FC and, specifically, how it alters correlation patterns centred on the insula, which is significant in the study of major depression, as we will discuss in section 6.5.

6.1 Next-Generation Neural-Mass Model

The full derivation of the NMM employed in this chapter is outlined in Coombes and Byrne (2019), but we briefly explain the model's formulation here.

We consider a model for a population of neurons with global self-feedback through a set of synapses with overall conductance g. The conductance evolves according to the dynamical system,

$$Qg = \kappa f(Z). \tag{6.1}$$

Here κ is the strength of coupling and the differential operator Q is chosen to best capture the temporal characteristics of synaptic response. $f(Z)$ is the average neuronal firing rate, dependent on the Kuramoto order parameter Z that quantifies synchrony within the population. For the popular α-function synapse, with shape $\alpha^2 t \mathrm{e}^{-\alpha t}\Theta(t)$ (where $\Theta(t)$ denotes the Heaviside step function) following the arrival of an action-potential at time $t = 0$, we would choose

$$Q = \left(1 + \frac{1}{\alpha}\frac{\mathrm{d}}{\mathrm{d}t}\right)^2. \tag{6.2}$$

In order to derive population dynamics from the underlying neuronal activity, it is convenient to consider oscillatory neural dynamics governed by a special class of oscillators for which a mean field reduction is known, via a mathematical technique described in Ott and Antonsen (2008). Their dynamics are described by the quadratic integrate-and-fire network model (Latham *et al.*, 2000),

$$\mathcal{T}\dot{v}_i = \eta_i + v_i^2 + g(v_{\mathrm{syn}} - v_i), \qquad Qg = \frac{\kappa}{N}\sum_{j=1}^{N}\sum_{m\in\mathbf{Z}}\delta(t - T_j^m), \tag{6.3}$$

subject to reset ($v_i \to -\infty$) whenever the neuron fires (v_i reaches $+\infty$ in finite time). These firing events occur at times T_i^m, where m indexes the mth time that neuron i fires. The background drives η_i are chosen from a normalised Lorentzian distribution,

$$L(\nu) = \frac{1}{\pi} \frac{\Delta}{(\nu - \nu_0)^2 + \Delta^2}, \tag{6.4}$$

with centre η_0 and width at half maximum Δ, and v_{syn} corresponds to the synaptic reversal potential of the neurons. In the limit $N \to \infty$, the system can be expressed as a reduced dynamical system using the the Ott–Antonsen ansatz (Ott and Antonsen, 2008), whereby the description of a globally coupled neuronal network with α-function conductance change is given by:

$$\mathcal{T}\dot{Z} = \mathcal{F}(Z; \eta_0, \Delta) + \mathcal{G}(Z, g; v_{\text{syn}}), \tag{6.5}$$

where

$$\begin{aligned} \mathcal{F}(Z; \eta_0, \Delta) &= -i\frac{(Z-1)^2}{2} + \frac{(Z+1)^2}{2}\left[-\Delta + i\eta_0\right] \\ \mathcal{G}(Z, g; v_{\text{syn}}) &= i\frac{(Z+1)^2}{2} v_{\text{syn}} g - \frac{(Z^2-1)}{2} g, \end{aligned} \tag{6.6}$$

and

$$f(Z) = \frac{1}{\pi\mathcal{T}} \text{Re}\left(\frac{1 - Z^*}{1 + Z^*}\right). \tag{6.7}$$

Equation (6.5) describes the evolution of the complex Kuramoto order parameter for synchrony and (6.1) describes how it governs the dynamics of synaptic conductance.

In the same spirit as the Wilson–Cowan model described in 2.2.1, this model can be extended to consider populations of interacting excitatory and inhibitory neurons. In this case we must consider the dynamics of conductances for multiple synaptic connections,

$$Q_{ab} g_{ab} = \varepsilon \kappa_{ab} f(Z_b), \qquad \mathcal{T}_a \frac{\mathrm{d}}{\mathrm{d}t} Z_a = \mathcal{F}_a(Z_a; \eta_0^a, \Delta^a) + \sum_b \mathcal{G}(Z_a, g_{ab}; v_{\text{syn}}^{ab}), \tag{6.8}$$

where $a, b \in \{E, I\}$ represent labels for excitation (E) and inhibition (I), Q_{ab} is obtained from (6.2) under the replacement $\alpha \to \alpha_{ab}$ (so that the time course of synaptic responses can differ), ε scales the magnitude of coupling (set to unity unless stated otherwise) and v_{syn}^{ab} is the reversal potential mediating the current from population a to population b.

Further to this, in correspondence with other models employed in this thesis, we wish to extend the model further to incorporate large-scale connectomic data. To develop a large-scale model incorporating interconnected neural populations across the whole brain, we generalise equation (6.8) to consider N connected populations of excitatory and inhibitory neurons, denoted $E_1, \ldots, E_N,\ I_1, \ldots, I_N$. Therefore, for each network node m we define population order parameters $Z_a \to Z_m^a$ and synaptic conductances $g_{ab} \to g_{ab}^{mn}$ for $a, b \in \{E, I\}$ and $n \in \mathcal{N}(m)$, where $\mathcal{N}(m)$ denotes the set of nodes connected to node m ($n = m$ represents within-node excitatory-inhibitory coupling). We note that since long-range connections in the brain mainly project from excitatory pyramidal cells (Gerfen *et al.*, 2018), we restrict inter-mass coupling to connections between excitatory populations. Constants are denoted similarly, with $(\alpha_{ab},\ \kappa_{ab},\ \eta_0^a,\ \Delta^a,\ v_{\text{syn}}^{ab}, \mathcal{T}_a) \to (\alpha_{ab}^{mn},\ \kappa_{ab}^{mn},\ \eta_{0,m}^a,\ \Delta_m^a,\ v_{mn}^{ab},\ \mathcal{T}_m^a)$.

In the next section, we describe how the model is further extended to accommodate TMS stimulation protocols.

6.2 TMS pulse simulation

TMS pulses are characterised by a rapidly changing magnetic field caused by the fast discharge of capacitors, followed by a slow decay (Rothkegel *et al.*, 2010). Due to Faraday's law (by which electromotive force is caused by a change in magnetic flux) a strong electric field incident on the cortical surface is induced, followed by a much weaker field of the opposite polarity. Pulses may be delivered as singular bursts, or in high-frequency trains referred to as repetitive TMS (rTMS). Pulses are accommodated in our neural mass network model by modulating the average population drive on each node (see equation (6.8)): $\eta_0^a \to \eta_{0,m}^a + p_m^a(t)$, and where $a \in \{E, I\}$ and $m \in \{1, \ldots, N\}$, where the function $p_m^a(t)$ is chosen to reflect the particular delivery protocol. For simplicity, in the following we assume that the induced drive is identical for both inhibitory and excitatory populations, with each pulse given by a damped sinusoid (Triesch *et al.*, 2015):

$$p(t) = I_{\text{peak}} \sin(\omega(t - t_i))\exp((t_i - t)/\tau)\Theta(t - t_i), \tag{6.9}$$

where t_i denotes pulse times, Θ the Heaviside function, $I_{\text{peak}} = 100\ \mu$A is the pulse amplitude, $\omega = 20$ rad/ms is the angular frequency and $\tau = 0.08$ ms characterises the pulse decay time (Rusu *et al.*, 2014). This ensures that the rise time and pulse duration are 50μs and 0.4ms respectively, which are typical for TMS apparatus (Triesch *et al.*, 2015). A plot of a single pulse is shown in Figure 6.1.

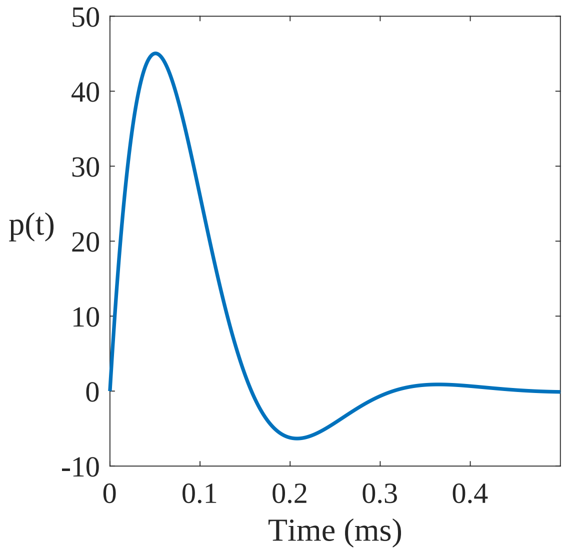

Figure 6.1: A TMS pulse. A simulated TMS pulse constructed from (6.9) with $p_{\text{peak}} = 100$, $\omega = 20\text{ms}^{-1}$ and $\tau = 0.08$ms.

In the following section, we present preliminary computation results in order to demonstrate the applicability of this model to TMS via exploration of its dynamic regimes in both a single-node and network case. We emphasise that we concentrate here on providing results that demonstrate the rich dynamics of the model, rather than pursuing results of specific biological relevance.

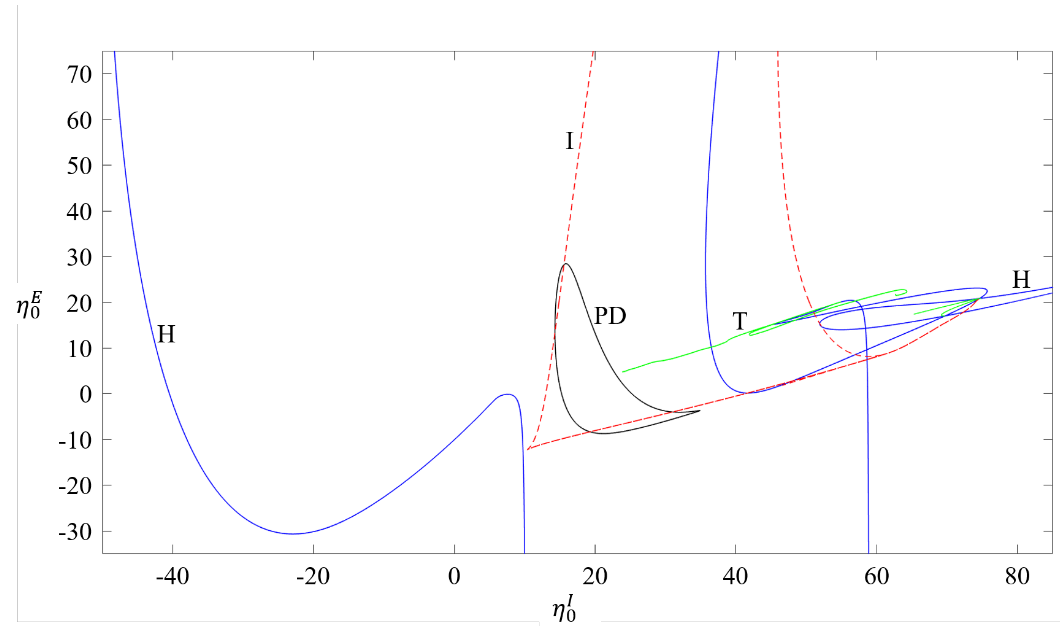

Figure 6.2: Next-Generation NMM bifurcation diagram. Bifurcation sets for (6.8) showing Hopf (H; blue), period-doubling (PD; black) and torus (T; green) sets, as well as limit points of isoli of stable oscillations (I; red), which are regions of oscillations which do not arise from instability of a fixed point (*i.e.* a Hopf bifurcation). η_0^E and η_I^0 are used as bifurcation parameters. Other parameters: $\mathcal{T}_I = \mathcal{T}_E = 1$, $\alpha_{EE} = 1$, $\alpha_{EI} = 0.7$, $\alpha_{IE} = 1.4$, $\alpha_{II} = 0.4$, $\kappa_{EE} = 1.5$, $\kappa_{EI} = 2$, $\kappa_{IE} = 1$, $\kappa_{II} = 3$, $v_{syn}^{EE} = 10$, $v_{syn}^{IE} = -v_{syn}^{EI} = 8$, $v_{syn}^{II} = -12$, $\Delta^E = \Delta^I = 0.5$.

6.3 Bifurcation analysis

In order to gain an insight into the dynamic repertoire of the next-generation NMM presented in section 6.1, here we produce a bifurcation diagram for a single node (constructed using XPPAUT (Ermentrout, 2002)) given by (6.8), where we use the average drives for the excitatory and inhibitory populations, η_0^E and η_0^I respectively, as bifurcation parameters (Figure 6.2). This is primarily to inform us of the parameter sets that allow multistable solutions. In the context of neuromodulation, we are particularly interested in these solutions as these provide a simple paradigm by which to observe switching between dynamic states.

6.4 Timeseries simulations

Poising the system at $\eta_0^E = 20$, $\eta_I^0 = 25$, we have two different types of oscillations, one arising from a Hopf bifurcation and one from the limit points of an isola, a branch of oscillatory solutions that is closed in the parameter space

(Dellwo *et al.*, 1982). To demonstrate driving the system from one oscillatory branch to another, we devised a hypothetical TMS protocol where the model ran for 50 seconds, during which it converged to the smaller-amplitude oscillations arising from the Hopf bifurcation. Then, after 50 seconds we applied a periodic forcing governed by the function (6.9) at a frequency of 30 pulses per second for 50 seconds, then removed the stimulus and let the system settle into the higher-amplitude oscillations associated arsing from the isola (Figure 6.3).

While the choice of stimulation protocol is largely arbitrary, since we only require a stimulation with a high enough magnitude to evoke a shift from the basin attraction of one stable branch of oscillations to another, the pulse frequency chosen has previously shown to induce long-lasting excitation in the motor cortex (Goldsworthy *et al.*, 2012).

Numerically, the system of equations (6.8) was integrated using `ode45` in Matlab®, which uses a dynamic time-stepping algorithm.

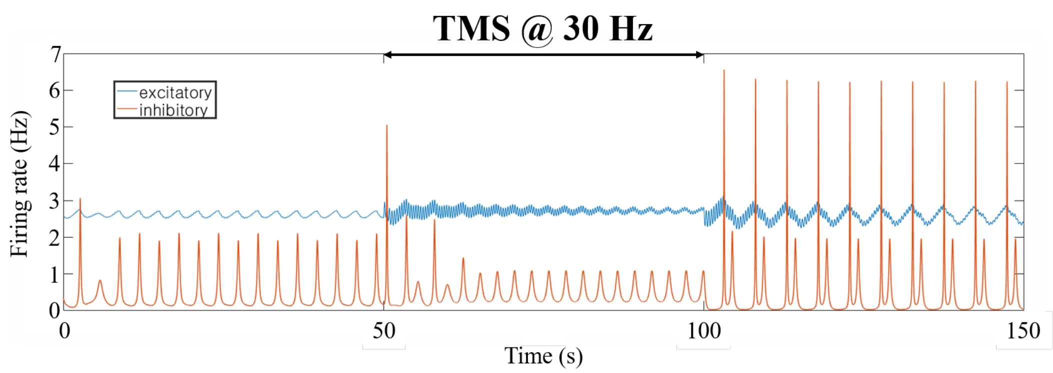

Figure 6.3: TMS in the single-node case. Timeseries solution for a single next-generation model node (6.8) where the dynamical regime permits two different branches of stable oscillations. We apply simulated TMS pulses at 30 Hz. Parameters are the same as for Figure 6.2, with the addition of $\eta_0^E = 20$, $\eta_I^0 = 25$.

As this thesis mainly concerns the distributed brain states that exist on the whole-brain scale, we considered a more relevant test to investigate whether stimulating a single node would propagate via white-matter coupling to force other nodes into different oscillatory regimes. In Figure 6.5, we show an example of this when using the same human structural network employed in previous chapters 4 and 5 and described explicitly in section 4.1. Apart from their connectivity, each node's dynamics is governed by identical parameters, *i.e.* α_{ab}^{mn}, $\eta_{0,m}^{a}$, Δ_m^a, v_{mn}^{ab}, $\mathcal{T}_m^a$ are the same for all nodes m and node pairs (m, n). The inter-node connectivity constants κ_{ab}^{mn} are given by the values of the all-to-all, weighted connectivity matrix. The stimulation protocol is also the same as for the single-node case, which we apply to the node with highest cumulative efferent weights (node 21, the left angular gyrus, whose position is visualised in Figure 6.4). This stimualtion site was chosen on the assumption that its relatively strong connectedness would give it a high influence on the network, resulting in prominent changes in dynamics. As a proxy for the varied oscillatory states that could be exhibited by brain rhythms from different regions, we gave each node different initial conditions so that their solution trajectories may settle onto different limit cycles.

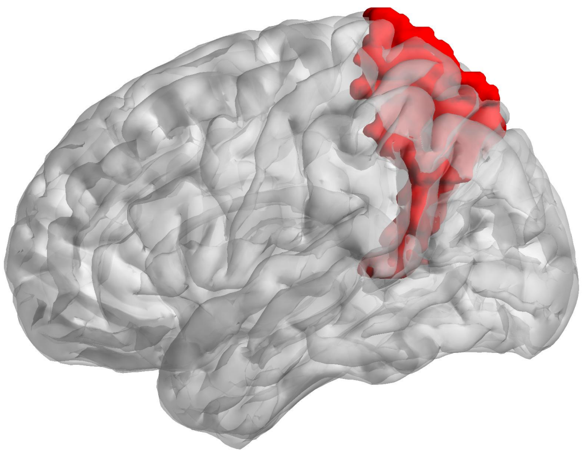

Figure 6.4: Visualisation of the left angular gyrus. This shows the size and position in the human cerebrum of the ROI stimulated in the next-generation NMM network, with results described in Figure 6.5.

In Figure 6.5, we illustrate the types of dynamical change that can be induced via our simulated TMS protocol and highlight particular cases in panel (a). In red, the solution shifts from non-uniform oscillations to regular periodic activity, as illustrated in (b). In cyan, we observe similar a dynamic shift between two branches of limit cycles, plotted in (c), as also shown for the single-node case (Figure 6.3). Finally in magenta, the node's relative phase is shifted due to stimulation, whereas other nodes are mostly synchronous before and after TMS pulses are applied. These results provide an indication of the suitability of our approach to investigate dynamical changes in neural activity brought about by TMS, by demonstrating that periodic drive to a node causes dynamic changes that propagate via structural couplings to give rise to alterations of the wider network's dynamics. In the following section, we study how altering the target site of TMS can provoke changes in FC. In particular, we consider the effect on the insula, which has been implicated as a cause of major depression as discussed in the following section.

6.5 Case study: Non-direct stimulation of the insula

The insula has been identified as a causal component of abnormalities in (Liu *et al.*, 2010; Horn *et al.*, 2010; Avery *et al.*, 2014), and interactions between (Mayberg, 1997), functional networks implicated in depression. This reflects its role as a component of the neurological switching mechanism which allows the brain to transition between the core functional subnetworks (namely the default-mode, salience and central executive networks) (Menon and Uddin, 2010; Sridharan *et al.*, 2008). However, since TMS induces a current on surface regions, sub-cortical regions such as the insula must be influenced indirectly (Iwabuchi *et al.*, 2017); the mechanisms by which this occurs, and ideal stimulation protocols to achieve this remain unclear. In this section, we use the next-generation model (6.8) to investigate how we can change the functional connectivity of the insula via stimulation of non-local target sites, describing the *in silico* experimental setup in 6.5.1, the stimulation protocol in 6.5.2 and finally discussion of results in 6.5.3.

6.5.1 FC simulation and visualisation

Utilising the TMS modelling framework discussed earlier, we used an SC described in (Abeysuriya *et al.*, 2018), which is produced using the same

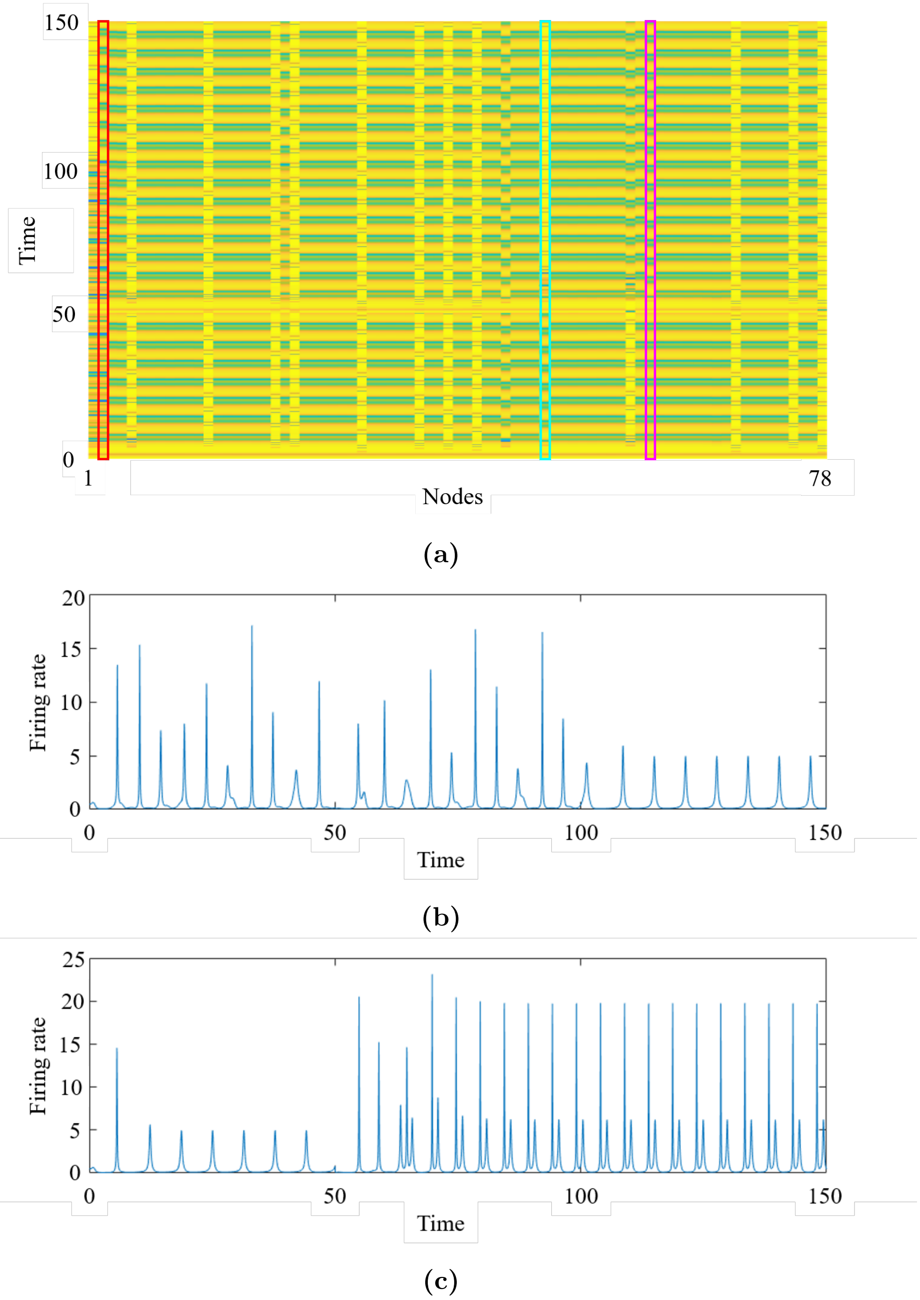

Figure 6.5: TMS propagation in a network. (a) Time series for the average firing rate of inhibitory neurons in each of 78 next-generation nodes, with connectivity informed by human SC. We apply simulated TMS pulses at 30 Hz to node 21, which has the highest sum of connectivity weights. We have highlighted time series from other nodes that display switching between particular dynamics and present these time series in panels (b) and (c). In red, the solution shifts from non-uniform oscillations to regular periodic activity, as illustrated in (b). In cyan, we observe similar a dynamic shift between two branches of limit cycles, plotted in (c). The magenta box indicates a case where the solution settles to the original limit cycle post-TMS.

tractography processes described in chapter 4 but is parcellated onto the atlas of Desikan *et al.* (2006), chosen for the readily available geometric data for brain network visualisation. This atlas also has fewer regions than that used in chapters 4 and 5, 68 as opposed to 78, so there is a benefit for computational efficiency when running forward simulations of network dynamics in the next-generation network model, which contains more ODEs than the NMMs employed in those chapters.

Functional connectivity is obtained, similarly to chapters 4 and 5, by direct simulation of the next-generation neural mass network, and computing the pairwise synchronisation between time-series activity on each network node, measured via mean phase coherence (Mormann *et al.*, 2000), to provide a matrix describing the strength of functional connection between each brain region. Each node was given random initial conditions to facilitate varied dynamics across the network, thereby encouraging diverse temporal correlations for richer FC patterns. Structure–function relations are assessed by computing the Jaccard similarity coefficient (Jaccard, 1912) of the non-diagonal entries of the binarised SC and FC matrices, which provides a natural measure of matrix overlap, ranging from 0 for matrices with no common links to 1 for identical matrices. The multiplex measure, discussed in the previous chapter, is not considered here, since the Jaccard measure offers a more direct comparison of structure–function as opposed to the more specialised multiplex clustering coefficient. All simulations were performed in Julia (Bezanson *et al.*, 2017) using the `DifferentialEquations` package.

Results visualising both the structural and derived functional networks, in absence of TMS, are shown in Figure 6.6; these show how FC patterns can differ significantly from the underlying connectome structure that supports neural population activity. We choose node degree as the metric of interest in brain visualisations, since it presents a convenient medium through which to compare nodes' connectedness in different contexts. In the following, we describe how the model and approaches described above can be employed to understand the influence of brain stimulation treatments on network behaviour.

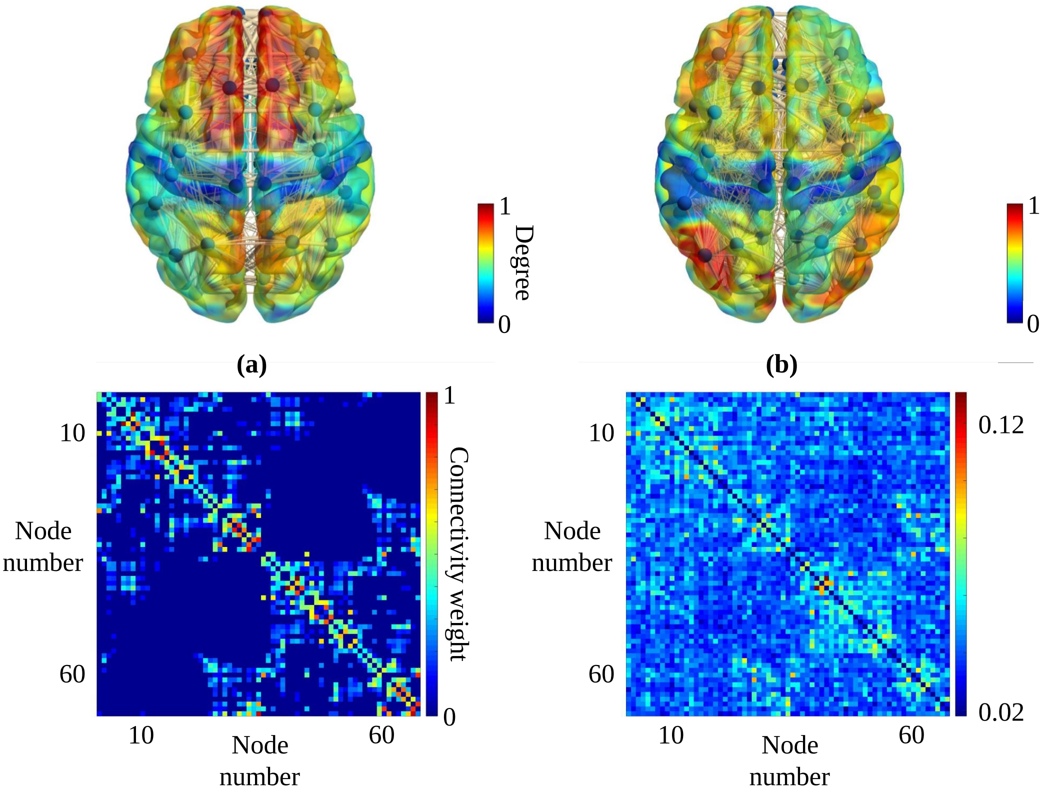

Figure 6.6: SC–FC visualisation. Visual representation of (a) the structural network and (b) the simulated functional network for 68 nodes parcellated according to the Desikan–Killiany atlas. The surface of the brain visualisations are coloured depending on nodal degree, which was normalised by the highest element for easier comparison between SC and FC. The upper surface plots highlight the strong differences between SC and FC patterns. The network graphs are shown on the bottom row. Parameter values: $\alpha_{EE}^{mn} = 1$, $\alpha_{IE}^{mn} = 1.4$, $\alpha_{EI}^{mn} = 0.7$, $\alpha_{II}^{mn} = 0.4$, $\kappa_{EE}^{mn} = 1.5$, $\kappa_{IE}^{nn} = 1$, $\kappa_{EI}^{nn} = 2$, $\kappa_{II}^{nn} = 3$, $v_{EE} = 10$, $v_{mn}^{IE} = 8$, $v_{mn}^{EI} = -8$, $v_{\mathrm{syn},mn}^{II} = -12$, $\Delta_m^E = 0.5$, $\Delta_m^I = 0.5$, $\eta_{0,m}^I = -20$, $\eta_{0,m}^E = 20$, $\mathcal{T}_m^a = 1$; values of κ_{EE}^{mn} are obtained from MRI data (see text), scaled by a global coupling strength $\varepsilon = 0.025$.

6.5.2 Stimulation protocol

We stimulated in turn each of the 14 nodes corresponding to cortical brain regions. We computed the resulting FC network from simulated time-series activity on each node (as described above), paying particular attention to the influence on the right anterior insula. In each case, we employed an rTMS stimulation protocol at 20 Hz, which has been used in a previous depression study (George *et al.*, 1995). TMS was applied for 50 seconds; functional connectivity was computed after a delay of 50 seconds post-TMS. These timescales were chosen on the basis of computational considerations, since we deemed these sufficient for to allow the solution trajectories' transients to settle to stable oscillatory states after the onset and termination of stimulation. Moreover, this *in silico* protocol provides a computationally tractable way to test whether the model is able to produce a variety of network states due to targeting different nodes with external stimulation. Furthermore, as in 6.4, we reiterate that the stimulation and measurement protocol adopted here was chosen for illustrative purposes of proof of concept, rather than to mimic a TMS experiment.

6.5.3 Results

Figures 6.7 and 6.8 summarise our results. Fig. 6.7 shows a representation of the functional network arising from stimulation of each cortical node, interpolated onto brain meshes of the right hemisphere, together with the node corresponding to the insula (right hemisphere). Here, the weighted degree of each node in the FC graph was calculated and normalised by highest degree. The global SC–FC similarity (measured by the Jaccard similarity coefficient) is also shown. These results highlight the dramatic difference that stimulating distinct cortical sites can make to both the overall pattern of functional connectivity, and the resulting influence on the insula, in particular. This is explored in more detail in Fig. 6.8, which shows the influence of each stimulated region on some exemplar graph-theoretical properties (as discussed in Rubinov and Sporns (2010a) and Newman (2016)) of the insula node (specifically, the node degree, eigencentrality and clustering coefficient), together with the path-length between the stimulation site and the insula. These results again highlight the strong dependence of emergent FC on stimulation site indicated in Fig. 6.7, both in terms of global SC–FC similarity, and specific influence on the insula. Moreover, the efficacy of stimulation is not strongly predicted by proximity (as measured by shortest path length connecting the stimulation site, and the insula), highlighting a non-trivial dependence on macroscopic brain

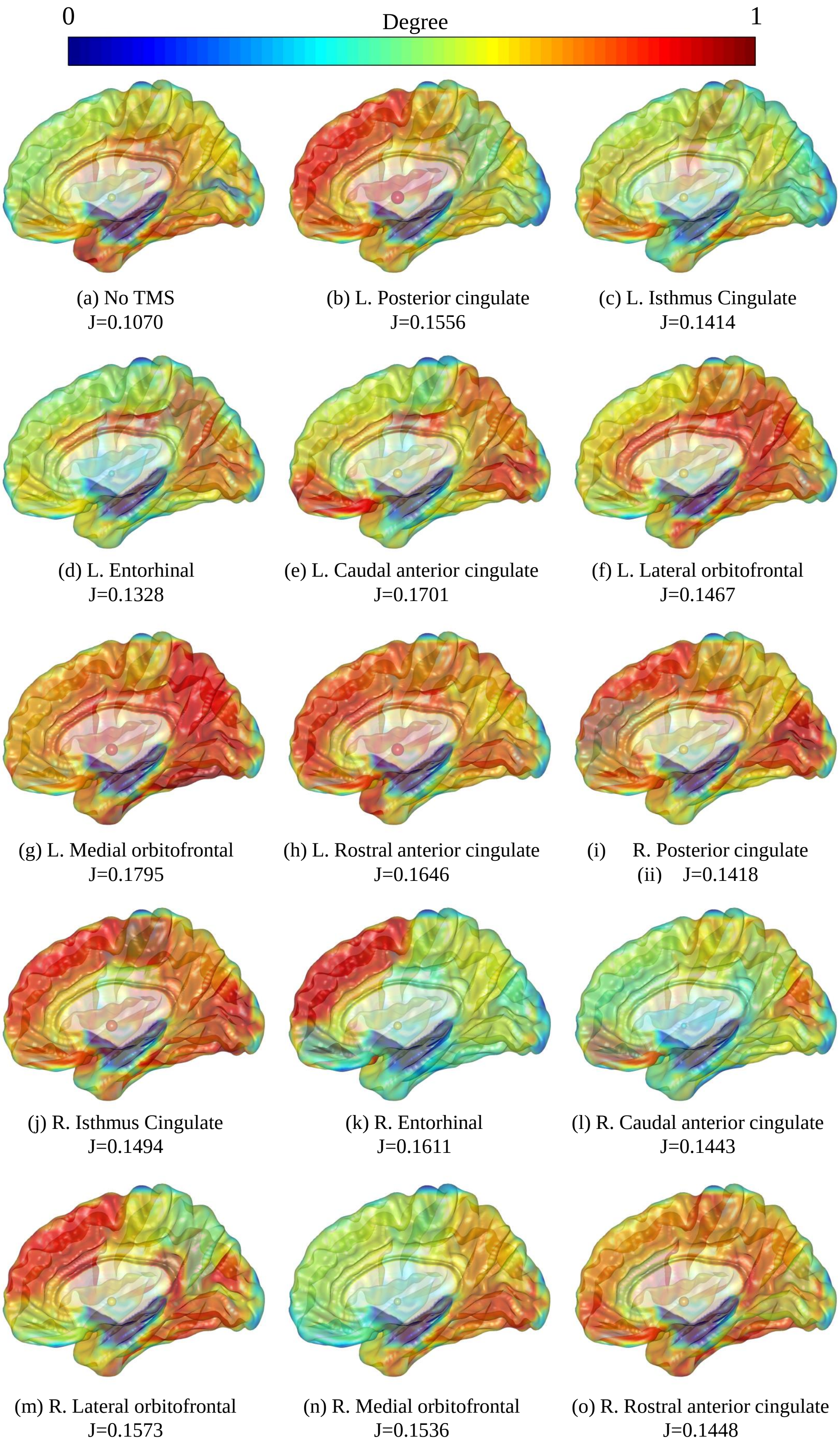

Figure 6.7: Normalised node degree of FC networks under rTMS stimulation of each cortical area. FC matrices are interpolated on brain meshes of the right hemisphere. The node representing the right anterior insula is also shown to depict the relative influence on stimulation of nodes on a specific sub-cortical region. Also shown for each target region is J, the Jaccard similarity coefficient between the SC and FC matrices. Figures created with BrainNet Viewer (Xia *et al.*, 2013). Parameters as in Fig. 6.6.

network architecture. We have shown results from a range of target regions

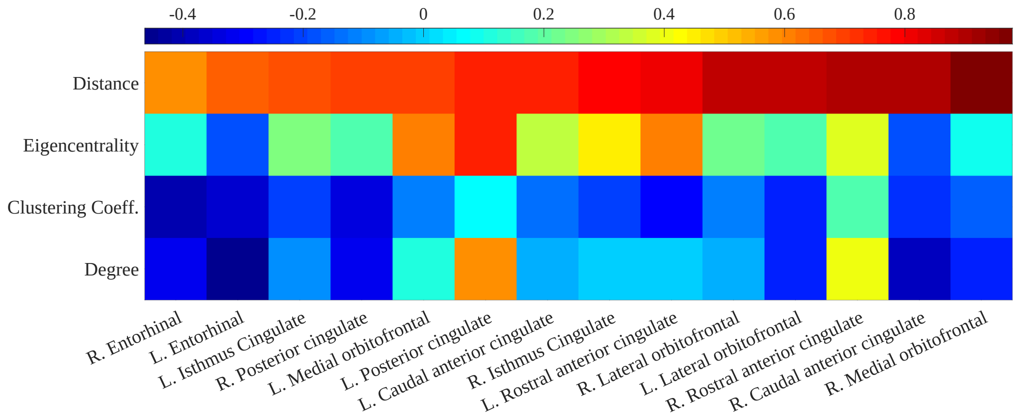

Figure 6.8: Graph properties of the right anterior insula in FC networks obtained under rTMS stimulation of each cortical area. Shown is: the shortest path length between the stimulated area and the right anterior insula; and the eigencentrality, clustering coefficient, and node degree of the insula node. Parameters as in Fig. 6.7.

to show the variability of simulated TMS-induced FC states. However, more clinically relevant TMS protocols could be implemented such as stimulation of the dorsolateral prefrontal cortex, which has frequently been the subject of TMS studies related to the treatment of major depression (Noda *et al.*, 2015; Lan *et al.*, 2016).

6.6 Incorporating of conduction delays

One of the most well-studied effects of TMS applied to the cortex is neuroplasticity (Siebner and Rothwell, 2003; Zrenner *et al.*, 2018; Chung *et al.*, 2017; Freitas *et al.*, 2013).The proposed mechanism for this is via TMS protocols that induce bursts of theta activity within the target area, which are thought to modulate synchronisation between areas exhibiting neuronal activity (Vernet *et al.*, 2013). While this is the subject of debate, it is an active area of research, since it holds promise for providing a therapeutic procedure to induce significant functional alterations in patients who suffer from a variety of neurological and psychiatric conditions (Ridding and Ziemann, 2010).

Computationally, we may consider these plastic effects to manifest themselves in the next-generation network model as changes in delays of synaptic conduction between neuronal populations (Knoblauch and Sommer, 2003), which may be used to facilitate the emergence of preferable functional network states (Madadi Asl *et al.*, 2018). This is especially relevant in the context of neurological disorders, since it has also been shown that normal brain activity is highly sensitive to conduction delays mediated by white-matter myelin plasticity (Fields, 2008; Pajevic *et al.*, 2014).

The specific case of TMS-induced plasticity has been studied as a homeostatic effect, whereby brain structures change as a regulatory response to the external stimuli (Ziemann, 2004; Müller *et al.*, 2007). Though algorithms have been developed for this kind of plasticity and applied in mathematical models (*e.g.* Nicola *et al.* (2018)and Hellyer *et al.* (2016)), we here tackle the more fundamental question of how adding delays to the model construction affects the neural mass network's dynamics.

As described in chapter 3, modulation of dynamics via delays in neural mass networks can be analysed using the eigenvalue spectra derived from linear analysis, which is formulated for a general NMM in section 3.3. Moreover, these have recently been shown to destabilise different eigenmodes to expose particular FC patterns (Tewarie *et al.*, 2019). We consider in greater depth the analysis of such delayed systems in chapter 7, but we here present a motivating computational test to demonstrate the influence of the inclusion of delays on the dynamics of the next-generation NMM. Specifically, we wish to show that it is possible to generate oscillations in the network via a delay-induced Hopf bifurcation.

We construct delays based on pairwise euclidean distance between the centres of mass of each brain region, divided by a uniform conduction velocity of 10ms^{-1}. This delay is applied to synaptic transmission between brain regions, which is implemented in the model by altering the necessary equations in (6.8), namely $Q_{ab}g_{ab}(t) = \kappa_{ab}f(Z_b(t)) \rightarrow Q_{ab}g_{ab}(t) = \kappa_{ab}f(Z_b(t-\tau_{ab}))$, where τ_{ab} represents the conduction time between the excitatory populations of nodes

a and b. We poised the system close in parameter space to a Hopf bifurcation, then integrated the equations to steady state. Then, we set initial conditions for the delayed counterpart by perturbing the solution from steady state and integrate the delayed system using Julia's `DelayDifferentialEquations` package. The results for both of these computations is displayed in Figure 6.9, showing that the inclusion of delays does indeed cause stable oscillatory dynamics to arise.

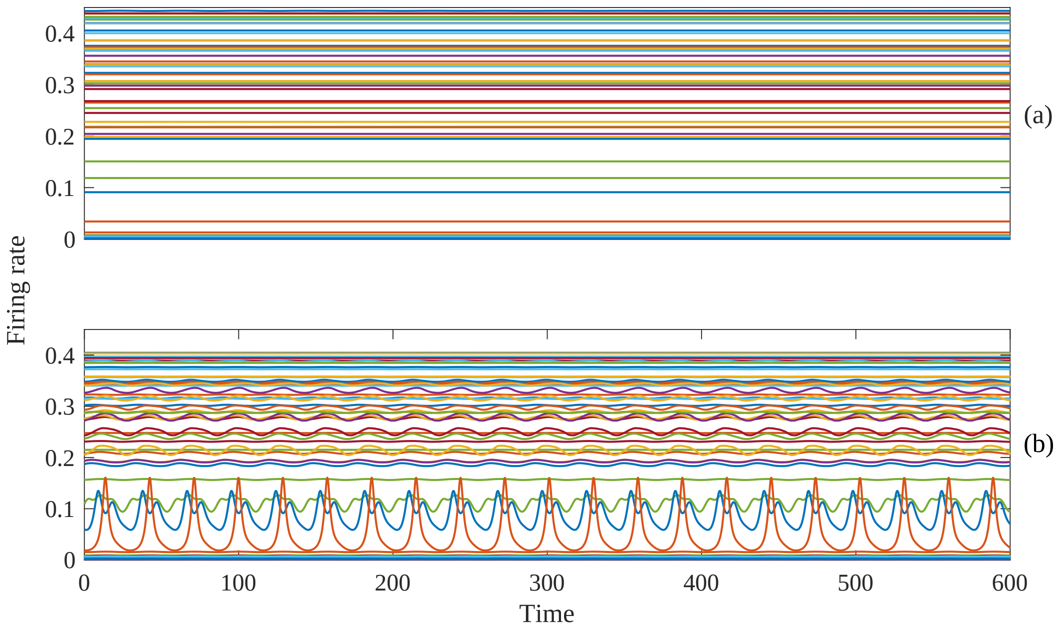

Figure 6.9: Delay-induced oscillations. (a) Steady state of the system described by 6.8, with parameters set to $\alpha_{EE}^{mn} = 0.12$, $\alpha_{IE}^{mn} = 0.0254$, $\alpha_{EI}^{mn} = 0.24$, $\alpha_{II}^{mn} = 0.08$, $\kappa_{EE}^{mn} = 5\pi($ for $m = n)$, $\kappa_{IE}^{mn} = 4\pi$, $\kappa_{EI}^{mn} = 10\pi$, $\kappa_{II}^{mn} = 15\pi$, $\eta_{0,E}^{a} = 10$, $\eta_{0,I}^{a} = -40$, $\Delta_m^E = 0.5$, $\Delta_m^I = 0.5$, $v_{mn}^{EE} = 6$, $v_{mn}^{IE} = 10$, $v_{mn}^{EI} = -10$, $v_{mn}^{II} = -10$, $\mathcal{T}_m^E = 5$, $\mathcal{T}_m^I = 5$, which are the same for all nodes/node pairs m and n. κ_{EE}^{mn} for $m \neq n$ (*i.e.* inter-node connectivity constants) are defined by their corresponding value in the connectivity matrix. (b) The solution for the same parameters when conduction delays are applied to coupled variables, governed by a Euclidean distance d_{ij} divided by a uniform conduction velocity of 10ms^{-1}.

6.7 Discussion

In this chapter, we have introduced a framework for modelling brain stimulation using a recently developed neural mass model. Our results demonstrate a range of uses for exploring several facets that may be useful for studying the effects of different stimulation protocols, with particular emphasis on the application of TMS due to its growing popularity as a therapeutic treatment for neurological diseases. We have shown that both oscillatory and functional properties of network behaviour can be modulated via application of simulated TMS pulses and have also provided a preliminary set of results to demonstrate how these can be further modulated by investigating plastic effects induced by TMS therapy and, moreover, its impact on conductivity in the brain.

While the particular dynamical regimes employed here present an expedient way to demonstrate the model's efficacy in providing results that exhibit different types of neural 'switching', which we believe to be relevant in the study of TMS, it leaves room for much more work to be conducted in order to better understand the variation of network activity as a result of different stimulation protocols. In particular, it would be interesting to fit the (function) data derived from simulated activity to real FC data from patients before and after TMS treatment to give confidence that the model is capable of reproducing empirical results. If there is sufficient confidence in the model's performance, a variety of protocols could then be tested to determine relative efficacy and potentially inform better treatment practises.

From a theoretical perspective, there is much more analytical work that may be conducted to better understand the network model's behaviour. In the next chapter, we study in greater depth two analytical questions arising from this chapter. The first concerns how the rhythm caused by periodic stimulation, such as in Figure 6.3, is related to the frequency and amplitude of pulses. The second is to better understand the delay-induced oscillations displayed in Figure 6.9 and how these arise from instabilities as revealed by the spectra of linearised eigenvalues of the model steady state.

Chapter 7

Analytical methods for exploring neuromodulatory effects

7.1 Introduction

Chapter 6 consolidates initial studies into the applicability of the next-generation NMM for studying TMS. The computational tests therein represent preliminary groundwork that illustrate the versatility of the model in different contexts related to TMS, *i.e.* mechanisms of switching between network states and the potential modulation of white-matter conduction delays associated with neural plasticity.

In this chapter, we aim to elucidate some of the mathematical underpinnings of the results presented in chapter 6, in order to better understand how those results arose and also to gain insight into how the model could be further manipulated in order to make it more applicable to current challenges in the field of TMS study. The topics considered here can are relevant to the study of neuromodulation more generally, which concerns how the plastic, oscillatory and network properties of the brain can be affected *e.g.* by administering drugs or employing electrical/magnetic stimulation. Specifically, we here treat the issues of entrainment and axonal plasticity by exploring the effects of simulated periodic drive and conduction delays in the next generation NMM.

This chapter is split into two distinct parts. In the first we investigate the nature of entrainment of oscillations by means of external forcing. We have already discussed the importance of entrainment of neural populations' activity (by rhythmic TMS) in relation to neural plasticity in section 6.6, but it is also important in other neurological contexts. There has been considerable focus on utilising TMS to reduce involuntary motor movement associated with Parkinson's disease (Brittain *et al.*, 2013) and Tourette's syndrome (Mantovani *et al.*, 2007; Le *et al.*, 2013; Kwon *et al.*, 2011). Of particular interest is the spectral power of oscillations in the beta band, which has been used as a biomarker for motor response due to the observed decrease in power during movement (Armstrong *et al.*, 2018). Since brain oscillations seen in EEG/MEG are thought to reflect the underlying population synchrony of neuronal firing, a relevant computational problem is to understand conditions for which model neural oscillators can be entrained to a rhythm, with the expectation that such techniques will inform clinical TMS techniques used to treat *e.g.* the abnormal EEG signals correlated with tics (Schnitzler and Gross, 2005). For instance, it has recently been shown in Maiquez *et al.* (2020) that entraining sensorimotor mu-rhythms by delivering pulses of median nerve stimulation to the wrists of Tourette's syndrome patients significantly reduced the frequency of their tics. A natural way to study such systems is through mathematical analysis of driven oscillators, given by Lyapunov exponents and Arnol'd tongues, in order to determine the stability and frequency of entrained rhythms, which may be used to prime models for simulating neural entrainment.

In the second part of this chapter we return to the issue of how delays in the network model influence emergent behaviour, such as oscillatory activity and coherence, as introduced in the previous chapter (section 6.6). Here, we pursue a similar methodology to Tewarie *et al.* (2019), whereby our main focus is to use linear theory to explain how the modulation of conduction velocities along axons can cause instabilities of particular eigenmodes of the network connectivity matrix, resulting in corresponding patterns of network activity.

Despite the complexity of the next-generation model relative to the other NMMs employed in this thesis, we are able to generate our results by using straightforward implementations of well-established mathematical theories. We explore possible further applications of the model in the discussion.

7.2 Entrainment of neural oscillators via periodic forcing

The mathematical theory behind the response of forced oscillators is well established and in this section we discuss and apply techniques appropriate for the study of TMS. However, we point the interested reader to relevant chapters of the book 'Synchronisation' (Pikovsky *et al.*, 2003) for a comprehensive overview of the subject. Entrainment is defined here as exposing a 'slave' oscillator to a rhythmic 'drive' so that the slave's dynamics converges to a frequency-locked state, such that there is a fixed ratio between the period of slave and the drive: the rotation number r.

Recall from chapter 1 (section 3.4) that we can study the effect of a small perturbation on an oscillator using a phase response function. This theory is suitable for weakly-driven oscillators, with a small deviation between the intrinsic dynamics and drive . However, in the case of entrainment, the external input must be of high enough magnitude in order for the slave to frequency-lock with the drive, meaning that this weakly-driven theory is unsuitable in this context (since frequencies are not necessarily similar). The analysis in this section is instead based on the theory of Lyapunov exponents (see *e.g.* (Pikovsky and Politi, 2016) for a recent survey) and Arnol'd Tongues (Boyland, 1986), which allows us to visualise, in a 2D domain of drive frequency and magnitude, where entrainment occurs. In the following sections we outline the mathematical theory and the computational method to generate such results numerically.

7.2.1 Lyapunov Exponents and Arnol'd Tongues

Lyapunov exponents characterise how quickly the distance between two trajectories of a dyanmical system will grow. When a forced system converges to a stable trajectory, it is defined to be entrained. Conversely, if the slave's frequency does not converge it will exhibit chaotic behaviour or aperiodicity (in the case of a zero exponent). The dynamics of a chaotic system differ greatly depending on initial conditions; a property known as sensitive dependence. To illustrate this mathematically, we first take a general M-dimensional dynamical system represented by the flow,

$$\dot{\mathbf{U}}(t) = \mathbf{F}(\mathbf{U}(t)). \tag{7.1}$$

Consider a trajectory along this flow, $\mathbf{x}(t)$, which is perturbed to a new trajectory $\mathbf{y}(t)$ such that $\mathbf{x}(t)$ and $\mathbf{y}(t)$ are close enough so that their distance apart evolves approximately linearly. At an infinitesimally small time Δt later, the difference between them can be written,

$$\mathbf{x}(t+\Delta t) - \mathbf{y}(t+\Delta t) \approx \mathbf{x}(t) - \mathbf{y}(t) + \Delta t(\mathbf{x}(t) - \mathbf{y}(t)) \cdot D\mathbf{F}|_{\mathbf{x}(t)}, \tag{7.2}$$

where $D\mathbf{F}$ is the Jacobian of the flow. Our goal is to determine whether $\mathbf{y}(t)$ stays close to $\mathbf{x}(t)$ by assuming the evolution of the trajectories' difference is given by,

$$|\mathbf{x}(t+\Delta t) - \mathbf{y}(t+\Delta t)| = e^{\lambda \Delta t}|\mathbf{x}(t) - \mathbf{y}(t)|, \tag{7.3}$$

where λ is a Lyapunov exponent. For systems of M dimensions, there is a corresponding set of M Lyapunov exponents, though for analysing whether the oscillator will be chaotic/entrained it is sufficient to compute just the largest Lyapunov exponent (LLE) because this will dominate the perturbation's evolution $\mathbf{u}(t)$. Therefore we only concern ourselves with how the solution changes in the most expanding direction, which from (7.2) is given by,

$$|\mathbf{x}(t + \Delta t) - \mathbf{y}(t + \Delta t)| \approx |[I + \Delta t D\mathbf{F}|_{\mathbf{x}(t)}] \cdot (\mathbf{x}(t) - \mathbf{y}(t))|, \tag{7.4}$$

where I is the identity matrix. If the stretching $|\mathbf{x}(t) - \mathbf{y}(t)|$ is normalised, then we have by (7.3),

$$\lambda = \ln(|\mathbf{x}(t + \Delta t) - \mathbf{y}(t + \Delta t)|)/\Delta t \tag{7.5}$$

In this form we can make a further approximation using Birkhoff's theorem (Birkhoff, 1931), whereby the LLE asymptotically approaches the true value $\lambda^\star$ by recursively measuring (7.5) along the trajectory,

$$\lambda^\star = \lim_{T\to\infty} \frac{1}{T} \sum_{i=0}^{N} \ln(|\mathbf{x}(i\Delta t) - \mathbf{y}(i\Delta t)|), \tag{7.6}$$

where T is the total time and $N = T/\Delta t$. Note that we have outlined the method for an autonomous system. For a driven, non-autonomous system, we can augment this by including time as an extra dependent variable in the system. The pseudocode in Algorithm 2 outlines the procedure, where we define our initial pertubation to be a random normalised vector $\mathbf{w}$.

Now consider $\mathbf{F}(\mathbf{U}(t), t) = \mathbf{g}(\mathbf{U}(\mathbf{t})) + \boldsymbol{\Omega}(S, f, t)$, where g describes a slave dynamical system and $\boldsymbol{\Omega}(S, f, t)$ is some periodic drive of magnitude S and frequency f. To construct Arnol'd Tongues, we determine points in (f, S) parameter space where Algorithm 2 reports a negative LLE, indicating that oscillations are stable. We also record frequency locking with rotation number r, given by $f \times$ Period of slave oscillator.

7.2.2 Results

We applied Algorithm 2 to a single next-generation population model, with dynamics governed by equations (6.1), (6.5) and (6.6). A sinusoidal drive, filtered by the α-function (6.2), was added to the base input, η_0 so that intrinsic

Algorithm 2 Algorithm to find the LLE

procedure LargestLyapunov($\mathbf{F}$, $\mathbf{U}_0$, T^{init}, Δt, N)

  for $0 \to T^{init}$ **do**

    solve $\dot{\mathbf{U}}(t) = \mathbf{F}(\mathbf{U}(t)), \quad \mathbf{U}(0) = \mathbf{U}_0$ ▷ Solve to time T^{init} for convergence to orbit

  end for

  $\mathbf{U}_0 = \mathbf{U}(T^{init})$ ▷ New initial point

  for $0 \to N\Delta t$ **do**

    solve $\dot{\mathbf{U}}(t) = \mathbf{F}(\mathbf{U}(t)), \quad \mathbf{U}(0) = \mathbf{U}_0$ ▷ Recompute trajectory

  end for

  $LLE = 0$ ▷ Initialising LLE

  for $i = 0 \to N$ **do**

    $J = I + \Delta t D\mathbf{F}|_{\mathbf{U}(i\Delta t)}$ ▷ Calculating flow matrix

    $a_i = |J\mathbf{w}|$ ▷ Calculate stretching of perturbation

    $\mathbf{w} = \mathbf{w}/a_i$ ▷ Re-normalise perturbation

    $LLE = LLE + a_i$ ▷ Update Lyapunov exponent

  end for

  $LLE = LLE/((N+1)\Delta t)$ ▷ Time-averaging

end procedure

population dynamics given by equation (6.6) becomes

$$\begin{aligned}\mathcal{F}(Z;\eta_0,A,\Delta) &= -i\frac{(Z-1)^2}{2} + \frac{(Z+1)^2}{2}\left[-\Delta + i(\eta_0 + A)\right],\\ QA &= \frac{S}{2}(1+\sin(2\pi f t)).\end{aligned} \tag{7.7}$$

The magnitude S and frequency f were varied from 0 to 100 mA and 1 to 10 pulses/s respectively, using a mesh of 1000 uniformly distributed points in parameter space. At each parameter value, Algorithm 2 was implemented in Matlab® using random initial conditions. The driven model was integrated using `ode45` from 0 to 200 seconds, which we found sufficient for transients to settle. The LLE was then averaged from 200s to 400s, with a fixed time step $\Delta t = 0.01$s, using a random, normalised initial perturbation. Where the LLE was found to be negative, we also reported the rotation number $r = fP$, where P is the period of oscillation of the average firing rate.

The result of this computation is shown in Figure 7.1, which show a complex organisation of Arnol'd tongues within the explored parameter space. The tongues result in a range of rotation numbers, from 1 : 1 frequency ratio between slave and drive to 1 : 7, demonstrating a broad range of frequencies that the node can be entrained to using appropriate stimulation protocols.

With respect to TMS, these results can be viewed as a preliminary theoretical study of how modulation of stimulation protocols can be used to entrain oscillations to different frequency bands. Since we chose parameters *a priori*, without fitting the model to real data, there is scope to use the model to replicate entrainment observed in empirical TMS experiments such as that reported in Thut *et al.* (2011). Furthermore, it is possible the model could be extended to incorporate synaptic plasticity, arising from the synchronised firing caused by rhythmic TMS (Vernet *et al.*, 2013), using a Hebbian learning rule (Hebb, 1949), whereby entrainment encourages more synaptic connections between neurons to strengthen self-coupling. As briefly discussed in section 6.6, it is also of interest to consider neuromodulation of axonal plasticity and

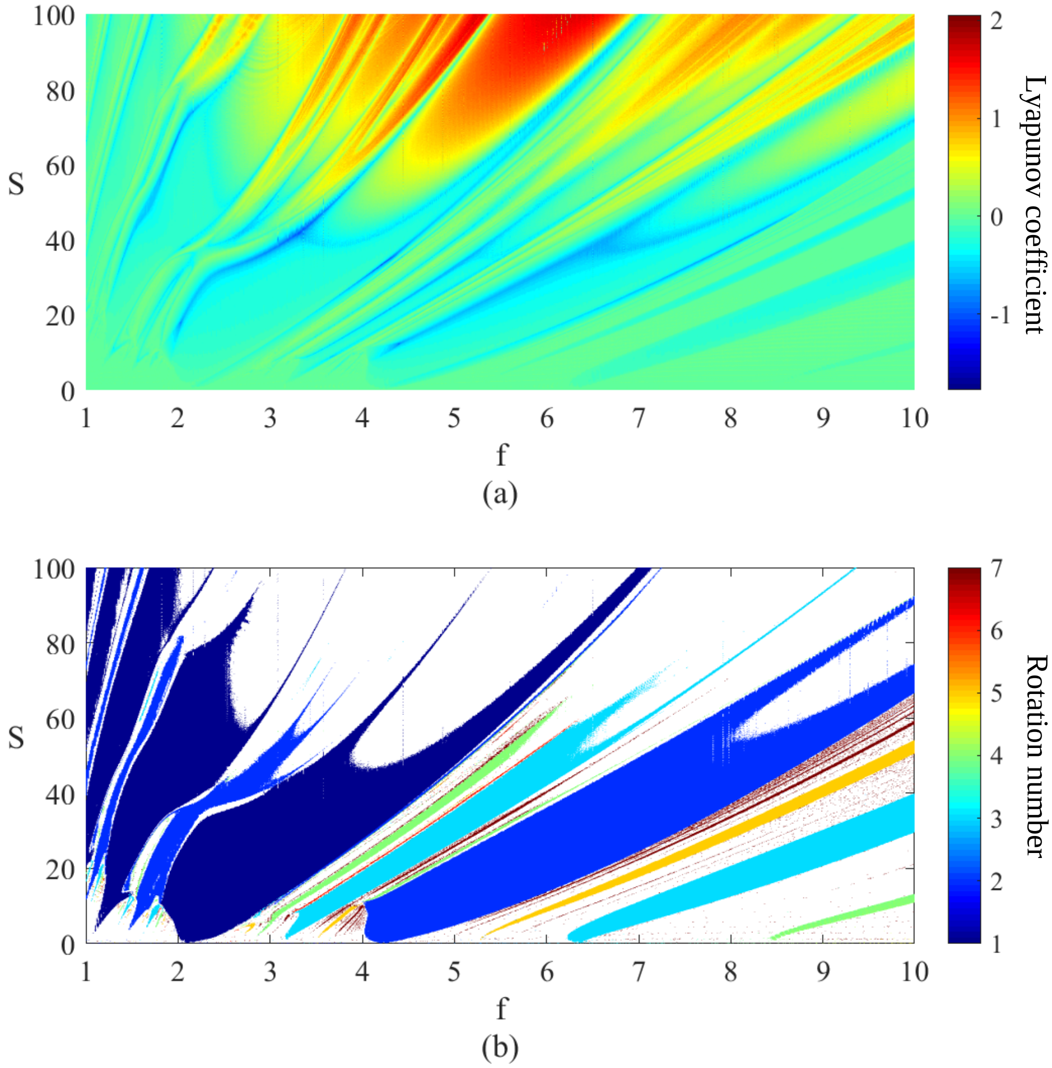

Figure 7.1: Arnol'd Tongues for a periodically driven neural mass: (a) Largest lyaponov coefficient and (b) rotation number for a single next-generation neural mass node (described in section 6.1) with dynamics governed by (6.1) and (6.5), with the addition of periodic forcing described by (7.7). Parameters used for simulations were $\alpha = 1$; $\kappa = 14$; $v_{\text{syn}} = -5$; $\Delta = 0.5$; $\eta_0 = 8$; $\alpha = 5.6$, $\mathcal{T} = 1$.

in the next section we return to the relationship between observed dynamics on a neural mass network and the conduction velocities along axons, which may be modified by promoting myelin production.

7.3 Using Delays to Excite Eigenmodes

In section 6.6, we discussed the importance of conduction delays in designing models that can replicate physiological TMS-induced effects. Variation in myelin thickness induced by TMS modifies axonal insulation, changing the speed of electrical conduction (Fields, 2008). As a means to address this, we here employ delay differential equations (DDEs), since they present a convenient mathematical framework to accommodate the modulation of axonal conduction delays by TMS. Here, we focus on a next-generation NMM with inter-regional axonal delays and, for simplicity, drop any external drive, and show how these delays can contribute to network oscillation dynamics. Moreover, the pattern of coherence between nodes' oscillations is predicted by the structural eigenmodes that are destabilised. This is important for future TMS modelling studies, since it shows promise that eigenmodes could be used as a basis for *in silico* experiments (that aim) to predict how brain states are altered by TMS-induced plasticity.

As a preliminary result, we showed in Figure 6.9 that the inclusion of delays in the NMM can be used to destabilise a steady state to achieve a pattern of oscillatory behaviour across the network. In this section we investigate the influence of delays in finer mathematical detail to help understand how the particular pattern of oscillations is related to the SC by using linear theory to deduce which eigenmodes are excited when delays are incorporated into the model.

7.3.1 Linear analysis

We described how to linearise general networks of neural masses in chapter 3, in which we calculated the eigenvalue spectra λ about a homogeneous network steady state given by the zeroes of the characteristic determinant:

$$\begin{aligned}\mathcal{E}(\lambda;p) &= \det\left[\lambda I_M - D\mathbf{F} - \mu_p(\lambda)D\mathbf{G}\right],\\ \mu_p(\lambda) &= \sum_{i=1}^{N}\sum_{j=1}^{N} w_{ij}e^{-\lambda\tau_{ij}}v_i^p v_j^p, \quad p=1,\ldots,N,\end{aligned} \tag{7.8}$$

where neural mass dynamics are governed by (3.4). $D\mathbf{F}$ and $D\mathbf{G}$ relate to the Jacobians of the model, with a $N \times N$ connectivity matrix W whose elements w_{ij} sum to 1 along rows and have an associated conduction delay given by τ_{ij}. I_M is an identity matrix of size $M \times M$ (M being the number of ODEs for each node). Recall from chapter 4 that the row-sum condition allowed us to reduce the linearisation problem to a decoupled set of N eigenvalue problems and we have an analogous set in (7.8) for a delayed system. Under the row-sum condition, matrices $D\mathbf{F}$ and $D\mathbf{G}$ are the same for all nodes $p = 1, \ldots, N$, while $\mu_p(\lambda)$ encapsulates nodal differences due to the network topology. Importantly, having decoupled spectral equations allows us to expose the role of the individual eigenmodes of the network, described by the eigenvectors $v^p \in \mathbb{R}^N$.

In practice, $\mathcal{E}(\lambda;p) = 0$ is difficult to solve since $\mu(\lambda)$ is a transcendental function, so we employ a quasi-analytic approach whereby we compute (7.8) for a range of complex λ values and find local minima of $|\mathcal{E}(\lambda;p)|$. These minima were then used as initial guesses of the eigenvalue spectra for Matlab®'s in-built `fsolve` numerical solver, which refined the eigenvalues to machine precision if a solution to $\mathcal{E}(\lambda;p) = 0$ existed in the neighbourhood of a local minimum of $|\mathcal{E}(\lambda;p)|$ (the Matlab® code for running this procedure is shown in Appendix A). In the following section we will describe the computational set-up for our specific next-generation NMM network.

7.3.2 Model setup

In order for us to use the decoupled system of spectral equations (7.8), we need to amend the delayed next-generation NMM employed in section 6.6 so it conforms to the generalised neural-mass equations (3.4). Specifically, we require synaptic coupling to be additive, rather than computing each synaptic conductance via independent ODEs. This requires encapsulating the ODEs governing synaptic conductivity (6.8) into a single equation by considering afferent inputs to be described by,

$$Q_{ext} g_a^{ext}(t) = \sum_b \kappa_{ab} f(Z_b(t - d_{ab}/c)), \tag{7.9}$$

for each node a with synaptic conductance g_a^{ext}, connected to nodes $b = 1, \ldots, N$ with strength κ_{ab}. Conduction delays are computed from the Euclidean distance between a and b, d_{ab}, divided by a conductance speed c. The coupling strengths κ_{ab} are taken from the same human 78-node SC matrix described in 4.1, which are normalised by row sum and multiplied by a universal scaling parameter ε, ($\kappa_{ab} = \varepsilon w_{ab} / \sum_b w_{ab}$). The α function is the same for all inter-node couplings, given by,

$$Q_{ext} = \left(1 + \frac{1}{\alpha_{ext}} \frac{\mathrm{d}}{\mathrm{d}t}\right)^2, \tag{7.10}$$

with a time-scale α_{ext}.

Using the new form of the next-generation network detailed above, we employ linear stability analysis of the delayed system using (7.8) in the following section.

7.3.3 Results

We first integrated the differential equation system described in section 7.3.2 without delays to find a steady state that, by inspection of the eigenvalue spectra, we identified as being close to a Hopf bifurcation. Following the quasi-analytical approach outlined in section 7.3.1, we confirmed that this stable fixed point solution could be destabilised via a Hopf bifurcation by adding delays, with conduction velocity chosen to be 9 ms^{-1}, which is a typical conduction velocity for white matter axons (Ingber and Nunez, 2011).

The linearised eigenvalue spectra was examined to determine whether there were complex conjugate pairs with positive real part, revealing which eigenmodes were destabilised. The unstable eigenmodes are of interest because they are predictive of the emergent FC (as shown in Tewarie *et al.* (2019)), which we treat later on in this section (see figures 7.3 and 7.4 and their discussion).

In Figure 7.2(a) and (b), the set of model parameters chosen result in two eigenvalue pairs crossing the imaginary axis when conduction delays are incorporated. This results in the instability of the steady state and oscillations are shown to emerge in Figure 7.2(c). Typically, dynamical systems at steady state will exhibit low-amplitude oscillations when parameters are adjusted just beyond a (super-critical) Hopf bifurcation, though the chaotic, high-amplitude waves shown here suggest that the limit cycle arising from this (sub-critical) Hopf point is in fact unstable. If this is the case, the oscillations observed here correspond to a different stable oscillatory solution and therefore the linear analysis of the initial steady state is incapable of capturing the resultant dynamics. The sub-critical bifurcation that gives rise to this result may be useful in certain neurological modelling contexts, since it could be interpreted as a network evolving from a quiescent state to a high-activity state. However, knowledge of the destabilised eigenvalues is not informative here since the linear theory breaks down in this case.

In the interests of testing whether the oscillatory dynamics resulting from an instability could be related to the network eigenstructure, the parameters were poised close to a different Hopf bifurcation we believed to be super-critical and the conduction velocity was chosen *a priori* so that only one complex conjugate pair crossed the imaginary axis, thus only destabilising a single eigenmode. An initial condition was then chosen for the delayed system, evaluated to be the steady state plus a small perturbation on g^a_{ext} for each node that was given by v^p_a, the ath element of the eigenvector associated with the unstable eigenmode. Integrating the equations with this initial condition, we found that we induced low-amplitude oscillations, as shown in figure (Figure 7.3), which

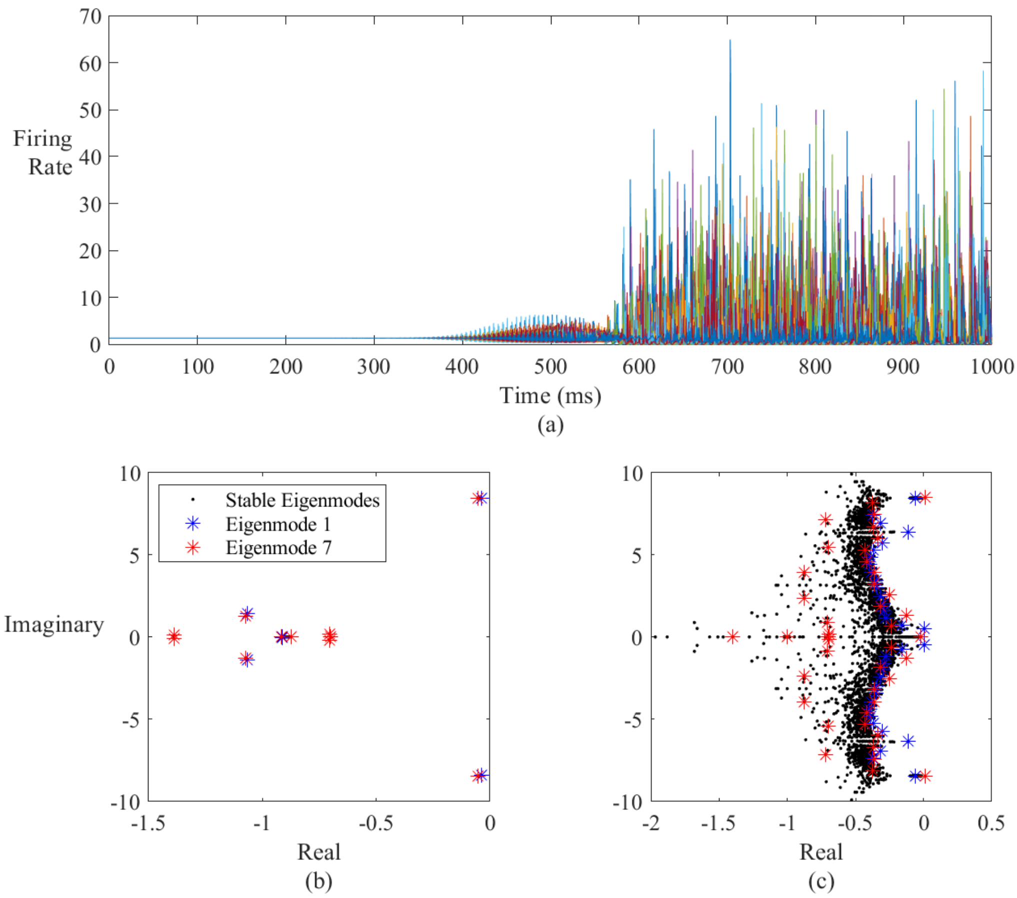

Figure 7.2: Delay-induced oscillations. Oscillations excited by the next generation NMM when conduction delays are applied. The top two panels show the spectra, calculated by solving (7.8) for the system (a) in absence and (b) in presence of delays due to a conduction velocity of 9ms^{-1}. The particular spectra for eigenmodes $p = 1, 7$ are shown highlighted in blue and red respectively. Panel (c) shows the resultant time series solution for the delayed system. The firing rate of the each node's excitatory population are plotted in different colours. Parameters used were: $\mathcal{T}_I = \mathcal{T}_E = 1$, $\alpha_{EE} = 1$, $\alpha_{EI} = 0.7$, $\alpha_{IE} = 1.4$, $\alpha_{II} = 0.7$, $\alpha_{ext} = 0.9$,$\kappa_{EE} = 1.5\pi$, $\kappa_{EI} = 2\pi$, $\kappa_{IE} = \pi$, $\kappa_{II} = 3\pi$, $v_{syn}^{EE} = 10$, $v_{syn}^{IE} = -v_{syn}^{EI} = 8$, $v_{syn}^{II} = -12$, $\Delta^E = \Delta^I = 0.5$, $\eta_0^E = 25$, $\eta_0^I = -50$, $\epsilon = 25$.

would be expected from a super-critical Hopf bifurcation.

In order to deduce whether the observed oscillatory pattern was reflective of the particular unstable eigenmode, we employed a similar methodology as used in chapter 4, wherein we showed that the eigenmode mediated the relative instantaneous phases of nodes' oscillations, which was measured as an average across the time series using the mean phase agreement (MPA) (4.7). We applied this to both the time series (which was Hilbert-transformed to extract phase via its imaginary parts) as well as the eigenvector itself. Since we posit

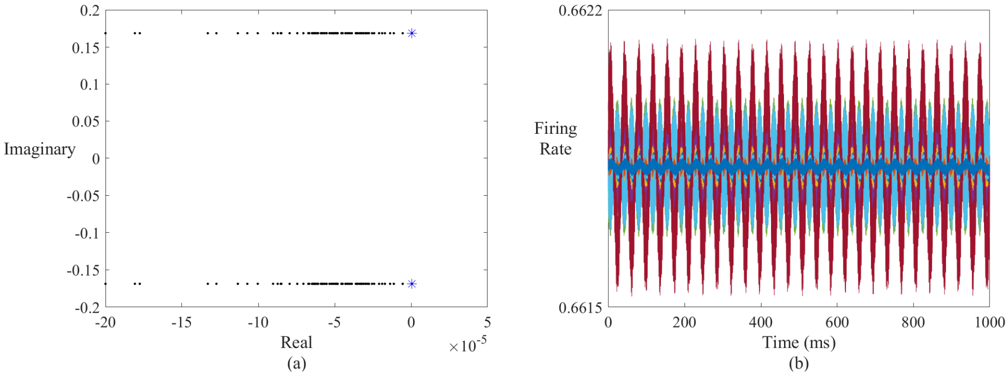

Figure 7.3: Oscillations due to instability of the 7th eigenmode. (a) Spectra showing the eigenvalue associated with the 7th eigenmode crossing the imaginary axis; (b) 1 second portion of the timeseries, taken between 19-20 seconds to give initial transients time to settle. The firing rate of the each node's excitatory population are plotted in different colours. Parameters used were: $\mathcal{T}_I = \mathcal{T}_E = 5$, $\alpha_{EE} = 0.2$, $\alpha_{EI} = 0.28$, $\alpha_{IE} = 0.14$, $\alpha_{II} = 0.08$, $\alpha_{ext} = 0.09$,$\kappa_{EE} = 2.5\pi$, $\kappa_{EI} = 10\pi$, $\kappa_{IE} = 3.5\pi$, $\kappa_{II} = 15\pi$, $v_{syn}^{EE} = v_{syn}^{IE} = -v_{syn}^{EI} = -v_{syn}^{II} = 10$, $\Delta^E = \Delta^I = 0.5$, $\eta_0^E = 20$, $\eta_0^I = -50$, $\epsilon = 17.5$.

that the phase differences between the nodes' oscillations reflect the unstable eigenmode, we used these as a basis to predict the average phase differences between nodes. Noting that the normalised eigenvector has values $v^p \in [-1, 1]$, we map these onto phases of a circle, $\theta^p \in [-\pi, \pi]$, via $\theta^p = \pi v^p$. The resulting matrices for the MPA calculations are shown in Figure 7.4. Comparing the two figures, we see that they share a similar modular structure. Also of note is that many of the nodes show a high degree of coherence, whereas a select few exhibit the opposite. This is expected, since from examining the time series in Figure 7.3(b) we see that some nodes oscillate in anti-phase with others. These nodes are exposed in Figure 7.4, whereby they show low MPA with other nodes, thereby appearing as blue bands on the matrix plot. We observe these bands on both the direct simulation and eigenvector prediction, suggesting that the anti-phase network dynamics are inherited from the unstable eigenmode. Moreover, the Jaccard similarity between the two matrices is 0.97 (to 2 s.f.), further indicating the predictive power of this analytical method to determine the dynamics of the model. Also of note is that in the linear approximation, the magnitude of the imaginary part of the unstable eigenvalue, $\mathrm{Im}(v^7)$, is related to the period of oscillation in Figure 7.3(b) via $\frac{2\pi}{\mathrm{Im}(v^7)}$; calculating these two quantities reveals this to be accurate with both $\sim 37\text{ms}^{-1}$.

This method could therefore be used as a precursor to future simulations, in order to test whether the model parameters are likely to produce patterns of coherence that correspond to the eigenmodes of interest. Indeed, such modes can reflect particular healthy/pathological states (Wang *et al.*, 2017), so this method may be used to better inform *in silico* simulations of specific brain states.

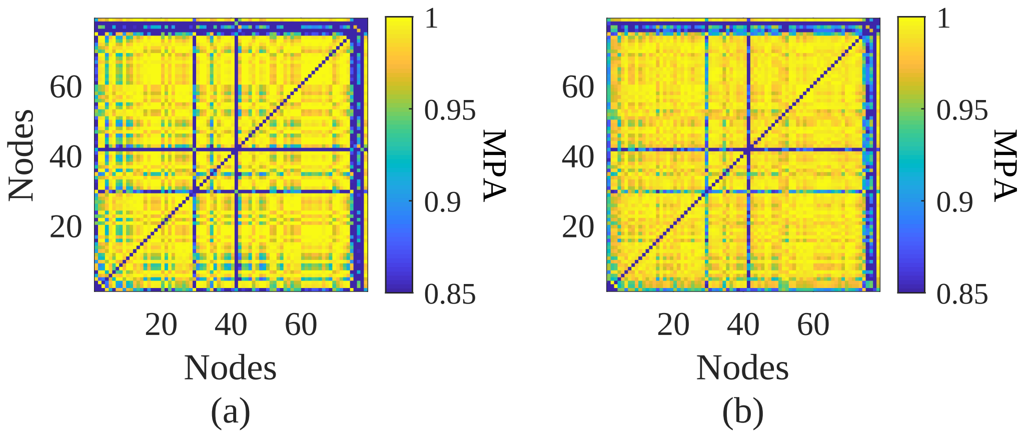

Figure 7.4: Comparison between MPA for the unstable eigenmode and direct model simulation (a) Matrix of MPA measures for a phase distribution dictated by the unstable 7th eigenmode's eigenvector; (b) MPA for the entire time series solution for the next-generation NMM, with parameters the same as in Figure 7.3. The Jaccard similarity between the matrices is 0.97 (to 2 s.f.)

7.4 Discussion

In this final technical chapter, we have presented methodologies for investigating neurological modulation using mathematical methods. In broader terms, these results also represent novel analyses of a recently developed NMM that contribute to understanding its dynamical nature, which may be useful for researchers wishing to employ the model in a variety of neurobiological applications.

In the context of our specific investigation, we have highlighted the relevance of entrainment, discussed in section 7.2, to Tourette's syndrome and we have shown that the model is able to exhibit a wide range of frequency-locked states. In future work, it would be appropriate to investigate the effects of entrainment on cortical excitability in simulations of irregular motor-related activity (Orth, 2009). An effect of particular interest would be increased beta power, which has been associated with reduced tic severity (Niccolai *et al.*, 2016). This may suppress the beta rebound effect related to motor movement, whereby decreased beta power is observed during movement followed by a spike immediately afterward. Indeed, this effect has previously been replicated using the next-generation NMM (Byrne *et al.*, 2017), suggesting that the model may be suitable to simulate pathological motor function.

In the second half of this chapter, we analysed the model at the scale of the whole brain. This revealed a highly non-trivial relationship between SC and the emergent dynamics via delay-induced excitation of eigenmodes. We did not attempt to replicate a particular TMS protocol here, but instead demonstrated the rich dynamics that can arise from the modulation of delays, which may arise from TMS-induced plasticity. Of particular interest was the prediction of certain nodes oscillating in anti-phase with most other nodes. This is significant in depression study since evidence has shown that sufferers typically do not exhibit network activity anticorrelated with the DMN, which are normally active during cognitive tasks (Chai *et al.*, 2016). Moreover, it has been shown that choosing TMS target sites that are anticorrelated with regions of interest may provide more effective treatment (Fox *et al.*, 2012). Though further investigation is required, the work here gives a preliminary indication that eigenmodes can be used in computation models to predict optimal target sites for TMS.

Next steps in this research would include varying conduction delays heterogeneously via homeostatic plastic effects, such as mentioned in section 6.6. The ability to modulate which eigenmodes are excited by the model also presents a framework to fit the model to real FC data, such as reported in Tewarie *et al.* (2019). Fitting the model to pathological brain states may not only shed light on how those states reflect the underlying structure, but also provide a basis to scrutinise the efficacy of different TMS protocols *in silico*. Moreover, eigenmodes have been shown to reflect functional resting state sub-networks (Atasoy *et al.*, 2016), so it may be feasible to simulate dynamic biologically realistic switching between brain states via excitation of different eigenmodes.

In the next and final chapter, we will summarise the main findings of this thesis and consolidate its contributions to the understanding of the function of large scale brain networks.

Chapter 8

Conclusion

To conclude, we revisit some of the main findings of this thesis and offer an evaluation of the scope for further study.

8.1 Summary of thesis

The aim of this thesis was to demonstrate a range of mathematical methods that describe the emergent behaviour of large-scale neural-mass networks. This has taken the form of a series of theoretical studies, which together represent a toolkit to interrogate brain data, especially through analysis of mathematical models.

A crucial aspect of this was to attempt to understand dynamics on the level of large-scale brain networks. After introducing some background to this topic in chapter 1 and describing some of the key mathematical concepts in chapter 3, we began the technical work of this thesis by conducting an initial computational study focused on the emergence of FC via modulation of nodal dynamics in chapter 4. We found not only that the relationship between FC and SC depended on the underlying NMM's dynamics, but that their network similarity could largely be attributed to the bifurcation structure and stability of global synchrony, both of which were independent of the SC topology (for the particular row-normalised connectivity matrix employed therein). Furthermore, we found that linear analysis of a reduced oscillator model (via a phase response function) was predictive of the behaviour of the (original) Jansen-Rit system. The main benefit of this is that it reduces the number of equations, which may greatly reduce the computational power required to simulate neural activity while still providing enough complexity to generate complex FC patterns.

In chapter 5 we focused on the nature of structure and function relations with a greater emphasis on network topology. Moreover, we developed a metric that gives a notion of how the FC contributes to the overall connectivity of the structure–function duplex, the amalgamation of both structural and functional connections, compared to the monolayer SC. This work extended the study of Crofts *et al.* (2016) for the restricted case of binary networks, to generalise this measure for use in multiplexes of several layers that have weighted connections. We showed that thresholding and binarising significantly alters the observed pattern of multiplex clustering within a parameter space for the Wilson–Cowan model. While thresholding brain networks is important to eliminate false-positive connections from data acquisition post-processing, the new metric allows researchers the freedom to interrogate multiplexes in an analogous way pre- and post-thresholding. We also offered some preliminary results to demonstrate proof of concept that such a metric could have use for empirical datasets, using frequency band-filtered MEG data as a motivating example.

Motivated by these structure–function experiments, we proceeded to use neural-mass modelling techniques for a more specialised study concerning TMS. Considering the myriad stimulation protocols that are available to clinicians, our goal here was to develop a framework for *in silico* experimentation to study the effects of stimulation on whole-brain networks. Moreover, we hoped that by doing so we could develop computational methods that may be used to elucidate the mechanisms that underly TMS's efficacy as a treatment for neurological conditions, with a particular focus on depression.

In chapter 6 we set out the model and computational setup to perform TMS simulations. Here, we were mainly interested in showing that such a model is amenable to producing changes in network dynamics, which is an essential property for simulating TMS effects. Furthermore, we showed how we could use the model to test different target sites and, by measuring various network properties of the emergent FC, described how propagation of stimuli throughout the network elicits different post-TMS network effects. We were particularly interested about how we could indirectly stimulate the insula, which is posited to be important in treating depression. This is embedded deep in the cortex, below the reach of direct TMS which only induces current close to the cortical surface. In the last part of this chapter, we noted that TMS could encourage myelination of axons and that this could potentially affect the conduction speeds between brain regions. To accommodate this, we added delays to the model and, as a motivating example, we showed that it was possible to induce oscillations by including conduction delays between coupled nodes.

In the last of the technical work, chapter 7, we took some of the ideas introduced in chapter 6 and outlined how these could be tackled from the perspective of mathematical analysis rather than through brute-force computations. We focused on two aspects of the model relevant for the study of Touettete's syndrome and TMS-induced neural plasticity; the stability of oscillations due to external forcing and linear bifurcation analysis of the network model with delays. In the former case, we revealed a rich pattern of different frequency-locked states when stimulation frequency and intensity were varied. In the latter case, we discovered that not only could we destabilise the model by including delays but the resultant dynamics were reflective of the particular unstable structural eigenmode. These findings warrant more thorough investigation and we will briefly give a critical evaluation of their significance and the next steps required to give clinical impact to the theoretical results presented in this thesis.

8.2 Discussion of further work

The results of this thesis are largely theoretical in nature and serve to illustrate mathematical methods for the analysis and simulation of brain dynamics. We note, however, that much of this work was undertaken on the presumption that such methods, while requiring further advancement, could eventually be deployed for more direct clinical applications, *i.e.* to simulate and/or analyse real brain data. We discuss some of these potential applications in this chapter, as well as suggestions to augment the relevant mathematical methods in order to establish computational tools sophisticated enough to tackle clinical challenges.

In light of our results surrounding the structure–function relationship of the brain and how this relates to the underlying dynamics, we pursued an approach whereby we used linear theory to make predictions of the emergent simulated FC in large-scale simulations. We have not, however, attempted to explain real FC data using similar techniques. One of the main limitations of our study is that we have only considered cortico-cortical interactions when, in reality, the brain's activity is mediated by a much more complex system of different types of interaction, *e.g.* the relay cells that regulate thalamo-cortical interactivity or the visual and auditory responses regulated by the midbrain. By considering only cortico-cortical connections, the model we use is limited in its ability to demonstrate how the structure of the brain acts as a substrate for its function. Indeed, many EEG/MEG experiments attempt to capture brain activity in the absence of sensory input to reveal the modes of function that emerge from cortico-cortical networks at rest (Laufs *et al.*, 2003). However, the interactions between cortical and subcortical regions are much less clear, though (as an example) it has been shown that interactions between the cortex and midbrain occur on multiple spatio-temporal scales (Stitt *et al.*, 2015), which suggests subcortical structures may have a complex role in facilitating brain function. A natural way to begin to integrate sensory information processing into the structure-function study would be to assimilate mechanisms from the thalamo-cortical system into the neural mass model. Such a model was used in Sotero *et al.* (2007) to simulate realistic EEG activity. This was further extended to replicate the slow waves and spindles associated with sleep (Cona *et al.*, 2014), as well as uncovering the dynamic response of the brain to structural neurodegeneration due to aging (Pons *et al.*, 2010). Noting the similarity of such models to that employed in chapter 4, the next step in this research could be investigating how the predictive power of the linear analyses and weakly-coupled oscillator theory techniques are altered when considering both cortico- and thalamo-cortical interactions.

In chapters 4 and 5, we briefly discussed the importance of dynamic FC in elucidating the brain's structure–function relationship. Reviewers of the paper adapted in chapter 4 (Forrester *et al.*, 2020) were interested in how the structure-function relationship evolves over time and whether our particular study could be advanced to accommodate dynamic fluctuations of FC. A primary reason for not pursuing this in the paper was that we had not fully categorised all of the phase-locked states of the network. We instead focused on near-synchronous states that were more amenable to be studied via the linear and weakly-coupled oscillator theories, as well as the most stable phase-locked states for the system under each set of values in the explored parameter space. Therefore, in simulations of the model, FC was measured over a long time to expose the most stable state (under the assumption that the noise driven system would be more inclined to the most stable phase-locked state over others). Despite these mathematical considerations, we do not wish to understate the significance of dynamic FC to current brain research (Preti *et al.*, 2017). It has been shown, for instance, that function resembles structure less over shorter timescales (Honey *et al.*, 2007; Cabral *et al.*, 2017). Moreover, the brain exhibits metastability (Friston, 1997; Deco *et al.*, 2017b), whereby the brain constantly shifts between states that are unstable rather than converging to a stable attractor. Moreover, it is thought that there exists a core of stable attracting states, comprising only a few regions, that facilitate FC transitions by engaging other specialised brain areas in order to orchestrate a particular cognitive task (Shine *et al.*, 2019). Eigenmodes of structural connectivity matrices may be a good candidate to characterise these states since they have been shown to reflect neural subnetworks of the brain (Wang *et al.*, 2017). However, though we have shown in chapter 4 that the dynamics of the Jansen-Rit network are partially reflective of the structural eigenmodes over a long timescale, it is not clear whether there is dynamic switching between states that arise from eigenmodes, or indeed if it is feasible to evaluate how many phase-locked states are stable within the network. Mathematical limitations notwithstanding, elucidating the non-trivial solutions of phase-oscillator networks is a rich area of research (Pietras and Daffertshofer, 2019) and additional analytical work may reveal the full repertoire of NMM network states, and how they may relate to dynamic FC. A more readily computable approach could be found by applying a sliding window approach, such as described in chapter 5, to treat simulated (or real) time series data. For instance, the time-varying multiplex metric described in section 5.4 could be used as a method of community detection to test the robustness of network clusters over time, potentially revealing core subnetworks.

It has also been shown that conduction delays may be integral is mediating the transient nature of brain activity (Kutchko and Fröhlich, 2013). The novelty of their work was to consider not only fast electrical conduction between cortical areas, as we considered in chapter 7, but also the slow, unmyelinated neurons that account for about half of these long-range projections. Incorporating these slower connections into their model not only caused the emergence of multistable states, but the model sporadically switched between these states in a manner that resembled real synchronisation patterns observed in brain recordings. Particularly relevant for our research is that the authors were able to use simulated transcranial alternating current stimulation to modulate the dynamic state of the model. The model itself comprised two interacting populations of neurons, rather than pursuing a large-scale simulation of mean-field cortical dynamics as we have employed throughout this thesis. It will therefore be of interest in future work to consider incorporating structural connectivity with different scales of conduction speeds in our model, both to test whether we observe a greater number of stable dynamic states in the next-generation NMM and whether we can accurately simulate FC metastability using induced noise to allow the system to explore the phase space. Some of these may relate to pathological states, since Kutchko and Fröhlich (2013) were able to simulate dynamics resembling epileptogenic activity (Schevon *et al.*, 2012). If it is possible to fit the next-generation NMM network to a pathological network state, we could use this an initial condition to prime the model for simulations of the application of therapeutic TMS to pathologically affected networks.

Finally, it is important to note how the time series data we present in this thesis relates to real physiological signals. The NMMs employed here use average firing rates as a measure of electrical activity in the brain which can be used as a suitable variable to describe EEG or MEG signals (David and Friston, 2003). However, much of the data used to describe functional connectivity on the brain comes from fMRI data. While both signals are related and can be used as biomarkers for function (Freeman *et al.*, 2009), if we wish to extend the computational methods in this thesis to fit our model to real fMRI data, it may be appropriate to transform the firing rate signals we simulate to blood-oxygen dependent (BOLD) signals that are measured using fMRI. The so-called Balloon model (Buxton *et al.*, 1998) was devised for this purpose, whereby BOLD signals are described by nonlinear functions of blood flow and neural activity. Although more recent experimental results have shown that this model does not account for all of the haemoglobic /metabolic responses due to neural stimulus Buxton (2012), moving the modelling research in this direction would be an important step in providing clinical impact, particularly in light of recent results which have used fMRI studies to investigate the therapeutic mechanisms of TMS (Hartwigsen *et al.*, 2020; Vink *et al.*, 2018).

Bibliography

Farras Abdelnour, Michael Dayan, Orrin Devinsky, Thomas Thesen, and Ashish Raj. Functional brain connectivity is predictable from anatomic network's laplacian eigen-structure. *NeuroImage*, 172:728–739, 2018.

Romesh G Abeysuriya, Jonathan Hadida, Stamatios N Sotiropoulos, Saad Jbabdi, Robert Becker, Benjamin AE Hunt, Matthew J Brookes, and Mark W Woolrich. A biophysical model of dynamic balancing of excitation and inhibition in fast oscillatory large-scale networks. *PLoS Computational Biology*, 14(2):e1006007, 2018.

Juan A Acebrón, Luis L Bonilla, Conrad J Pérez Vicente, Félix Ritort, and Renato Spigler. The Kuramoto model: A simple paradigm for synchronization phenomena. *Reviews of Modern Physics*, 77(1):137, 2005.

Saeed Ahmadizadeh, Philippa J Karoly, Dragan Nešić, David B Grayden, Mark J Cook, Daniel Soudry, and Dean R Freestone. Bifurcation analysis of two coupled jansen-rit neural mass models. *PloS One*, 13(3):e0192842, 2018.

Isabel Alkhasli, Katrin Sakreida, Felix Manuel Mottaghy, and Ferdinand Binkofski. Modulation of fronto-striatal functional connectivity using transcranial magnetic stimulation. *Frontiers in Human Neuroscience*, 13:190, 2019.

Elena A Allen, Eswar Damaraju, Sergey M Plis, Erik B Erhardt, Tom Eichele, and Vince D Calhoun. Tracking whole-brain connectivity dynamics in the resting state. *Cerebral Cortex*, 24(3):663–676, 2014.

Joel T Ariaratnam and Steven H Strogatz. Phase diagram for the winfree model of coupled nonlinear oscillators. *Physical Review Letters*, 86(19):4278, 2001.

Samuel Armstrong, Martin V Sale, and Ross Cunnington. Neural oscillations and the initiation of voluntary movement. *Frontiers in Psychology*, 9:2509, 2018.

Keyoumars Ashkan, Priya Rogers, Hagai Bergman, and Ismail Ughratdar. Insights into the mechanisms of deep brain stimulation. *Nature Reviews Neurology*, 13(9):548, 2017.

Peter Ashwin, Stephen Coombes, and Rachel Nicks. Mathematical frameworks for oscillatory network dynamics in neuroscience. *The Journal of Mathematical Neuroscience*, 6(1):2, 2016.

Selen Atasoy, Isaac Donnelly, and Joel Pearson. Human brain networks function in connectome-specific harmonic waves. *Nature Communications*, 7: 10340, 2016.

Jason A Avery, Wayne C Drevets, Scott E Moseman, Jerzy Bodurka, Joel C Barcalow, and W Kyle Simmons. Major depressive disorder is associated with abnormal interoceptive activity and functional connectivity in the insula. *Biological Psychiatry*, 76:258–266, 2014.

Claudio Babiloni, Vittorio Pizzella, Cosimo Del Gratta, Antonio Ferretti, and Gian Luca Romani. Fundamentals of electroencefalography, magnetoencefalography, and functional magnetic resonance imaging. *International Review of Neurobiology*, 86:67–80, 2009.

Danielle Smith Bassett and ED Bullmore. Small-world brain networks. *The Neuroscientist*, 12(6):512–523, 2006.

Karla Batista-García-Ramó and Caridad Ivette Fernández-Verdecia. What we know about the brain structure–function relationship. *Behavioral Sciences*, 8(4):39, 2018.

Federico Battiston, Vincenzo Nicosia, and Vito Latora. Structural measures for multiplex networks. *Physical Review E*, 89(3):032804, 2014.

Federico Battiston, Vincenzo Nicosia, Mario Chavez, and Vito Latora. Multilayer motif analysis of brain networks. *Chaos: An Interdisciplinary Journal of Nonlinear Science*, 27(4):047404, 2017.

John M Beggs and Dietmar Plenz. Neuronal avalanches in neocortical circuits. *Journal of neuroscience*, 23(35):11167–11177, 2003.

John M Beggs and Nicholas Timme. Being critical of criticality in the brain. *Frontiers in Physiology*, 3:163, 2012.

Alim Louis Benabid. Deep brain stimulation for parkinson's disease. *Current Opinion in Neurobiology*, 13(6):696–706, 2003.

Abi Berger. How does it work?: Magnetic resonance imaging. *BMJ: British Medical Journal*, 324(7328):35, 2002.

Til Ole Bergmann, Anke Karabanov, Gesa Hartwigsen, Axel Thielscher, and Hartwig Roman Siebner. Combining non-invasive transcranial brain stimulation with neuroimaging and electrophysiology: current approaches and future perspectives. *NeuroImage*, 140:4–19, 2016.

Francesco Saverio Bersani, A Minichino, Peter Gregory Enticott, L Mazzarini, N Khan, G Antonacci, RN Raccah, M Salviati, R Delle Chiaie, G Bersani, PB Fitzgerald, and M Biondi. Deep transcranial magnetic stimulation as a treatment for psychiatric disorders: a comprehensive review. *European Psychiatry*, 28(1):30–39, 2013.

Marcelo Bertalmío, Luca Calatroni, Valentina Franceschi, Benedetta Franceschiello, Alexander Gomez Villa, and Dario Prandi. Visual illusions via neural dynamics: Wilson–cowan-type models and the efficient representation principle. *Journal of Neurophysiology*, 123(5):1606–1618, 2020.

Richard F Betzel and Danielle S Bassett. Multi-scale brain networks. *NeuroImage*, 160:73–83, 2017.

Richard F Betzel, Shi Gu, John D Medaglia, Fabio Pasqualetti, and Danielle S Bassett. Optimally controlling the human connectome: the role of network topology. *Scientific Reports*, 6:30770, 2016.

Richard F Betzel, John D Medaglia, Lia Papadopoulos, Graham L Baum, Ruben Gur, Raquel Gur, David Roalf, Theodore D Satterthwaite, and Danielle S Bassett. The modular organization of human anatomical brain networks: Accounting for the cost of wiring. *Network Neuroscience*, 1(1): 42–68, 2017.

Jeff Bezanson, Alan Edelman, Stefan Karpinski, and Viral B Shah. Julia: A fresh approach to numerical computing. *SIAM review*, 59(1):65–98, 2017. URL https://doi.org/10.1137/141000671.

Christian Bick, Marc Goodfellow, Carlo R Laing, and Erik A Martens. Understanding the dynamics of biological and neural oscillator networks through exact mean-field reductions: a review. *The Journal of Mathematical Neuroscience*, 10(1):1–43, 2020.

George D Birkhoff. Proof of a recurrence theorem for strongly transitive systems. *Proceedings of the National Academy of Sciences of the United States of America*, 17(12):650, 1931.

Joschka Boedecker, Oliver Obst, Joseph T Lizier, N Michael Mayer, and Minoru Asada. Information processing in echo state networks at the edge of chaos. *Theory in Biosciences*, 131(3):205–213, 2012.

Paulo S Boggio, Felipe Fregni, Felix Bermpohl, Carlos G Mansur, Moacyr Rosa, Demetrio O Rumi, Egberto R Barbosa, Marina Odebrecht Rosa, Alvaro Pascual-Leone, Sérgio Paulo Rigonatti, Marco A Marcolin, and Maria Teresa Araujo Silva. Effect of repetitive TMS and fluoxetine on cognitive function in patients with parkinson's disease and concurrent depression. *Movement Disorders*, 20:1178–1184, 2005.

Mélanie Boly, Vincent Perlbarg, Guillaume Marrelec, Manuel Schabus, Steven Laureys, Julien Doyon, Mélanie Pélégrini-Issac, Pierre Maquet, and Habib Benali. Hierarchical clustering of brain activity during human nonrapid eye movement sleep. *Proceedings of the National Academy of Sciences*, 109(15): 5856–5861, 2012.

Elena Boto, Niall Holmes, James Leggett, Gillian Roberts, Vishal Shah, Sofie S Meyer, Leonardo Duque Muñoz, Karen J Mullinger, Tim M Tierney, Sven Bestmann, Gareth R Barnes, Richard Bowtell, and Matthew J Brookes. Moving magnetoencephalography towards real-world applications with a wearable system. *Nature*, 555(7698):657–661, 2018.

Susan M Bowyer. Coherence a measure of the brain networks: past and present. *Neuropsychiatric Electrophysiology*, 2(1):1, 2016.

Philip L Boyland. Bifurcations of circle maps: Arnol'd tongues, bistability and rotation intervals. *Communications in Mathematical Physics*, 106(3): 353–381, 1986.

Urs Braun, Sarah F Muldoon, and Danielle S Bassett. *On Human Brain Networks in Health and Disease*, pages 1–9. American Cancer Society, 2015. ISBN 9780470015902.

Michael Breakspear. Dynamic models of large-scale brain activity. *Nature Neuroscience*, 20(3):340, 2017.

Michael Breakspear, Viktor Jirsa, and Gustavo Deco. Computational models of the brain: from structure to function. *NeuroImage*, 52(3):727, 2010.

Paul C Bressloff, Jack D Cowan, Martin Golubitsky, Peter J Thomas, and Matthew C Wiener. What geometric visual hallucinations tell us about the visual cortex. *Neural Computation*, 14(3):473–491, 2002.

John-Stuart Brittain, Penny Probert-Smith, Tipu Z Aziz, and Peter Brown. Tremor suppression by rhythmic transcranial current stimulation. *Current Biology*, 23(5):436–440, 2013.

Matthew J Brookes, Prejaas K Tewarie, Benjamin AE Hunt, Sian E Robson, Lauren E Gascoyne, Elizabeth B Liddle, Peter F Liddle, and Peter G Morris. A multi-layer network approach to MEG connectivity analysis. *NeuroImage*, 132:425–438, 2016.

Javier M Buldú and Mason A Porter. Frequency-based brain networks: From a multiplex framework to a full multilayer description. *Network Neuroscience*, 2(4):418–441, 2018.

Ed Bullmore and Olaf Sporns. The economy of brain network organization. *Nature Reviews Neuroscience*, 13(5):336, 2012.

Richard B Buxton. Dynamic models of bold contrast. *NeuroImage*, 62(2): 953–961, 2012.

Richard B Buxton, Eric C Wong, and Lawrence R Frank. Dynamics of blood flow and oxygenation changes during brain activation: the balloon model. *Magnetic resonance in medicine*, 39(6):855–864, 1998.

György Buzsáki, Nikos Logothetis, and Wolf Singer. Scaling brain size, keeping timing: evolutionary preservation of brain rhythms. *Neuron*, 80(3):751–764, 2013.

Aine Byrne, Matthew J Brookes, and Stephen Coombes. A mean field model for movement induced changes in the beta rhythm. *Journal of Computational Neuroscience*, 43(2):143–158, 2017.

Áine Byrne, Reuben D O'Dea, Michael Forrester, James Ross, and Stephen Coombes. Next-generation neural mass and field modeling. *Journal of Neurophysiology*, 123(2):726–742, 2020.

Joana Cabral, Morten L Kringelbach, and Gustavo Deco. Functional connectivity dynamically evolves on multiple time-scales over a static structural connectome: Models and mechanisms. *NeuroImage*, 160:84–96, 2017.

Lihui Cai, Xile Wei, Jing Liu, Lin Zhu, Jiang Wang, Bin Deng, Haitao Yu, and Ruofan Wang. Functional integration and segregation in multiplex brain networks for alzheimer's disease. *Frontiers in Neuroscience*, 2020.

Jonathan Cannon, Michelle M McCarthy, Shane Lee, Jung Lee, Christoph Börgers, Miles A Whittington, and Nancy Kopell. Neurosystems: brain rhythms and cognitive processing. *European Journal of Neuroscience*, 39 (5):705–719, 2014.

Ugo Cerletti. Old and new information about electroshock. *American Journal of Psychiatry*, 107(2):87–94, 1950.

Xiaoqian J Chai, Dina Hirshfeld-Becker, Joseph Biederman, Mai Uchida, Oliver Doehrmann, Julia A Leonard, John Salvatore, Tara Kenworthy, Ariel Brown, Elana Kagan, Carlo de los Angeles, John DE Gabrieli, and Susan Whitfield-Gabrieli. Altered intrinsic functional brain architecture in children at familial risk of major depression. *Biological Psychiatry*, 80(11):849–858, 2016.

Hongyan Chen, Yuexiu Li, Qi Liu, Qingli Shi, Jingfang Wang, Huicong Shen, Xuzhu Chen, Jun Ma, Lin Ai, and Yu Mei Zhang. Abnormal interactions of the salience network, central executive network, and default-mode network in patients with different cognitive impairment loads caused by leukoaraiosis. *Frontiers in Neural Circuits*, 13, 2019.

Juan Chen, Jun-an Lu, Choujun Zhan, and Guanrong Chen. Laplacian spectra and synchronization processes on complex networks. In *Handbook of Optimization in Complex Networks*, pages 81–113. Springer, 2012.

Sung Wook Chung, Benjamin P Lewis, Nigel C Rogasch, Takashi Saeki, Richard H Thomson, Kate E Hoy, Neil W Bailey, and Paul B Fitzgerald. Demonstration of short-term plasticity in the dorsolateral prefrontal cortex with theta burst stimulation: A TMS-EEG study. *Clinical Neurophysiology*, 128(7):1117–1126, 2017.

Luca Cocchi, Leonardo L Gollo, Andrew Zalesky, and Michael Breakspear. Criticality in the brain: A synthesis of neurobiology, models and cognition. *Progress in Neurobiology*, 158:132–152, 2017.

Filippo Cona, M Lacanna, and Mauro Ursino. A thalamo-cortical neural mass model for the simulation of brain rhythms during sleep. *Journal of Computational Neuroscience*, 37(1):125–148, 2014.

Stephen Coombes and Aine Byrne. Next generation neural mass models. In *Nonlinear Dynamics in Computational Neuroscience*, pages 1–16. Springer, 2019.

Jonathan J Crofts, Michael Forrester, and Reuben D O'Dea. Structure-function clustering in multiplex brain networks. *EPL (Europhysics Letters)*, 116(1):18003, 2016.

Fernando Lopes da Silva. EEG and MEG: relevance to neuroscience. *Neuron*, 80(5):1112–1128, 2013.

FH Lopes Da Silva, A Hoeks, H Smits, and LH Zetterberg. Model of brain rhythmic activity. *Kybernetik*, 15(1):27–37, 1974.

Olivier David and Karl J Friston. A neural mass model for MEG/EEG:: coupling and neuronal dynamics. *NeuroImage*, 20(3):1743–1755, 2003.

Manlio De Domenico, Shuntaro Sasai, and Alex Arenas. Mapping multiplex hubs in human functional brain networks. *Frontiers in Neuroscience*, 10: 326, 2016.

Gustavo Deco, Viktor K Jirsa, Peter A Robinson, Michael Breakspear, and Karl Friston. The dynamic brain: from spiking neurons to neural masses and cortical fields. *PLoS Comput Biol*, 4(8):e1000092, 2008.

Gustavo Deco, Viktor Jirsa, Anthony R McIntosh, Olaf Sporns, and Rolf Kötter. Key role of coupling, delay, and noise in resting brain fluctuations. *Proceedings of the National Academy of Sciences*, 106(25):10302–10307, 2009.

Gustavo Deco, Viktor K Jirsa, and Anthony R McIntosh. Resting brains never rest: computational insights into potential cognitive architectures. *Trends in Neurosciences*, 36(5):268–274, 2013.

Gustavo Deco, Joana Cabral, Mark W Woolrich, Angus BA Stevner, Tim J Van Hartevelt, and Morten L Kringelbach. Single or multiple frequency generators in on-going brain activity: A mechanistic whole-brain model of empirical MEG data. *NeuroImage*, 152:538–550, 2017a.

Gustavo Deco, Morten L Kringelbach, Viktor K Jirsa, and Petra Ritter. The dynamics of resting fluctuations in the brain: metastability and its dynamical cortical core. *Scientific Reports*, 7(1):1–14, 2017b.

Gustavo Deco, Josephine Cruzat, Joana Cabral, Enzo Tagliazucchi, Helmut Laufs, Nikos K Logothetis, and Morten L Kringelbach. Awakening: Predicting external stimulation to force transitions between different brain states. *Proceedings of the National Academy of Sciences*, 116(36):18088–18097, 2019.

David Dellwo, Herbert B Keller, Bernard J Matkowsky, and Edward L Reiss. On the birth of isolas. *SIAM Journal on Applied Mathematics*, 42(5):956–963, 1982.

Rahul S Desikan, Florent Ségonne, Bruce Fischl, Brian T Quinn, Bradford C Dickerson, Deborah Blacker, Randy L Buckner, Anders M Dale, R Paul Maguire, Bradley T Hyman, Marilyn S Albert, and Ronald J Killiany. An automated labeling system for subdividing the human cerebral cortex on MRI scans into gyral based regions of interest. *NeuroImage*, 31(3):968–980, 2006.

M Desroches, M Krupa, and S Rodrigues. Inflection, canards and excitability threshold in neuronal models. *Journal of Mathematical Biology*, 67(4):989–1017, 2013.

Günther Deuschl, Carmen Schade-Brittinger, and Neurostimulation Section Krack, Paul *et al.*; German Parkinson Study Group. A randomized trial of deep-brain stimulation for parkinson's disease. *New England Journal of Medicine*, 355(9):896–908, 2006.

Serena Di Santo, Pablo Villegas, Raffaella Burioni, and Miguel A Muñoz. Landau–ginzburg theory of cortex dynamics: Scale-free avalanches emerge at the edge of synchronization. *Proceedings of the National Academy of Sciences*, 115(7):E1356–E1365, 2018.

Stavros I Dimitriadis, Mark Drakesmith, Sonya Bells, Greg D Parker, David E Linden, and Derek K Jones. Improving the reliability of network metrics in structural brain networks by integrating different network weighting strategies into a single graph. *Frontiers in Neuroscience*, 11:694, 2017.

Bard Ermentrout. *Simulating, analyzing, and animating dynamical systems: a guide to XPPAUT for researchers and students*, volume 14. SIAM, 2002.

Farnaz Zamani Esfahlani, Maxwell A Bertolero, Danielle S Bassett, and Richard F Betzel. Space-independent community and hub structure of functional brain networks. *NeuroImage*, 211:116612, 2020.

Takahiro Ezaki, Elohim Fonseca Dos Reis, Takamitsu Watanabe, Michiko Sakaki, and Naoki Masuda. Closer to critical resting-state neural dynamics in individuals with higher fluid intelligence. *Communications biology*, 3(1):1–9, 2020.

Albert J Fenoy and Richard K Simpson. Risks of common complications in deep brain stimulation surgery: management and avoidance. *Journal of Neurosurgery*, 120(1):132–139, 2014.

Miroslav Fiedler. Algebraic connectivity of graphs. *Czechoslovak Mathematical Journal*, 23(2):298–305, 1973.

R Douglas Fields. White matter in learning, cognition and psychiatric disorders. *Trends in Neurosciences*, 31(7):361–370, 2008.

Esther Florin and Sylvain Baillet. The brain's resting-state activity is shaped by synchronized cross-frequency coupling of neural oscillations. *NeuroImage*, 111:26–35, 2015.

L Fochtmann. A mechanism for the efficacy of ECT in parkinson's disease. *The Journal of ECT*, 4(4):321–327, 1988.

Michael Forrester, Jonathan J Crofts, Stamatios N Sotiropoulos, Stephen Coombes, and Reuben D O'Dea. The role of node dynamics in shaping emergent functional connectivity patterns in the brain. *Network Neuroscience*, 4 (2):467–483, 2020.

Michael D Fox, Randy L Buckner, Matthew P White, Michael D Greicius, and Alvaro Pascual-Leone. Efficacy of transcranial magnetic stimulation targets for depression is related to intrinsic functional connectivity with the subgenual cingulate. *Biological Psychiatry*, 72:595–603, 2012.

Walter J Freeman, Seppo P Ahlfors, and Vinod Menon. Combining fMRI with EEG and MEG in order to relate patterns of brain activity to cognition. *International Journal of Psychophysiology*, 73(1):43–52, 2009.

WJ Freeman. Models of the dynamics of neural populations. *Electroencephalography and clinical neurophysiology. Supplement*, (34):9–18, 1978.

FreeSurfer. Cortical parcellation estimated by intrinsic functional connectivity. https://surfer.nmr.mgh.harvard.edu/fswiki/CorticalParcellation_Yeo2011. Accessed: 2020-02-18.

Catarina Freitas, Faranak Farzan, and Alvaro Pascual-Leone. Assessing brain plasticity across the lifespan with transcranial magnetic stimulation: why, how, and what is the ultimate goal? *Frontiers in Neuroscience*, 7:42, 2013.

Karl J Friston. Transients, metastability, and neuronal dynamics. *NeuroImage*, 5(2):164–171, 1997.

Makoto Fukushima, Richard F Betzel, Ye He, Martijn P van den Heuvel, Xi-Nian Zuo, and Olaf Sporns. Structure–function relationships during segregated and integrated network states of human brain functional connectivity. *Brain Structure and Function*, 223(3):1091–1106, 2018.

PK Fung and PA Robinson. Neural field theory of synaptic metaplasticity with applications to theta burst stimulation. *Journal of Theoretical Biology*, 340:164–176, 2014.

Nicholas Furl, Richard Coppola, Bruno B Averbeck, and Daniel R Weinberger. Cross-frequency power coupling between hierarchically organized face-selective areas. *Cerebral Cortex*, 24(9):2409–2420, 2014.

Mark S George, Eric M Wassermann, Wendol A Williams, Ann Callahan, Terence A Ketter, Peter Basser, Mark Hallett, and Robert M Post. Daily repetitive transcranial magnetic stimulation (rTMS) improves mood in depression. *Neuroreport: An International Journal for the Rapid Communication of Research in Neuroscience*, 1995.

Mark S George, Ziad Nahas, Monica Molloy, Andrew M Speer, Nicholas C Oliver, Xing-Bao Li, George W Arana, S Craig Risch, and James C Ballenger. A controlled trial of daily left prefrontal cortex TMS for treating depression. *Biological Psychiatry*, 48:962–970, 2000.

Charles R Gerfen, Michael N Economo, and Jayaram Chandrashekar. Long distance projections of cortical pyramidal neurons. *Journal of Neuroscience Research*, 96(9):1467–1475, 2018.

Matthew F Glasser, Stamatios N Sotiropoulos, J Anthony Wilson, Timothy S Coalson, Bruce Fischl, Jesper L Andersson, Junqian Xu, Saad Jbabdi, Matthew Webster, Jonathan R Polimeni, David C Van Essen, and Mark Jenkinson. The minimal preprocessing pipelines for the human connectome project. *NeuroImage*, 80:105–124, 2013.

Gary H Glover. Overview of functional magnetic resonance imaging. *Neurosurgery Clinics*, 22(2):133–139, 2011.

Mitchell R Goldsworthy, Julia B Pitcher, and Michael C Ridding. A comparison of two different continuous theta burst stimulation paradigms applied to the human primary motor cortex. *Clinical Neurophysiology*, 123(11):2256–2263, 2012.

Joan Gomez. Subjective side-effects of ECT. *The British Journal of Psychiatry*, 127(6):609–611, 1975.

Javier Gonzalez-Castillo and Peter A Bandettini. Task-based dynamic functional connectivity: Recent findings and open questions. *NeuroImage*, 180: 526–533, 2018.

M Goodfellow, Christian Rummel, Eugenio Abela, MP Richardson, K Schindler, and JR Terry. Estimation of brain network ictogenicity predicts outcome from epilepsy surgery. *Scientific Reports*, 6:29215, 2016.

Marc Goodfellow, Kaspar Schindler, and Gerold Baier. Intermittent spike–wave dynamics in a heterogeneous, spatially extended neural mass model. *NeuroImage*, 55(3):920–932, 2011.

Nia Goulden, Aygul Khusnulina, Nicholas J Davis, Robert M Bracewell, Arun L Bokde, Jonathan P McNulty, and Paul G Mullins. The salience network is responsible for switching between the default mode network and the central executive network: replication from dcm. *NeuroImage*, 99:180–190, 2014.

François Grimbert and Olivier Faugeras. Bifurcation analysis of jansen's neural mass model. *Neural Computation*, 18(12):3052–3068, 2006.

RW Guillery and S Murray Sherman. Thalamic relay functions and their role in corticocortical communication: generalizations from the visual system. *Neuron*, 33(2):163–175, 2002.

Patric Hagmann, Leila Cammoun, Xavier Gigandet, Reto Meuli, Christopher J Honey, Van J Wedeen, and Olaf Sporns. Mapping the structural core of human cerebral cortex. *PLoS Biology*, 6(7), 2008.

Emma L Hall, Siân E Robson, Peter G Morris, and Matthew J Brookes. The relationship between MEG and fMRI. *NeuroImage*, 102:80–91, 2014.

Mark Hallett. Transcranial magnetic stimulation and the human brain. *Nature*, 406(6792):147–150, 2000.

Enrique CA Hansen, Demian Battaglia, Andreas Spiegler, Gustavo Deco, and Viktor K Jirsa. Functional connectivity dynamics: modeling the switching behavior of the resting state. *NeuroImage*, 105:525–535, 2015.

Gesa Hartwigsen, Tanja Kassuba, and Hartwig R Siebner. Combining transcranial magnetic stimulation with (f)MRI. In *fMRI*, pages 157–174. Springer, 2020.

Jeff Hawkins, Subutai Ahmad, and Yuwei Cui. A theory of how columns in the neocortex enable learning the structure of the world. *Frontiers in Neural Circuits*, 11:81, 2017.

Donald Olding Hebb. *The organization of behavior: a neuropsychological theory*. J. Wiley; Chapman & Hall, 1949.

Peter J Hellyer, Barbara Jachs, Claudia Clopath, and Robert Leech. Local inhibitory plasticity tunes macroscopic brain dynamics and allows the emergence of functional brain networks. *NeuroImage*, 124:85–95, 2016.

Moisés Hernández, Ginés D Guerrero, José M Cecilia, José M García, Alberto Inuggi, Saad Jbabdi, Timothy EJ Behrens, and Stamatios N Sotiropoulos. Accelerating fibre orientation estimation from diffusion weighted magnetic resonance imaging using GPUs. *PLoS One*, 8(4), 2013.

Jaroslav Hlinka and Stephen Coombes. Using computational models to relate structural and functional brain connectivity. *European Journal of Neuroscience*, 36(2):2137–2145, 2012.

Alan L Hodgkin and Andrew F Huxley. A quantitative description of membrane current and its application to conduction and excitation in nerve. *The Journal of Physiology*, 117(4):500–544, 1952.

Christopher J Honey, Rolf Kötter, Michael Breakspear, and Olaf Sporns. Network structure of cerebral cortex shapes functional connectivity on multiple time scales. *Proceedings of the National Academy of Sciences*, 104(24): 10240–10245, 2007.

CJ Honey, O Sporns, Leila Cammoun, Xavier Gigandet, Jean-Philippe Thiran, Reto Meuli, and Patric Hagmann. Predicting human resting-state functional connectivity from structural connectivity. *Proceedings of the National Academy of Sciences*, 106(6):2035–2040, 2009.

John J Hopfield. Neural networks and physical systems with emergent collective computational abilities. *Proceedings of the National Academy of Sciences*, 79(8):2554–2558, 1982.

Andreas Horn. The impact of modern-day neuroimaging on the field of deep brain stimulation. *Current Opinion in Neurology*, 32(4):511–520, 2019.

Dorothea I Horn, Chunshui Yu, Johann Steiner, Julia Buchmann, Joern Kaufmann, Annemarie Osoba, Ulf Eckert, Kathrin Zierhut, Kolja Schiltz, Huiguang He, B Biswal, B Bogerts, and M Walter. Glutamatergic and resting-state functional connectivity correlates of severity in major depression–the role of pregenual anterior cingulate cortex and anterior insula. *Frontiers in Systems Neuroscience*, 4:33, 2010.

R Matthew Hutchison, Thilo Womelsdorf, Elena A Allen, Peter A Bandettini, Vince D Calhoun, Maurizio Corbetta, Stefania Della Penna, Jeff H Duyn, Gary H Glover, Javier Gonzalez-Castillo, Daniel A Handwerker, Shella Keilholz, Vesa Kiviniemi, David A Leopold, Francesco de Pasquale, Olaf Sporns, Martin Walter, and Catie Chang. Dynamic functional connectivity: promise, issues, and interpretations. *NeuroImage*, 80:360–378, 2013a.

R Matthew Hutchison, Thilo Womelsdorf, Joseph S Gati, Stefan Everling, and Ravi S Menon. Resting-state networks show dynamic functional connectivity in awake humans and anesthetized macaques. *Human Brain Mapping*, 34 (9):2154–2177, 2013b.

Kai Hwang, Maxwell A Bertolero, William B Liu, and Mark D'esposito. The human thalamus is an integrative hub for functional brain networks. *Journal of Neuroscience*, 37(23):5594–5607, 2017.

Risto J Ilmoniemi and Dubravko Kičić. Methodology for combined TMS and EEG. *Brain Topography*, 22(4):233, 2010.

Lester Ingber and Paul L Nunez. Neocortical dynamics at multiple scales: EEG standing waves, statistical mechanics, and physical analogs. *Mathematical Biosciences*, 229(2):160–173, 2011.

Sarina J Iwabuchi, Felix Raschke, Dorothee P Auer, Peter F Liddle, Sudheer T Lankappa, and Lena Palaniyappan. Targeted transcranial theta-burst stimulation alters fronto-insular network and prefrontal GABA. *NeuroImage*, 146:395–403, 2017.

Paul Jaccard. The distribution of the flora in the alpine zone. 1. *New phytologist*, 11(2):37–50, 1912.

Ben H Jansen and Vincent G Rit. Electroencephalogram and visual evoked potential generation in a mathematical model of coupled cortical columns. *Biological Cybernetics*, 73(4):357–366, 1995.

Saad Jbabdi, Stamatios N Sotiropoulos, Alexander M Savio, Manuel Graña, and Timothy EJ Behrens. Model-based analysis of multishell diffusion mr data for tractography: How to get over fitting problems. *Magnetic Resonance in Medicine*, 68(6):1846–1855, 2012.

Charles H Kellner, Robert M Greenberg, James W Murrough, Ethan O Bryson, Mimi C Briggs, and Rosa M Pasculli. ECT in treatment-resistant depression. *American Journal of Psychiatry*, 169(12):1238–1244, 2012.

Mikko Kivelä, Alex Arenas, Marc Barthelemy, James P Gleeson, Yamir Moreno, and Mason A Porter. Multilayer networks. *Journal of Complex Networks*, 2(3):203–271, 2014.

Andreas Knoblauch and Friedrich T Sommer. Synaptic plasticity, conduction delays, and inter-areal phase relations of spike activity in a model of reciprocally connected areas. *Neurocomputing*, 52:301–306, 2003.

Hans Martin Kolbinger, Gereon Höflich, Andreas Hufnagel, Hans-Jürgen Müller, and Siegfried Kasper. Transcranial magnetic stimulation (TMS) in the treatment of major depression — a pilot study. *Human Psychopharmacology: Clinical and Experimental*, 10:305–310, 1995.

James M Krueger, David M Rector, Sandip Roy, Hans PA Van Dongen, Gregory Belenky, and Jaak Panksepp. Sleep as a fundamental property of neuronal assemblies. *Nature Reviews Neuroscience*, 9(12):910–919, 2008.

Levin Kuhlmann, David B Grayden, Fabrice Wendling, and Steven J Schiff. The role of multiple-scale modelling of epilepsy in seizure forecasting. *Journal of Clinical Neurophysiology*, 32(3):220, 2015.

Yoshiki Kuramoto. Self-entrainment of a population of coupled non-linear oscillators. In *International symposium on mathematical problems in theoretical physics*, pages 420–422. Springer, 1975.

Katrina M Kutchko and Flavio Fröhlich. Emergence of metastable state dynamics in interconnected cortical networks with propagation delays. *PLoS Computational Biology*, 9(10):e1003304, 2013.

Ho Jang Kwon, Won Seok Lim, Myung Ho Lim, Seong Jae Lee, Jung Keun Hyun, Jeong-Ho Chae, and Ki Chung Paik. 1-hz low frequency repetitive transcranial magnetic stimulation in children with tourette's syndrome. *Neuroscience Letters*, 492(1):1–4, 2011.

M J Lan, B T Chhetry, C Liston, J J Mann, and M Dubin. Transcranial magnetic stimulation of left dorsolateral prefrontal cortex induces brain morphological changes in regions associated with a treatment resistant major depressive episode: An exploratory analysis. *Brain Stimulation*, 9:577–583, 2016.

Nicolas Lang, Hartwig R Siebner, Zoltan Chadaide, Klara Boros, Michael A Nitsche, John C Rothwell, Walter Paulus, and Andrea Antal. Bidirectional modulation of primary visual cortex excitability: a combined tDCS and rTMS study. *Investigative Ophthalmology & Visual Science*, 48:5782–5787, 2007.

Louis Lapique. Recherches quantitatives sur l'excitation electrique des nerfs traitee comme une polarization. *Journal of Physiology and Pathololgy*, 9: 620–635, 1907.

Linda J Larson-Prior, Robert Oostenveld, Stefania Della Penna, G Michalareas, F Prior, Abbas Babajani-Feremi, J-M Schoffelen, Laura Marzetti, Francesco de Pasquale, F Di Pompeo, J Stout, M Woolrich, Q Luo, R Bucholz, P Fries, V Pizzella, GL Romani, M Corbetta, and AZ Snyder. Adding dynamics to the human connectome project with MEG. *NeuroImage*, 80: 190–201, 2013.

Peter E Latham, BJ Richmond, PG Nelson, and S Nirenberg. Intrinsic dynamics in neuronal networks. I. theory. *Journal of Neurophysiology*, 83(2): 808–827, 2000.

Helmut Laufs, K Krakow, P Sterzer, E Eger, A Beyerle, A Salek-Haddadi, and A Kleinschmidt. Electroencephalographic signatures of attentional and cognitive default modes in spontaneous brain activity fluctuations at rest. *Proceedings of the National Academy of Sciences*, 100(19):11053–11058, 2003.

Kai Le, Ling Liu, Manli Sun, Ling Hu, and Nong Xiao. Transcranial magnetic stimulation at 1 hertz improves clinical symptoms in children with tourette syndrome for at least 6 months. *Journal of Clinical Neuroscience*, 20(2): 257–262, 2013.

Seung-Hwan Lee, Won Kim, Young-Cho Chung, Kyung-Hee Jung, Won-Myong Bahk, Tae-Yun Jun, Kwang-Soo Kim, Mark S George, and Jeong-Ho Chae. A double blind study showing that two weeks of daily repetitive TMS over the left or right temporoparietal cortex reduces symptoms in patients with schizophrenia who are having treatment-refractory auditory hallucinations. *Neuroscience Letters*, 376:177–181, 2005.

Klaus Lehnertz, Stephan Bialonski, Marie-Therese Horstmann, Dieter Krug, Alexander Rothkegel, Matthäus Staniek, and Tobias Wagner. Synchronization phenomena in human epileptic brain networks. *Journal of Neuroscience Methods*, 183(1):42–48, 2009.

Tristram A Lett, Aristotle N Voineskos, James L Kennedy, Brian Levine, and Zafiris J Daskalakis. Treating working memory deficits in schizophrenia: a review of the neurobiology. *Biological Psychiatry*, 75:361–370, 2014.

Xuhong Liao, Athanasios V Vasilakos, and Yong He. Small-world human brain networks: perspectives and challenges. *Neuroscience & Biobehavioral Reviews*, 77:286–300, 2017.

Zhifen Liu, Cheng Xu, Yong Xu, Yanfang Wang, Bing Zhao, Yating Lv, Xiaohua Cao, Kerang Zhang, and Chongxi Du. Decreased regional homogeneity in insula and cerebellum: a resting-state fMRI study in patients with major depression and subjects at high risk for major depression. *Psychiatry Research: Neuroimaging*, 182:211–215, 2010.

Colleen K Loo and Philip B Mitchell. A review of the efficacy of transcranial magnetic stimulation (TMS) treatment for depression, and current and future strategies to optimize efficacy. *Journal of Affective Disorders*, 88: 255–267, 2005.

Mark J Lowe, Ken E Sakaie, Erik B Beall, Vince D Calhoun, David A Bridwell, Mikail Rubinov, and Stephen M Rao. Modern methods for interrogating the human connectome. *Journal of the International Neuropsychological Society*, 22(2):105–119, 2016.

Mojtaba Madadi Asl, Alireza Valizadeh, and Peter A Tass. Dendritic and axonal propagation delays may shape neuronal networks with plastic synapses. *Frontiers in Physiology*, 9:1849, 2018.

Barbara Morera Maiquez, Hilmar P Sigurdsson, Katherine Dyke, Eleri Clarke, Polly McGrath, Matthew Pasche, Anupriya Rajendran, Georgina M Jackson, and Stephen R Jackson. Entraining movement-related brain oscillations to suppress tics in tourette syndrome. *Current Biology*, 2020.

Barry Maletzky, Bentson McFarland, and Alex Burt. Refractory obsessive compulsive disorder and ECT. *Convulsive therapy*, 1994.

Antonio Mantovani, James F Leckman, Heidi Grantz, Robert A King, Alexandra L Sporn, and Sarah H Lisanby. Repetitive transcranial magnetic stimulation of the supplementary motor area in the treatment of tourette syndrome: report of two cases. *Clinical Neurophysiology*, 10(118):2314–2315, 2007.

F Marten, S Rodrigues, O Benjamin, M P Richardson, and J R Terry. Onset of polyspike complexes in a mean-field model of human electroencephalography and its application to absence epilepsy. *Philosophical Transactions of the Royal Society of London A*, 367:1145–1161, 2009.

Sergei Maslov and Kim Sneppen. Specificity and stability in topology of protein networks. *Science*, 296(5569):910–913, 2002.

Helen S Mayberg. Limbic-cortical dysregulation: a proposed model of depression. *The Journal of Neuropsychiatry and Clinical Neurosciences*, 9:471–481, 1997.

Shawn M McClintock, Irving M Reti, Linda L Carpenter, William M McDonald, Marc Dubin, Stephan F Taylor, Ian A Cook, John O'Reardon, Mustafa M Husain, Christopher Wall, Andrew D Krystal, Shirlene M Sampson, Oscar Morales, Brent G Nelson, Vassilios Latoussakis, Mark S George, and Sarah H Lisanby. Consensus recommendations for the clinical application of repetitive transcranial magnetic stimulation (rTMS) in the treatment of depression. *The Journal of Clinical Psychiatry*, 79(1), 2018.

Lisa A Mellman and Jack M Gorman. Successful treatment of obsessive-compulsive disorder with ECT. *The American Journal of Psychiatry*, 1984.

Vinod Menon. Large-scale brain networks and psychopathology: a unifying triple network model. *Trends in Cognitive Sciences*, 15(10):483–506, 2011.

Vinod Menon and Lucina Q Uddin. Saliency, switching, attention and control: a network model of insula function. *Brain Structure and Function*, 214(5-6): 655–667, 2010.

Arnaud Messé, David Rudrauf, Habib Benali, and Guillaume Marrelec. Relating structure and function in the human brain: relative contributions of anatomy, stationary dynamics, and non-stationarities. *PLoS Computational Biology*, 10(3):e1003530, 2014.

Arnaud Messé, Marc-Thorsten Hütt, Peter König, and Claus C Hilgetag. A closer look at the apparent correlation of structural and functional connectivity in excitable neural networks. *Scientific Reports*, 5:7870, 2015.

David Meunier, Renaud Lambiotte, and Edward T Bullmore. Modular and hierarchically modular organization of brain networks. *Frontiers in Neuroscience*, 4:200, 2010.

Microsoft 3D Library. Paint 3d. https://www.microsoft.com/en-gb/p/paint-3d/9nblggh5fv99. Accessed: 2020-04-28.

Richard Miles, Katalin Tóth, Attila I Gulyás, Norbert Hájos, and Tamas F Freund. Differences between somatic and dendritic inhibition in the hippocampus. *Neuron*, 16(4):815–823, 1996.

Friederike Moeller, Hartwig R Siebner, Stephan Wolff, Hiltrud Muhle, Oliver Granert, Olav Jansen, Ulrich Stephani, and Michael Siniatchkin. Simultaneous EEG-fMRI in drug-naive children with newly diagnosed absence epilepsy. *Epilepsia*, 49(9):1510–1519, 2008.

Florian Mormann, Klaus Lehnertz, Peter David, and Christian E Elger. Mean phase coherence as a measure for phase synchronization and its application to the EEG of epilepsy patients. *Physica D*, 144(3-4):358–369, 2000.

Florian Mormann, Thomas Kreuz, Ralph G Andrzejak, Peter David, Klaus Lehnertz, and Christian E Elger. Epileptic seizures are preceded by a decrease in synchronization. *Epilepsy Research*, 53(3):173–185, 2003.

Vernon B Mountcastle. Modality and topographic properties of single neurons of cat's somatic sensory cortex. *Journal of Neurophysiology*, 20(4):408–434, 1957.

Peter J Mucha, Thomas Richardson, Kevin Macon, Mason A Porter, and Jukka-Pekka Onnela. Community structure in time-dependent, multiscale, and multiplex networks. *Science*, 328(5980):876–878, 2010.

Sophia Mueller, Danhong Wang, Michael D Fox, BT Thomas Yeo, Jorge Sepulcre, Mert R Sabuncu, Rebecca Shafee, Jie Lu, and Hesheng Liu. Individual variability in functional connectivity architecture of the human brain. *Neuron*, 77(3):586–595, 2013.

J Florian M Müller, Yuriy Orekhov, Yali Liu, and Ulf Ziemann. Homeostatic plasticity in human motor cortex demonstrated by two consecutive sessions of paired associative stimulation. *European Journal of Neuroscience*, 25(11):3461–3468, 2007.

Umer Najib, Shahid Bashir, Dylan Edwards, Alexander Rotenberg, and Alvaro Pascual-Leone. Transcranial brain stimulation: clinical applications and future directions. *Neurosurgery Clinics*, 22(2):233–251, 2011.

Theoden I Netoff and Steven J Schiff. Decreased neuronal synchronization during experimental seizures. *Journal of Neuroscience*, 22(16):7297–7307, 2002.

Mark Newman. *Networks*. Oxford university press, 2018.

Mark EJ Newman. *Mathematics of Networks*, pages 1–8. Palgrave Macmillan UK, London, 2016.

Valentina Niccolai, Hanneke van Dijk, Stephanie Franzkowiak, Jennifer Finis, Martin Südmeyer, Melanie Jonas, Götz Thomalla, Hartwig Roman Siebner, Kirsten Müller-Vahl, Alexander Münchau, Alfons Schnitzler, and Katja Biermann-Ruben. Increased beta rhythm as an indicator of inhibitory mechanisms in tourette syndrome. *Movement Disorders*, 31(3):384–392, 2016.

Wilten Nicola, Peter John Hellyer, Sue Ann Campbell, and Claudia Clopath. Chaos in homeostatically regulated neural systems. *Chaos: An Interdisciplinary Journal of Nonlinear Science*, 28(8):083104, 2018.

Y Noda, W K Silverstein, M S Barr, F Vila-Rodriguez, J Downar, T K Rajji, P B Fitzgerald, B H Mulsant, S N Vigod, Z J Daskalakis, and D M Blumberger. Neurobiological mechanisms of repetitive transcranial magnetic stimulation of the dorsolateral prefrontal cortex in depression: A systematic review. *Psychological Medicine*, 45:3411–3432, 2015.

Paul L Nunez and Ramesh Srinivasan. *Electric fields of the brain: the neurophysics of EEG*. Oxford University Press, USA, 2006.

Y Okazaki, Y Nakagawa, T Hanakawa, Y Mizuno, and K Kitajo. P119 repetitive TMS can modulate local phase and global phase synchronization of human brain activity. *Clinical Neurophysiology*, 128(3):e73, 2017.

Stuart Oldham and Alex Fornito. The development of brain network hubs. *Developmental Cognitive Neuroscience*, 2018.

Tore Opsahl and Pietro Panzarasa. Clustering in weighted networks. *Social networks*, 31(2):155–163, 2009.

Tore Opsahl, Vittoria Colizza, Pietro Panzarasa, and José J Ramasco. Prominence and control: the weighted rich-club effect. *Physical Review Letters*, 101(16):168702, 2008.

Michael Orth. Transcranial magnetic stimulation in gilles de la tourette syndrome. *Journal of Psychosomatic Research*, 67(6):591–598, 2009.

Jill L Ostrem and Philip A Starr. Treatment of dystonia with deep brain stimulation. *Neurotherapeutics*, 5(2):320–330, 2008.

Edward Ott and Thomas M Antonsen. Low dimensional behavior of large systems of globally coupled oscillators. *Chaos: An Interdisciplinary Journal of Nonlinear Science*, 18(3):037113, 2008.

Andreas Otto, Günter Radons, Dániel Bachrathy, and Gábor Orosz. Synchronization in networks with heterogeneous coupling delays. *Physical Review E*, 97(1):012311, 2018.

George C O'Neill, Prejaas K Tewarie, Giles L Colclough, Lauren E Gascoyne, Benjamin AE Hunt, Peter G Morris, Mark W Woolrich, and Matthew J Brookes. Measurement of dynamic task related functional networks using MEG. *NeuroImage*, 146:667–678, 2017.

Daniel Pagnin, Valéria de Queiroz, Stefano Pini, and Giovanni Battista Cassano. Efficacy of ECT in depression: a meta-analytic review. *Focus*, 6(1): 155–162, 2008.

Sinisa Pajevic, Peter J Basser, and R Douglas Fields. Role of myelin plasticity in oscillations and synchrony of neuronal activity. *Neuroscience*, 276:135–147, 2014.

Agostina Palmigiano, Theo Geisel, Fred Wolf, and Demian Battaglia. Flexible information routing by transient synchrony. *Nature neuroscience*, 20(7): 1014, 2017.

Hae-Jeong Park and Karl Friston. Structural and functional brain networks: from connections to cognition. *Science*, 342(6158):1238411, 2013.

Joel S Perlmutter and Jonathan W Mink. Deep brain stimulation. *Annual Review of Neuroscience*, 29:229–257, 2006.

Steven E Petersen and Olaf Sporns. Brain networks and cognitive architectures. *Neuron*, 88(1):207–219, 2015.

George Petkov, Marc Goodfellow, Mark P Richardson, and John R Terry. A critical role for network structure in seizure onset: a computational modeling approach. *Frontiers in neurology*, 5:261, 2014.

Bastian Pietras and Andreas Daffertshofer. Network dynamics of coupled oscillators and phase reduction techniques. *Physics Reports*, 819:1–105, 2019.

Arkady Pikovsky and Antonio Politi. *Lyapunov exponents: a tool to explore complex dynamics*. Cambridge University Press, 2016.

Arkady Pikovsky, Jurgen Kurths, Michael Rosenblum, and Jürgen Kurths. *Synchronization: a universal concept in nonlinear sciences*, volume 12. Cambridge university press, 2003.

Adrián Ponce-Alvarez, Gustavo Deco, Patric Hagmann, Gian Luca Romani, Dante Mantini, and Maurizio Corbetta. Resting-state temporal synchronization networks emerge from connectivity topology and heterogeneity. *PLoS Computational Biology*, 11(2):e1004100, 2015.

AJ Pons, Jose L Cantero, Mercedes Atienza, and Jordi Garcia-Ojalvo. Relating structural and functional anomalous connectivity in the aging brain via neural mass modeling. *NeuroImage*, 52(3):848–861, 2010.

D Popeo and CH Kellner. ECT for parkinson's disease. *Medical hypotheses*, 73(4):468, 2009.

Maria Giulia Preti, Thomas AW Bolton, and Dimitri Van De Ville. The dynamic functional connectome: State-of-the-art and perspectives. *NeuroImage*, 160:41–54, 2017.

Sonia Pujol. Imaging white matter anatomy for brain tumor surgery. In *Image-Guided Neurosurgery*, pages 91–121. Elsevier, 2015.

Deepti Putcha, Robert S Ross, Alice Cronin-Golomb, Amy C Janes, and Chantal E Stern. Salience and default mode network coupling predicts cognition in aging and parkinson's disease. *Journal of the International Neuropsychological Society*, 22(2):205–215, 2016.

Amit Ray and Susan M Bowyer. Clinical applications of magnetoencephalography in epilepsy. *Annals of Indian Academy of Neurology*, 13(1):14, 2010.

Scott Rich, Michal Zochowski, and Victoria Booth. Effects of neuromodulation on excitatory–inhibitory neural network dynamics depend on network connectivity structure. *Journal of Nonlinear Science*, pages 1–24, 2018.

MC Ridding and U Ziemann. Determinants of the induction of cortical plasticity by non-invasive brain stimulation in healthy subjects. *The Journal of Physiology*, 588(13):2291–2304, 2010.

Serafim Rodrigues, David Barton, Frank Marten, Moses Kibuuka, Gonzalo Alarcon, Mark P Richardson, and John R Terry. A method for detecting false bifurcations in dynamical systems: application to neural-field models. *Biological Cybernetics*, 102(2):145–154, 2010.

H Rothkegel, M Sommer, W Paulus, and N Lang. Impact of pulse duration in single pulse TMS. *Clinical neurophysiology*, 121(11):1915–1921, 2010.

M Rubinov and O Sporns. Complex network measures of brain connectivity: Uses and interpretations. *NeuroImage*, 52:1059–1069, 2010a.

Mikail Rubinov and Olaf Sporns. Complex network measures of brain connectivity: uses and interpretations. *NeuroImage*, 52(3):1059–1069, 2010b.

Mikail Rubinov, Olaf Sporns, Cees van Leeuwen, and Michael Breakspear. Symbiotic relationship between brain structure and dynamics. *BMC Neuroscience*, 10(1):55, 2009.

Cătălin V Rusu, Max Murakami, Ulf Ziemann, and Jochen Triesch. A model of TMS-induced I-waves in motor cortex. *Brain Stimulation*, 7:401–414, 2014.

Maria Luisa Saggio, Petra Ritter, and Viktor K Jirsa. Analytical operations relate structural and functional connectivity in the brain. *PLoS One*, 11(8): e0157292, 2016.

Speranza Sannino, Sebastiano Stramaglia, Lucas Lacasa, and Daniele Marinazzo. Visibility graphs for fMRI data: Multiplex temporal graphs and their modulations across resting-state networks. *Network Neuroscience*, 1 (3):208–221, 2017.

Catherine A Schevon, Shennan A Weiss, Guy McKhann, Robert R Goodman, Rafael Yuste, Ronald G Emerson, and Andrew J Trevelyan. Evidence of an inhibitory restraint of seizure activity in humans. *Nature Communications*, 3(1):1–11, 2012.

Kaspar A Schindler, Stephan Bialonski, Marie-Therese Horstmann, Christian E Elger, and Klaus Lehnertz. Evolving functional network properties and synchronizability during human epileptic seizures. *Chaos: An Interdisciplinary Journal of Nonlinear Science*, 18(3):033119, 2008.

Alfons Schnitzler and Joachim Gross. Normal and pathological oscillatory communication in the brain. *Nature Reviews Neuroscience*, 6(4):285–296, 2005.

Joohi Shahed, James Poysky, Christopher Kenney, Richard Simpson, and Joseph Jankovic. GPi deep brain stimulation for tourette syndrome improves tics and psychiatric comorbidities. *Neurology*, 68(2):159–160, 2007.

S Murray Sherman. Thalamic relays and cortical functioning. *Progress in Brain Research*, 149:107–126, 2005.

Woodrow L Shew and Dietmar Plenz. The functional benefits of criticality in the cortex. *The Neuroscientist*, 19(1):88–100, 2013.

Hotetsu Shimamoto, Hitoyuki Morimitsu, Shunsuke Sugita, Kimihiro Nakahara, and Minoru Shigemori. Therapeutic effect of repetitive transcranial magnetic stimulation in Parkinson's disease. *Rinsho Shinkeigaku*, 39:1264–1267, 1999.

James M Shine, Michael Breakspear, Peter T Bell, Kaylena A Ehgoetz Martens, Richard Shine, Oluwasanmi Koyejo, Olaf Sporns, and Russell A Poldrack. Human cognition involves the dynamic integration of neural activity and neuromodulatory systems. *Nature Neuroscience*, 22(2):289–296, 2019.

Oren Shriki, Jeff Alstott, Frederick Carver, Tom Holroyd, Richard NA Henson, Marie L Smith, Richard Coppola, Edward Bullmore, and Dietmar Plenz. Neuronal avalanches in the resting meg of the human brain. *Journal of Neuroscience*, 33(16):7079–7090, 2013.

Hartwig Siebner and John Rothwell. Transcranial magnetic stimulation: new insights into representational cortical plasticity. *Experimental Brain Research*, 148(1):1–16, 2003.

Hartwig R Siebner, Gesa Hartwigsen, Tanja Kassuba, and John C Rothwell. How does transcranial magnetic stimulation modify neuronal activity in the brain? Implications for studies of cognition. *Cortex*, 45:1035–1042, 2009.

Aditya Somani and Sujita Kumar Kar. Efficacy of repetitive transcranial magnetic stimulation in treatment-resistant depression: the evidence thus far. *General Psychiatry*, 32(4), 2019.

Roberto C Sotero, Nelson J Trujillo-Barreto, Yasser Iturria-Medina, Felix Carbonell, and Juan C Jimenez. Realistically coupled neural mass models can generate EEG rhythms. *Neural Computation*, 19(2):478–512, 2007.

Stamatios N Sotiropoulos, Moisés Hernández-Fernández, An T Vu, Jesper L Andersson, Steen Moeller, Essa Yacoub, Christophe Lenglet, Kamil Ugurbil, Timothy EJ Behrens, and Saad Jbabdi. Fusion in diffusion MRI for improved fibre orientation estimation: An application to the 3T and 7T data of the human connectome project. *NeuroImage*, 134:396–409, 2016.

Andreas Spiegler, Stefan J Kiebel, Fatihcan M Atay, and Thomas R Knösche. Bifurcation analysis of neural mass models: Impact of extrinsic inputs and dendritic time constants. *NeuroImage*, 52(3):1041–1058, 2010.

Olaf Sporns. The human connectome: a complex network. *Annals of the New York Academy of Sciences*, 1224(1):109–125, 2011.

Olaf Sporns. Structure and function of complex brain networks. *Dialogues in clinical neuroscience*, 15(3):247, 2013.

Olaf Sporns and Richard F Betzel. Modular brain networks. *Annual Review of Psychology*, 67:613–640, 2016.

Devarajan Sridharan, Daniel J Levitin, and Vinod Menon. A critical role for the right fronto-insular cortex in switching between central-executive and default-mode networks. *Proceedings of the National Academy of Sciences*, 105(34):12569–12574, 2008.

Ramesh Srinivasan, William R Winter, Jian Ding, and Paul L Nunez. EEG and MEG coherence: measures of functional connectivity at distinct spatial scales of neocortical dynamics. *Journal of Neuroscience Methods*, 166(1): 41–52, 2007.

CJ Stam, ECW Van Straaten, E Van Dellen, P Tewarie, G Gong, A Hillebrand, J Meier, and P Van Mieghem. The relation between structural and functional connectivity patterns in complex brain networks. *International Journal of Psychophysiology*, 103:149–160, 2016.

Iain Stitt, Edgar Galindo-Leon, Florian Pieper, Gerhard Engler, Eva Fiedler, Thomas Stieglitz, and Andreas K Engel. Intrinsic coupling modes reveal the functional architecture of cortico-tectal networks. *Science Advances*, 1(7): e1500229, 2015.

Steven Strogatz. *Sync: The emerging science of spontaneous order*. Penguin UK, 2004.

Prejaas Tewarie, Arjan Hillebrand, Bob W van Dijk, Cornelis J Stam, George C O'Neill, Piet Van Mieghem, Jil M Meier, Mark W Woolrich, Peter G Morris, and Matthew J Brookes. Integrating cross-frequency and within band functional networks in resting-state MEG: a multi-layer network approach. *NeuroImage*, 142:324–336, 2016.

Prejaas Tewarie, BA Hunt, George C O'Neill, Aine Byrne, Kevin Aquino, Markus Bauer, Karen J Mullinger, Stephen Coombes, and Matthew J Brookes. Relationships between neuronal oscillatory amplitude and dynamic functional connectivity. *Cerebral Cortex*, 1:14, 2018.

Prejaas Tewarie, Romesh Abeysuriya, Áine Byrne, George C O'Neill, Stamatios N Sotiropoulos, Matthew J Brookes, and Stephen Coombes. How do spatially distinct frequency specific MEG networks emerge from one underlying structural connectome? the role of the structural eigenmodes. *NeuroImage*, 186:211–220, 2019.

Gregor Thut, Domenica Veniero, Vincenzo Romei, Carlo Miniussi, Philippe Schyns, and Joachim Gross. Rhythmic TMS causes local entrainment of natural oscillatory signatures. *Current Biology*, 21(14):1176–1185, 2011.

Martin Tik, André Hoffmann, Ronald Sladky, Livia Tomova, Allan Hummer, Lucia Navarro de Lara, Henryk Bukowski, Jürgen Pripfl, Bharat Biswal, Claus Lamm, and C Windischberger. Towards understanding rTMS mechanism of action: stimulation of the DLPFC causes network-specific increase in functional connectivity. *NeuroImage*, 162:289–296, 2017.

Wing Ting To, Dirk De Ridder, John Hart Jr, and Sven Vanneste. Changing brain networks through non-invasive neuromodulation. *Frontiers in Human Neuroscience*, 12:128, 2018.

Robert Ton, Gustavo Deco, and Andreas Daffertshofer. Structure-function discrepancy: inhomogeneity and delays in synchronized neural networks. *PLoS Computational Biology*, 10(7):e1003736, 2014.

J Touboul, F Wendling, P Chauvel, and O Faugeras. Neural mass activity, bifurcations, and epilepsy. *Neural Computation*, 23:3232–3286, 2011.

Jochen Triesch, Christoph Zrenner, and Ulf Ziemann. Modeling TMS-induced i-waves in human motor cortex. In *Progress in Brain Research*, volume 222, pages 105–124. Elsevier, 2015.

Shang-Yueh Tsai. Reproducibility of structural brain connectivity and network metrics using probabilistic diffusion tractography. *Scientific Reports*, 8(1): 11562, 2018.

Nathalie Tzourio-Mazoyer, Brigitte Landeau, Dimitri Papathanassiou, Fabrice Crivello, Olivier Etard, Nicolas Delcroix, Bernard Mazoyer, and Marc Joliot. Automated anatomical labeling of activations in SPM using a macroscopic anatomical parcellation of the MNI MRI single-subject brain. *NeuroImage*, 15(1):273–289, 2002.

Peter J Uhlhaas and Wolf Singer. Neural synchrony in brain disorders: relevance for cognitive dysfunctions and pathophysiology. *Neuron*, 52(1):155–168, 2006.

Frederik Van de Steen, Hannes Almgren, Adeel Razi, Karl Friston, and Daniele Marinazzo. Dynamic causal modelling of fluctuating connectivity in resting-state EEG. *NeuroImage*, 189:476–484, 2019.

Martijn P Van Den Heuvel and Hilleke E Hulshoff Pol. Exploring the brain network: a review on resting-state fMRI functional connectivity. *European Neuropsychopharmacology*, 20(8):519–534, 2010.

Martijn P Van Den Heuvel and Olaf Sporns. Rich-club organization of the human connectome. *Journal of Neuroscience*, 31(44):15775–15786, 2011.

Martijn P van den Heuvel and Olaf Sporns. Network hubs in the human brain. *Trends in Cognitive Sciences*, 17(12):683–696, 2013.

David C Van Essen, Stephen M Smith, Deanna M Barch, Timothy EJ Behrens, Essa Yacoub, and Kamil Ugurbil. The WU-Minn human connectome project: an overview. *NeuroImage*, 80:62–79, 2013.

Elisabeth CW van Straaten and Cornelis J Stam. Structure out of chaos: functional brain network analysis with EEG, MEG, and functional MRI. *European Neuropsychopharmacology*, 23(1):7–18, 2013.

Marine Vernet, Shahid Bashir, Woo-Kyoung Yoo, Jennifer M Perez, Umer Najib, and Alvaro Pascual-Leone. Insights on the neural basis of motor plasticity induced by theta burst stimulation from TMS–EEG. *European Journal of Neuroscience*, 37(4):598–606, 2013.

Marine Vernet, Chloé Stengel, Romain Quentin, Julià L Amengual, and Antoni Valero-Cabré. Entrainment of local synchrony reveals a causal role for high-beta right frontal oscillations in human visual consciousness. *Scientific Reports*, 9(1):1–15, 2019.

Diego Vidaurre, Stephen M Smith, and Mark W Woolrich. Brain network dynamics are hierarchically organized in time. *Proceedings of the National Academy of Sciences*, 114(48):12827–12832, 2017.

François JG Vingerhoets, J-G Villemure, P Temperli, C Pollo, E Pralong, and J Ghika. Subthalamic dbs replaces levodopa in parkinson's disease: two-year follow-up. *Neurology*, 58(3):396–401, 2002.

Jord JT Vink, Stefano Mandija, Petar I Petrov, Cornells AT van den Berg, Iris EC Sommer, and Sebastiaan FW Neggers. A novel concurrent TMS-fMRI method to reveal propagation patterns of prefrontal magnetic brain stimulation. *Human Brain Mapping*, 39(11):4580–4592, 2018.

Christopher S von Bartheld, Jami Bahney, and Suzana Herculano-Houzel. The search for true numbers of neurons and glial cells in the human brain: A review of 150 years of cell counting. *Journal of Comparative Neurology*, 524 (18):3865–3895, 2016.

Maxwell B Wang, Julia P Owen, Pratik Mukherjee, and Ashish Raj. Brain network eigenmodes provide a robust and compact representation of the structural connectome in health and disease. *PLoS Computational Biology*, 13(6), 2017.

Yujiang Wang, Marc Goodfellow, Peter Neal Taylor, and Gerold Baier. Dynamic mechanisms of neocortical focal seizure onset. *PLoS Computational Biology*, 10(8), 2014.

Quan Wen and Dmitri B Chklovskii. Segregation of the brain into gray and white matter: a design minimizing conduction delays. *PLoS Computational Biology*, 1(7), 2005.

F Wendling, F Bartolomei, JJ Bellanger, and P Chauvel. Epileptic fast activity can be explained by a model of impaired gabaergic dendritic inhibition. *European Journal of Neuroscience*, 15(9):1499–1508, 2002.

T L Williams and G Bowtell. The calculation of frequency-shift functions for chains of coupled oscillators, with application to a network model of the lamprey locomotor pattern generator. *Journal of Computational Neuroscience*, 4:47–55, 1997.

Hugh R Wilson and Jack D Cowan. Excitatory and inhibitory interactions in localized populations of model neurons. *Biophysical Journal*, 12(1):1–24, 1972.

Arthur T Winfree. Biological rhythms and the behavior of populations of coupled oscillators. *Journal of Theoretical Biology*, 16(1):15–42, 1967.

Mingrui Xia, Jinhui Wang, and Yong He. Brainnet viewer: a network visualization tool for human brain connectomics. *PloS ONE*, 8(7):e68910, 2013.

BT Thomas Yeo, Fenna M Krienen, Jorge Sepulcre, Mert R Sabuncu, Danial Lashkari, Marisa Hollinshead, Joshua L Roffman, Jordan W Smoller, Lilla Zöllei, Jonathan R Polimeni, Bruce Fischl, Hesheng Liu, and Randy L Buckner. The organization of the human cerebral cortex estimated by intrinsic functional connectivity. *Journal of Neurophysiology*, 106(3):1125, 2011.

Dahua Yu, Kai Yuan, Lin Luo, Jinquan Zhai, Yanzhi Bi, Ting Xue, Xiaoying Ren, Ming Zhang, Guoyin Ren, and Xiaoqi Lu. Abnormal functional integration across core brain networks in migraine without aura. *Molecular pain*, 13:1744806917737461, 2017a.

Meichen Yu, Marjolein MA Engels, Arjan Hillebrand, Elisabeth CW Van Straaten, Alida A Gouw, Charlotte Teunissen, Wiesje M Van Der Flier, Philip Scheltens, and Cornelis J Stam. Selective impairment of hippocampus and posterior hub areas in alzheimer's disease: an MEG-based multiplex network study. *Brain*, 140(5):1466–1485, 2017b.

ULF Ziemann. TMS induced plasticity in human cortex. *Reviews in the Neurosciences*, 15(4):253–266, 2004.

Vincent Zimmern. Why brain criticality is clinically relevant: A scoping review. *Frontiers in Neural Circuits*, 14:54, 2020.

Christoph Zrenner, Debora Desideri, Paolo Belardinelli, and Ulf Ziemann. Real-time EEG-defined excitability states determine efficacy of TMS-induced plasticity in human motor cortex. *Brain stimulation*, 11(2):374–389, 2018.

Appendix A

Selected Matlab® codes

In this section we produce codes that were used in computing several results presented in this thesis. In the interests of brevity, we here include two Matlab® codes that demonstrate a range of computational methods that were critical in our simulation and analysis of NMM network dynamics. Since portions of these codes were repurposed for several results throughout this thesis, they appropriately summarise a large proportion of our computational work. Other codes, including those used for XPPAUT and Julia simulations, are available on GitHub (https://github.com/MichaelForrester/PhD-Codes/).

Function to calculate the Jaccard coefficient between SC and FC for the Jansen–Rit NMM network

FC simulation is crucial to many of the results we present in this thesis. The following code was used in constructing Figure 4.5(a), which shows the Jaccard similarity between SC and simulated FC over a parameter space of the Jansen-Rit model. It outlines the procedure to generate time-series, hilbert transform to obtain instantaneous phases and then process this data via MPC to an FC matrix. We simulated FC in this way to explore structure–function relations in chapters 4 and 5, while we also use is as a basis to investigate the neuromodulatory effects of TMS in chapter 6. The Jaccard similarity agreement is also used in different ways: as a convenient metric to determine the degree to which structure contributes to emergent FC (as in Figures 4.5(a) and 6.7), but also to qualify the accuracy of FC matrices predicted from weakly-coupled oscillator theory (Figure 4.7) and linear theory (Figure 7.4).

```
function J=Jaccard(C,P)

%Function to calculate the Jaccard coefficient for
   the SC matrix C and the FC matrix
%resulting from the MPC between each node's
   timeseries (transformed by the Hilbert function).
%Timeseries dynamics are governed by the Jansen-Rit
   model with parameters P.
```

```
% Inputs: C - Connectivity matrix where C(i,j) is
   coupling strength from node j -> i.
%          P - Structure containing Jansen-Rit
   paramteters.
% Output: Jaccard - Jaccard coefficient between SC
   and simulated FC.

N=length(C); % Number of nodes.
C_bin=1*(C~=0); % Binary SC.

% Setting time increments.
T = 500; dt = 0.001; N = T/dt;

% Preallocating variables.
y0=rand(N,1);
y1=rand(N,1);
y2=rand(N,1);
y3=rand(N,1);
y4=rand(N,1);
y5=rand(N,1);

% Preallocating saved variables.
y0save = zeros(N,1);
y1save = zeros(N,1);
y2save = zeros(N,1);
y3save = zeros(N,1);
y4save = zeros(N,1);
y5save = zeros(N,1);
ysave  = zeros(N,N+1);

% Preallocating space for timeseries of variable y.
ysave(:,1) = y1-y2;

% Defining noise.
dW = normrnd(0,0.1,F,N-1);

% Implementing method.
for j = 1:N
        y0save = y0 + y3*dt;
        y1save = y1 + y4*dt;
        y2save = y2 + y5*dt;
        y3save = y3 + ...
            (P.A*P.a*sigm(y1-y2)-2*P.a*y3-(P.a^2)*y0)
               *dt;
        y4save = y4 + ...
            (P.A*P.a*(P.p.P+P.e*(C*f(y1-y2))+P.C2*f(P
               .C1*y0))-2*P.a*y4-(P.a^2)*y1)*dt+dW(:,N
               -1);
        y5save = y5 + ...
```

```
            (P.B*P.b*P.C4*f(P.C3*y0)-2*P.b*y5-(P.b^2)
               *y2)*dt;

        y0 = y0save; y1 = y1save; y2 = y2save;
        y3 = y3save; y4 = y4save; y5 = y5save;
        ysave(:,j+1)=y1-y2;
end

ysave(:,1:100000)=[]; % Removing inital transients.
U_trans = angle(hilbert(ysave')); % Implementing
   Hilbert tranform.
FC = zeros(N); % Preallocating FC.

% Calculating FC matrix.
for f = 1:F
    FC(f,f+1:F) = abs((1/size(U_trans,1))*sum(exp(1i
       *(unwrap(U_trans(:,f+1:F))-repmat(unwrap(
       U_trans(:,f)),1,F-f)))));
    FC(f+1:F,f)=FC(f,f+1:F);
end

% Thresholding and binarising FC matrix.
R_bin=zeros(F);
[~,I]=sort(FC(:));
R_bin(I(end-cons+1:end))=1;

% Calculating Jaccard coefficient.
J = sum(sum(C_bin.*R_bin))/sum(sum(C_bin==1|R_bin==1)
   );
end
```

Function to calculate eigenvalue spectra for undelayed and delayed next-generation NMM

Many of the analytical results in this thesis are underpinned by linear methods, which are used to compute bifurcation sets for NMMs (Figure 4.3), as well as predict the organisation of simulated FC matrices and to quantify their stability (Figures 4.7 and 7.4). The following code computes the spectra for the next-generation NMM with delays, as well as its undelayed counterpart, using the spectral equations derived in chapter 3 (section 3.3). Importantly, this method (for row-normalised matrices) allows us to have decoupled spectral equations for each structural eigenmode. This not only makes solving the eigenvalue problems easier when calculating bifurcation sets, but also allows us to determine each eigenmode's stability individually, from which we make predictions about emergent network behaviour (see section 7.3).

```
function [nodel_spectra,del_spectra]=CBdelplot(C,D,y0
   ,P,s)
    % Calculates the spectra for an undelayed network
        of next-generation neural masses with
       paramters set in P, as well as spectra for the
       same network with conduction delays with
       distance matrix D and conduction speed s.

    N=length(C); % Number of nodes.
    M=length(y0); % Number of ODEs for each node.

    % Calculating delay matrix (distance/speed).
    tau=D/s;

    C0=P.e*C; % Scaling coupling.

    [EVec,EVal]=eig(C0); % Eigenvectors and
       eigenvalues of SC matrix.

    % Defining solver options.
    options = optimoptions(@fsolve,'Display','iter',
       ...
        'Algorithm','trust-region-dogleg',...
        'SpecifyObjectiveGradient',true,'
           PrecondBandWidth',0);

    % Solving neural-mass network using next-
       generation model and its jacobian defined in
       NextGen, with initial conditions y0.
    [~,~,~,~,jacobian] = fsolve(@(y) NextGen(y,P),y0,
       options);

    jacobian=full(jacobian); % Conversion from sparse
        to full Jacobian.

    % Setting DF (from equation 7.8).
    DF=jacobian; DF(M,1:2)=0;

    % Setting DG (from equation 7.8).
    DG=zeros(M);
    DG(M,1)=P.aext^2*dfx(S(1),S(2),P.taue);
    DG(M,2)=P.aext^2*dfy(S(1),S(2),P.taue);

    % Redefining options
    options = optimoptions(@fsolve,'Display','iter',
       ...
        'Algorithm','trust-region-dogleg',...
        'SpecifyObjectiveGradient',false,'
           PrecondBandWidth',0);
```

```
nodel_spectra=zeros(M*N,1); % Initialising
   spectra for undelayed network.
del_spectra=[]; % Initialising spectra for
   delayed network.

% Loop over each eigenmode n.
for n=1:N

    % Spectra for nth eigenmode of undelayed
       system.
    nodel_spectra((n-1)*M+1:n*M)=eig(DF+EVal(n)*
       DG);

    % Set upper and lower limits for real and
       imaginary eigenvalues and make arrays with
       1000 uniform intervals.
    u_lim=[u_min u_max]; v_lim=[v_min v_max];
    u=linspace(u_lim(1),u_lim(2),1001);
    v=linspace(v_lim(1),v_lim(2),1001);

    % Initialise plane in selected domain of real
       /imaginary values.
    UVplane=zeros(length(v),length(u));

    % Calculate absolute value of characteristic
       determinant for each complex value.
    for U=1:length(u)
        for V=1:length(v)
            ig=u(U)+1i*v(V);
            UVplane(V,U)=abs(del_det(l,C0,tau,DF,
               DG,EVec(:,n)));
        end
    end

    % Find local minima in UVplane
    [X,Y]=meshgrid(u,v);
    ix = find(imregionalmin(UVplane));

    % Setting initial conditions for solver
    X0=X(ix)+1i*Y(ix);

    % Solving for each eigenvalue
    for m=1:length(X0)
        x0=X0(m);
        [l,~,ef,~] = fsolve(@(l) del_det(l,C0,tau
           ,DF,DG,EVec(:,n)),x0,options);
        if ef~=-2 && ef~=-3
```

```
                del_spectra=[del_spectra;real(l),imag
                   (l),n];
            end
        end
    end
end

% Defining df/dx and df/dy, where f is firing rate of
    excitatory population, x and y are the real and
   imaginary Kuramoto order paramters, respectively.
function X = dfx(x,y,tau)
    X=-(1/(pi*tau))*2*(x.^2+2*x-y.^2+1)./((1+2*x+x
       .^2+y.^2).^2);
end

function X = dfy(x,y,tau)
    X=-(1/(pi*tau))*4*y.*(1+x)./((1+2*x+x.^2+y.^2)
       .^2);
end

% Characteristic determinant.
function X=del_det(l,C,tau,DF,DG,V)
    X=det(eye(length(DF))*l-(DF+sum(sum(C.*exp(-l*tau
       ).*(V*V')))*DG));
end
```

Appendix B

List of Abbreviations

SC	Structural connectivity
FC	Functional connectivity
EEG	Electroencephalography
MEG	Magnetoencephalography
MRI	Magnetic Resonance Imaging
fMRI	Functional Magnetic Resonance Imaging
DWI	Diffusion-Weighted Imaging
DTI	Diffusion Tensor Imaging
ECT	Electroconvulsive Therapy
DBS	Deep brain stimulation
TMS	Transcranial Magnetic Stimulation
NMM	Neural mass model
PRC	Phase Response Curve
MPC	Mean phase coherence
MPA	Mean phase agreement
LLE	Largest Lyapunov exponent